

Dissertation  
submitted to the  
Combined Faculty of Mathematics, Engineering and Natural Sciences  
of Heidelberg University, Germany  
for the degree of  
Doctor of Natural Sciences

Put forward by  
Sandra Anna Brandstetter  
Born in: Linz, Austria  
Oral examination: 05.06.2025



# Collective Behavior in Few-Fermion Systems

**Referees:**

Prof. Dr. Selim Jochim

Prof. Dr. Markus K. Oberthaler



## **Abstract**

This thesis reports on the exploration of collective behavior in a system of few fermionic atoms. Access to both real- and momentum space observables in combination with a high degree of control over both particle number and interaction strength allows us to explore the emergence of collective behavior from the bottom up - atom by atom.

Inspired by observations in high-energy physics, where hydrodynamic behavior is present in absence of a separation of scales, we explore interaction-driven elliptic flow which is commonly considered a smoking-gun of hydrodynamic behavior. Our measurements reveal elliptic flow in systems of only six constituents.

Motivated by the formation of pairs of fermionic particles in system with broken translational symmetry (such as atomic nuclei or 'dirty' superconductors), where BCS theory does not apply, we investigate how a spatially varying potential affects pair formation. By altering interaction strength and particle number, we observe a transition from a regime in which pair formation is determined by the discrete level structure of the potential to a regime in which the potential only influences pairing by altering the local density.



## Zusammenfassung

Diese Arbeit behandelt die Erforschung von kollektivem Verhalten in einem System aus wenigen, fermionischen Atomen. Der Zugriff auf Messgrößen im Orts und Impulsraum in Kombination mit einem hohen Maß an Kontrolle über Teilchenzahl und Wechselwirkungsstärke ermöglicht es die Entstehung von kollektivem Verhalten zu erforschen.

Inspiziert von Beobachtungen in der Hochenergiephysik, wo hydrodynamisches Verhalten bei fehlender Skalentrennung beobachtet wird, erforschen wir den wechselwirkungsgetriebenen elliptischen Fluss, der gemeinhin als Indikator für hydrodynamisches Verhalten gilt. Unsere Messungen zeigen elliptischen Fluss in Systemen die aus lediglich sechs Atomen bestehen.

Motiviert von Paarbildung zwischen Fermionen in Systemen mit gebrochener Translationssymmetrie (wie Atomkernen oder 'schmutzigen' Supraleitern), in denen BCS Theorie ihre Gültigkeit verliert, untersuchen wir wie ein räumlich variierendes Potenzial die Paarbildung beeinflusst. Durch Veränderung von Wechselwirkungsstärke und Teilchenzahl beobachten wir einen Übergang von einem Regime, in dem die Paarbildung durch die diskrete Level-Struktur des Potentials bestimmt wird, zu einem Regime, in dem das Potenzial die Paarbildung nur durch die Veränderung der lokale Dichte beeinflusst.



*To my parents*



# Contents

<b>1</b>	<b>Introduction</b>	<b>1</b>
1.1	Thesis outline . . . . .	3
1.2	List of publications . . . . .	4
<b>2</b>	<b>Theory of ultracold quantum gases</b>	<b>5</b>
2.1	Bosons and Fermions . . . . .	6
2.2	Internal structure of ${}^6\text{Li}$ . . . . .	7
2.3	Interactions in ultracold quantum gases . . . . .	8
2.4	Optical Dipole Traps . . . . .	14
<b>3</b>	<b>Experimental setup and techniques</b>	<b>17</b>
3.1	Reaching quantum degeneracy . . . . .	17
3.2	Deterministic state preparation . . . . .	19
3.3	Single atom resolved imaging . . . . .	22
<b>4</b>	<b>Matterwave manipulation</b>	<b>25</b>
4.1	Rotating in phase space . . . . .	26
4.2	Experimental implementation . . . . .	29
4.3	Conclusion . . . . .	39
<b>5</b>	<b>Emergence of elliptic flow</b>	<b>41</b>
5.1	Hydrodynamics in high energy physics . . . . .	42
5.2	Elliptic flow in a mesoscopic Fermi gas . . . . .	43
5.3	Emergence of interaction-driven elliptic flow . . . . .	48
5.4	Interaction dependence . . . . .	49
5.5	Conclusion and Outlook . . . . .	50
<b>6</b>	<b>Pairing: from shell to bulk</b>	<b>53</b>
6.1	Translation invariant systems . . . . .	54
6.2	Broken translational symmetry . . . . .	56
6.3	Pairing in a harmonic oscillator potential . . . . .	57
6.4	Experimental observation . . . . .	65
6.5	Conclusion and Outlook . . . . .	69
<b>7</b>	<b>Summary and Outlook</b>	<b>71</b>
	<b>Bibliography</b>	<b>75</b>
	<b>List of Acronyms</b>	<b>85</b>
	<b>Acknowledgments</b>	<b>87</b>



# 1 | Introduction

In the first place it is fair to state that we are not experimenting with single particles, any more than we can raise Ichthyosauria in the zoo.

---

ERWIN SCHRÖDINGER  
*J. Phil. Sci* 3, 233–247 (1952).

At the dawn of the computer age, William Phillips, an engineer-turned-sociology-student, noticed a perplexing similarity between the differential equations describing the flow of water and those used in macroeconomic theories. Following this insight, he rushed to his landlady's garage to assemble an extraordinary device. This device – dubbed the Monetary National Income Analogue Computer (MONIAC) – simulates the complex interplay of different economical parameters using tanks, pipes and pumps. After calibrating it to the day's knowledge of the British economy, William Phillips found that the MONIAC had a precision of 2% – primarily limited by the finite water tightness of the contraption. In a time when computers were still (mainly female) human beings, the MONIAC represented a remarkable breakthrough. It could not only be used to visualize the economic system, but could also simulate the impact of different economic policies – a feat that was beyond the reach of human computers. Moreover, it also included the out of equilibrium dynamics occurring when the economy transitions from one steady state to the other – such turbulent dynamics were not describable by economic theories. Following the prototype, roughly a dozen of these devices were built and used even by the Bank of Guatemala and the Ford Motor Company<sup>1</sup>. [1, 2]

The MONIAC is a paradigmatic example of an analogue computer, showcasing the power of using an analogue system in a clean and controllable environment to explore complex problems. This idea is not only pertinent to the classical world, but can also be used to explore the quantum world. As Richard Feynman famously conjectured in 1982 [3], simulations of quantum mechanical phenomena are best implemented on quantum mechanical systems. Following the discussion of Hangleiter et al. [4], analogue quantum simulators can be divided into two different categories: *analogue quantum computers* and *analogue quantum emulators*. *Analogue quantum computers* are used to explore the formal properties of the target system. This is often achieved by implementing the target Hamiltonian on an analogue system offering a higher degree of control than the target system. An example of an analogue quantum computer is simulating solid state systems – described by the Hubbard Hamiltonian [5] – with ultracold atoms in optical lattice potentials [6, 7]. *Analogue quantum emulators* focus on reproducing only specific physical properties of the target system. Often, this allows to gain a deeper qualitative understanding of the essential mechanism underlying the physical properties. Examples for analogue quantum emulation include simulating the dynamics in curved spacetime using

---

<sup>1</sup>Fortunately, none of them ever exhibited the direct feedback to the real world economy discussed in Terry Pratchett's fantasy novel 'Making money'.

---

a two-dimensional (2D) Bose-Einstein condensate (BEC) [8] or modelling quantum effects in photosynthesis with coupled waveguides [9, 10]. Note that in this distinction, the MONIAC is a classical analogue computer, as it harnesses the equivalency of the differential equations describing macroeconomics and those describing the flow of water.

In this thesis, we use few fermionic  ${}^6\text{Li}$  atoms to perform *analogue quantum emulation* of collective behavior in various strongly interacting quantum systems. Collective behavior is ubiquitous in nature, both in the classical and quantum world. Sardines move in synchrony to create so-called bait balls that confuse their predators, electrons in superconductors form coherent Cooper pairs. But what mechanisms drive this collective behavior? How does it emerge from the few-body limit? Utilizing the high degree of control and observables accessible in our experiment, we explore collective phenomena in systems with an intermediate number of constituents. Here, quantum emulation is especially useful, as these systems lie beyond the reach of both exact theoretical calculations available for few-body systems and many-body models.

Inspired by observations in high-energy proton-proton collisions, which reveal elliptic flow – a signature of hydrodynamic behavior – despite the absence of a separation of scales, we study the emergence of elliptic flow in a system of few fermions. While our experiments naturally do not capture all physical properties of proton-proton collision, the controlled environment and the access to observables that remain elusive in high-energy nuclear collisions, allow us to distinguish single particle and collective dynamics to study the emergence of interaction-driven elliptic flow, atom by atom.

In the nucleus, the formation of pairs between the fermionic nucleons is strongly influenced by the nuclear mean-field potential, which breaks translational symmetry. To gain a deeper understanding of the influence of broken translational symmetry on pair formation, we disregard much of the complexity inherent in the full nuclear system, such as the effects of multi-nucleon interactions and nuclear excitations. We perform analogue quantum emulation by exploring pairing between fermionic  ${}^6\text{Li}$  atoms in a harmonic oscillator potential. Our control over both particle number and interaction strength allows us to explore how the formation of pairs is influenced by this confining potential - from the regime where pairing is governed by the discrete level structure to the regime where the potential only sets the local density.

## 1.1 Thesis outline

Chapters 2 and 3 introduce the basic theoretical and experimental concepts used throughout the scope of this thesis. They aim to provide an introduction aimed at readers not well-versed in the theory of ultracold atoms or the experimental details of our cold atom experiment. A discussion of the theoretical concepts pertinent to the individual chapters is provided in the respective chapters.

Chapter 4 introduces the concept of matterwave manipulation used to gain access to real and momentum space with single atom resolution. We discuss the design parameters used to optimize an optical potential for accurate magnification of the initial matterwave and benchmark its performance using systems with a known wave function. The chapter is aimed to provide instructions for the experimental implementation of a matterwave magnification scheme.

In Chapter 5, we present our measurements on interaction-driven elliptic flow in a system of few fermions. We observe the interacting expansion of ten fermions and compare the evolution to different models. Additionally, we explore the emergence of interaction-driven elliptic flow as a function of the number of constituents and interaction strength.

Chapter 6 focuses on the influence of a spatially varying potential on the formation of pairs between two distinguishable fermions. By measuring the pair density in real and momentum space, we can distinguish a regime at low interaction strengths, where pairs form between time-reversed states of the potential to a regime at higher interaction strength, where the potential only determines the local density.

## 1.2 List of publications

Most of the results presented in this thesis can be found in the following references:

- *Magnifying the Wave Function of Interacting Fermionic Atoms*  
Sandra Brandstetter\*, Carl Heintze\*, Keerthan Subramanian\*, Paul Hill, Philipp M. Preiss, Maciej Galka, Selim Jochim  
arXiv: [2409.18954](https://arxiv.org/abs/2409.18954) (2024)
- *Emergent interaction-driven elliptic flow of few fermionic atoms*  
Sandra Brandstetter\*, Philipp Lunt\*, Carl Heintze, Giuliano Giacalone, Lars H. Heyen, Maciej Galka, Keerthan Subramanian, Marvin Holten, Philipp M. Preiss, Stefan Floerchinger, Selim Jochim  
doi: [Nature Physics \*\*21\*\*, 52–56 \(2025\)](https://doi.org/10.1038/s41586-025-0250-2) arXiv: [2308.09699](https://arxiv.org/abs/2308.09699) (2023)
- *Observation of Cooper Pairs in a Mesoscopic 2D Fermi Gas*  
Marvin Holten, Luca Bayha, Keerthan Subramanian, Sandra Brandstetter, Carl Heintze, Philipp Lunt, Philipp M. Preiss, Selim Jochim  
doi: [Nature \*\*606\*\*, 287-291 \(2022\)](https://doi.org/10.1038/s41586-022-0250-2), arXiv: [2109.11511](https://arxiv.org/abs/2109.11511) (2022)

Additionally, Chapter 6 is based on a paper in preparation:

- *Cooper Pairing: from the surface to the bulk*  
Sandra Brandstetter, Carl Heintze, Fabian Brauneis, Stephanie M. Reimann, Georg M. Bruun, Maciej Galka, Selim Jochim

## 2 | Theory of ultracold quantum gases

If atoms would behave like billiard balls, you  
and me would both be out of jobs.

---

PHILIPP M. PREISS  
*to the author, 2021*

Ultracold systems are among the most used experimental platforms for simulating quantum many-body physics in an isolated and controlled environment. Since the first realization of a BEC in a vapor of rubidium atoms [11], a wide variety of atomic and molecular species have been brought to quantum degeneracy. These range from the comparatively simple alkali atoms to the significantly more complex lanthanides, such as erbium [12] and dysprosium [13], as well as ultracold molecules [14, 15]. The choice of atomic or molecular species not only defines the system’s quantum statistics (see Sec. 2.1) but also determines key properties such as the nature of interactions (see Sec. 2.3). As a result, ultracold atom experiments provide an exceptionally versatile platform for simulating a broad range of quantum phenomena. Even within a single atomic species, diverse experimental settings allow for the exploration of vastly different physical phenomena. For instance, fermionic  ${}^6\text{Li}$  atoms – used here to explore the emergence of collective behavior – have also been employed to study the Fermi-Hubbard model in optical lattices [16, 17] or, when coupled to a high-finesse optical cavity, to investigate light-induced density waves [18].

*This chapter provides a concise overview of the properties of fermionic  ${}^6\text{Li}$  atoms and the theoretical concepts underlying this thesis, mainly aimed at readers not well versed in the theory of ultracold atoms. Those already familiar with ultracold fermions can comfortably move on to subsequent chapters. A more detailed discussion of specialized topics relevant to individual chapters is presented in the respective chapters.*

## 2.1 Bosons and Fermions

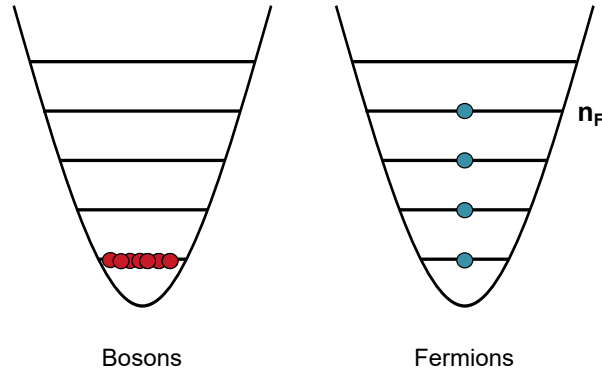


**Figure 2.1: Occupation of a 1D harmonic oscillator potential at zero temperature.** The fundamental properties of indistinguishable particles are determined by their exchange symmetry. For bosons, the total wave function is symmetric under particle exchange. Non-interacting bosons at zero temperature will accumulate in the lowest energy state. In contrast, fermions obey antisymmetric exchange statistics. Hence, they are subject to the Pauli exclusion principle, limiting the maximum occupation of each single-particle quantum state to one. As a result, non-interacting fermions at zero temperature fill all available energy levels up to the Fermi level  $n_F$ .

A fundamental distinction in quantum mechanics is the classification of particles into fermions and bosons. This distinction becomes relevant when the wave-packets of the individual particles start to overlap, i.e. when the de-Broglie wavelength  $\lambda_{\text{DB}} = h/p$  (where  $p$  is the momentum) approaches the mean interparticle spacing. The classification of (composite) particles into fermions and bosons depends on their total spin: Particles with half-integer total spin (in units of  $\hbar$ ) follow fermionic-, those with integer spin obey bosonic-commutation relations.

When the two particles are fermions, their total wave function is antisymmetric under particle exchange:

$$\psi(\xi_1, \xi_2) = -\psi(\xi_2, \xi_1). \quad (2.1)$$

This anti-symmetrization of the wave function directly leads to Pauli's exclusion principle, as the total wave function of two indistinguishable particles in the same quantum state can not be anti-symmetrized. Thus, non-interacting trapped fermions at zero temperature will fill the energy levels of the trap up to the Fermi level  $n_F$ , which sets the Fermi energy  $E_F$ . This is sketched in Fig. 2.1.

For two indistinguishable bosons (with coordinates  $\xi_1$  and  $\xi_2$ ), the total wave function is symmetric under particle exchange, i.e.

$$\psi(\xi_1, \xi_2) = \psi(\xi_2, \xi_1). \quad (2.2)$$

Consequently, multiple bosons can occupy the same quantum state, as sketched in Fig. 2.1.

## 2.2 Internal structure of ${}^6\text{Li}$

Here, we briefly introduce the features of  ${}^6\text{Li}$  relevant to this thesis, based on [19]. There one can also find a detailed discussion of the properties of  ${}^6\text{Li}$ .

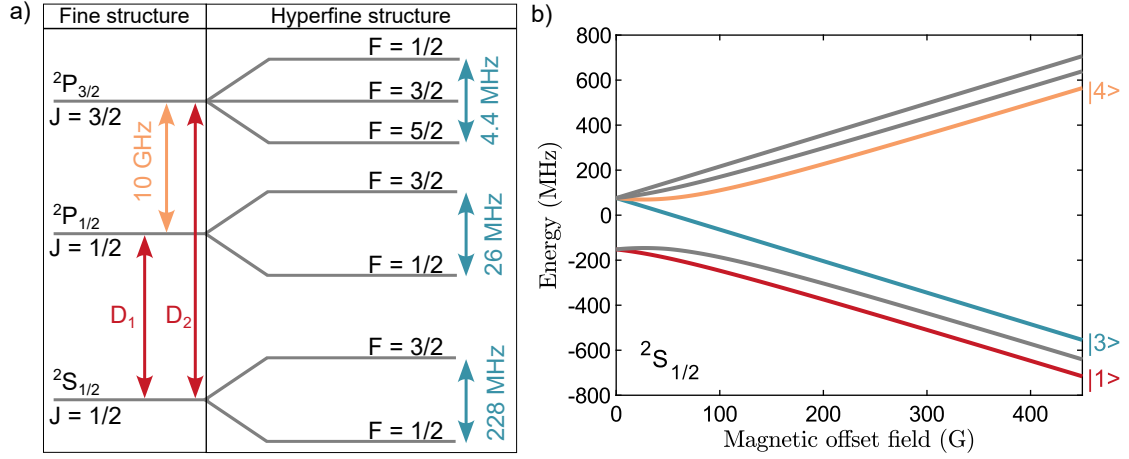


**Figure 2.2: Schematic illustration of the fine and hyperfine structure of  ${}^6\text{Li}$ .** a) Energy level scheme of  ${}^6\text{Li}$  - not to scale. The ground state ( ${}^2S$ ) exhibits a single fine structure manifold ( ${}^2S_{1/2}$ ). The first excited state ( ${}^2P$ ) is split into two states by the spin orbit coupling ( ${}^2P_{1/2}$  and  ${}^2P_{3/2}$ ). They are coupled to the ground state by the  $D_1$  and  $D_2$  line respectively. The ground state has two hyperfine manifolds at zero field. Their magnetic field dependence is shown in b) . At low magnetic fields, the energy of the states is set by  $m_F$ . At higher magnetic offset fields, we enter the Paschen-Back regime and the energy is set by  $m_J$ . We label these states as |1> to |6> in ascending order of energies. The three states (|1>, |3>, |4>) mainly used in the scope of this thesis are highlighted. Figure based on [19].

Lithium is the first (and lightest) element in the Alkali group. As all alkali atoms, it has a single valence electron and a hydrogen-like level structure. The ground state ( ${}^2S$ ) exhibits a single fine structure manifold ( ${}^2S_{1/2}$ ). The first excited state ( ${}^2P$ ) is split into two states ( ${}^2P_{1/2}$  and  ${}^2P_{3/2}$ ) by spin-orbit coupling. They are coupled to the ground state by the  $D_1$  and  $D_2$  line, respectively. The  $D_1$  and  $D_2$  both have a wavelength of  $\lambda \approx 671$  nm and are separated by only 10 GHz

Within the scope of this thesis, we use the isotope  ${}^6\text{Li}$ . It has a nuclear spin of  $I = 1$ , which, in combination with the spin  $S = 1/2$  of the valence electron, leads to a half-integer total spin -  ${}^6\text{Li}$  is fermionic. The nuclear spin gives rise to a hyperfine splitting of both the ground and excited states. While the hyperfine splitting of the ground state is  $\approx 228$  MHz, the two excited states  ${}^2P_{1/2}$  and  ${}^2P_{3/2}$  feature a hyperfine splitting of only  $\approx 26$  MHz and  $\approx 4.4$  MHz, respectively. The fine and hyperfine structure of  ${}^6\text{Li}$  is sketched in Fig. 2.2a) .

Figure 2.2b) shows the magnetic field dependence, i.e. the Zeeman splitting of the  ${}^2S_{1/2}$  state. At low magnetic fields, the energy of the states is set by  $m_F$ . At higher magnetic offset fields ( $B \gtrsim 100$  G), we enter the Paschen-Back regime and the energy is set by  $m_J$ . We label the states at high magnetic fields as |1> to |6> in ascending order of energies. The three high field seeking states |1>, |2> and |3> are separated by  $\approx 80$  MHz. Consequently, transitions between them can be driven with radio frequency (RF)-fields. All the possible two-component mixture of these three hyperfine states are collisionally stable. Within the scope of this thesis, we use

the  $|1\rangle - |3\rangle$  mixture. For simplicity, we refer to atoms in  $|1\rangle$  as spin-up and to those in  $|3\rangle$  as spin-down atoms.

## 2.3 Interactions in ultracold quantum gases

*The following discussion is based on lecture notes and reviews [20–22].*

Tuneable interactions are a vital ingredient of ultracold quantum gases. On the one hand, they enable the exploration of complex many-body quantum phenomena. On the other hand, collisions ensure the thermalization of the system, and are thus an essential ingredient for reaching quantum degeneracy via evaporative cooling (see Sec. 3.2). The dominant interactions between  ${}^6\text{Li}$  atoms are the van der Waals (VdW) interactions. The dipole-dipole interaction caused by the magnetic dipole moment of the atom is negligible.

Let us consider two distinguishable particles (1 and 2) of equal mass ( $m_a$ ) in a three-dimensional (3D) geometry, interacting via a (radially symmetric) interaction potential  $V(r)$  with finite range  $r_0$  – as is the case for the VdW potential. The Schrödinger equation describing the relative motion of these two particles is given by

$$\left( \frac{\hat{\mathbf{p}}^2}{2M} + V(\hat{\mathbf{r}}) \right) \psi_{\mathbf{k}}(\mathbf{r}) = E_{\mathbf{k}} \psi_{\mathbf{k}}(\mathbf{r}), \quad (2.3)$$

where  $M = m_a/2$  is the reduced mass, and we use the position and momentum operators for the relative coordinates:  $\hat{\mathbf{r}} = \hat{\mathbf{r}}_1 - \hat{\mathbf{r}}_2$  and  $\hat{\mathbf{p}} = (\hat{\mathbf{p}}_1 - \hat{\mathbf{p}}_2)/2$ , respectively. When the relative distance is larger than  $r_0$ , the characteristic length of the potential,  $V(\hat{\mathbf{r}}) \rightarrow 0$  and the solution reduces to that of a free particle with energy

$$E_{\mathbf{k}} = \frac{\hbar^2 k^2}{2M}. \quad (2.4)$$

As the collision is elastic, the total energy and wave number  $k$  is conserved – the collision can only cause a phase shift. The total wave function is

$$\psi_{\mathbf{k}}(\mathbf{r}) \xrightarrow{r \rightarrow \infty} \underbrace{e^{i\mathbf{k}\mathbf{r}}}_{\psi_{\text{in}}(\mathbf{r})} + \underbrace{f(k, \theta) \frac{e^{ikr}}{r}}_{\psi_{\text{out}}(\mathbf{r})}, \quad (2.5)$$

the superposition of the incoming plane wave  $\psi_{\text{in}}(\mathbf{r})$  and the outgoing scattered wave  $\psi_{\text{out}}(\mathbf{r})$ . The scattering amplitude  $f(k, \theta)$ , depends on the scattering energy (through  $k$ ) and the angle  $\theta$  between the ingoing wave and the direction along which the outgoing wave is observed. It contains the phase shift and amplitude of the scattered wave. The differential scattering cross-section for scattering in direction  $(\theta, \phi)$  is then given by

$$\frac{d\sigma(k, \theta, \phi)}{d\Omega} = |f(k, \theta)|^2. \quad (2.6)$$

The total scattering cross-section  $\sigma$  is obtained by integrating over all scattering angles

$$\sigma(k) = \int_0^{2\pi} \int_0^\pi |f(k, \theta)|^2 \underbrace{\sin \theta d\theta d\phi}_{d\Omega}. \quad (2.7)$$

As the spherically symmetric scattering potential conserves angular momenta, the scattering problem can be simplified by expressing the plane wave as a sum of the angular momentum eigenstates  $l$ , i.e. by performing the partial wave expansion. The relative wave function is then given as

$$\psi_{\mathbf{k}}(\mathbf{r}) = \sum_{l=0}^{\infty} P_l(\cos \theta) \frac{u_{k,l}(r)}{r}, \quad (2.8)$$

where  $P_l(\cos \theta)$  are the Legendre polynomials. The spherical symmetry of  $V(\hat{\mathbf{r}})$  ensures that states with different  $l$  do not couple, hence we can write the scattering equation independently for each partial wave. The Schrödinger equation for the  $l$ -th partial wave is then given by

$$\left( \frac{\hat{\mathbf{p}}^2}{2M} + \underbrace{\left( V(\hat{\mathbf{r}}) + \frac{\hbar^2 l(l+1)}{2Mr^2} \right)}_{\tilde{V}(\hat{\mathbf{r}})} \right) \frac{u_{k,l}(r)}{r} = E_{\mathbf{k}} \frac{u_{k,l}(r)}{r}. \quad (2.9)$$

Following [21], the total scattering amplitude is

$$f(k, \theta) = \frac{1}{k} \sum_{l=0}^{\infty} (2l+1) (e^{i\delta_l} \sin \delta_l) P_l(\cos \theta), \quad (2.10)$$

where  $\delta_l$  gives the phase shift of the partial wave  $l$ . Based on Eq. (2.7), the total scattering cross-section is given by

$$\sigma(k) = \frac{4\pi}{k^2} \sum_{l=0}^{\infty} \underbrace{(2l+1) \sin^2 \delta_l}_{\sigma_l(k)}. \quad (2.11)$$

From Eq. (2.9) we can see that the partial waves with  $l > 0$  experience an effective potential  $\tilde{V}(r)$  that includes a (repulsive) centrifugal barrier  $\frac{\hbar^2 l(l+1)}{2Mr^2}$ . Consequently, the  $l = 0$  (s-) wave is dominant over all partial waves (in the absence of resonance phenomena for  $l > 0$ ). Here it is convenient to rewrite the scattering amplitude as

$$f(k, \theta) \approx f_0 = \frac{1}{k} (e^{i\delta_0} \sin \delta_0) = \frac{1}{k \cot \delta_0 - ik}. \quad (2.12)$$

For  $k \ll r_0^{-1}$  we can expand  $k \cot \delta_0$  to order  $k^2$ :

$$k \cot \delta_0 \approx -\frac{1}{a} + r_{\text{eff}} \frac{k^2}{2} + \mathcal{O}(k^4), \quad (2.13)$$

defining the *scattering length*  $a$  and *effective range*  $r_{\text{eff}}$ . Thus, the s-wave phase shift is, to first order, independent of  $k$  and is solely determined by the scattering length  $a$ . This approximation breaks down when the next order in the expansion – characterized by the effective range – becomes relevant (i.e. for  $r_{\text{eff}} \simeq 1/k$ ). For  ${}^6\text{Li}$ , the effective range is  $r_{\text{eff}} = 87 a_0$ , where  $a_0$  is

the Bohr radius [23]. Throughout the scope of this thesis, the momentum dependence of  $\delta_0$  can be omitted. The s-wave scattering cross-section is then given by

$$\sigma_s = \frac{4\pi a^2}{1 + k^2 a^2}. \quad (2.14)$$

As a consequence, even for  $|a| \rightarrow \infty$ , the scattering cross-section is capped at  $\sigma_s = 4\pi k^{-2}$  - the so called unitarity limit. This can also be seen from Eq. (2.11), as  $\sin^2 \delta_l \leq 1$ . For  $k|a| \ll 1$ , the scattering cross-section is independent of  $k$  and given by  $\sigma_s = 4\pi a^2$ . For positive scattering lengths ( $a > 0$ ), the interaction potential supports a two-body bound state with binding energy [24]

$$E_B = \frac{\hbar^2}{ma^2}. \quad (2.15)$$

The binding energy  $E_B$  is defined relative to the energy of two non-interacting particles  $E_{\text{free}}$  as  $E_B = E_{\text{free}} - E_2$ , where  $E_2$  is the total energy of two particles.

### 2.3.1 Indistinguishable particles

The discussion above holds for scattering of two distinguishable particles. For two indistinguishable particles their quantum statistics have to be taken into account, as discussed in Sec. 2.1. Specifically, when the particles are bosons, their relative wave function has to be symmetric, when they are fermions it has to be antisymmetric, that is

$$\psi_{\mathbf{k}}(\mathbf{r}) = \epsilon \psi_{\mathbf{k}}(-\mathbf{r}) \quad \text{with} \quad \begin{cases} \epsilon = +1, & \text{for bosons} \\ \epsilon = -1, & \text{for fermions.} \end{cases} \quad (2.16)$$

Taking this into account, we rewrite the scattering wave function as [21]

$$\psi_{\mathbf{k}}(\mathbf{r}) = \frac{e^{i\mathbf{k}\mathbf{r}} + \epsilon e^{-i\mathbf{k}\mathbf{r}}}{\sqrt{2}} + \frac{f(k, \theta) + \epsilon f(k, \theta - \pi)}{\sqrt{2}} \frac{e^{i\mathbf{k}\mathbf{r}}}{r}. \quad (2.17)$$

The scattering cross-section for two indistinguishable particles is then given by [21]

$$\sigma(k) = 2\pi \int_0^\pi |f(k, \theta) + \epsilon f(k, \theta - \pi)|^2 \sin \theta d\theta. \quad (2.18)$$

Considering the  $(-1)^l$  parity of the Legendre polynomials (i.e.  $P_l(\theta - \pi) = (-1)^l P_l(\theta)$ ), we can see that only the partial waves with even  $l$  contribute to the scattering of indistinguishable bosons. For fermions, only odd partial waves contribute. In both cases, the contribution of the

contributing partial waves is doubled, resulting in

$$\sigma(k) = \frac{8\pi}{k^2} \sum_{l \text{ even}} \sigma_l(k) \stackrel{l=0}{=} \frac{8\pi a^2}{1 + k^2 a^2} \quad (\text{bosons}) \quad (2.19)$$

$$\sigma(k) = \frac{8\pi}{k^2} \sum_{l \text{ odd}} \sigma_l(k) \stackrel{l=0}{=} 0 \quad (\text{fermions}) \quad (2.20)$$

$$\sigma(k) = \frac{4\pi}{k^2} \sum_l \sigma_l(k) \stackrel{l=0}{=} \frac{4\pi a^2}{1 + k^2 a^2} \quad (\text{distinguishable particles}). \quad (2.21)$$

Consequently, in the case of a spherically symmetric interaction potential and in the absence of higher partial wave resonance, indistinguishable fermions are non-interacting. In our experiment we use fermions in two different hyperfine states (see Section 2.2) - these are then distinguishable particles that interact via s-wave interactions.

### 2.3.2 Effective potential

The VdW interactions are characterized by the (rotationally symmetric) interaction potential

$$V(\mathbf{r}) = -\frac{C_6}{r^6}, \quad (2.22)$$

where  $r$  is the inter-particle distance and  $C_6$  is the VdW coefficient. The characteristic length scale  $r_0$  of the VdW potential is given by

$$r_0 = \left( \frac{2MC_6}{\hbar^2} \right)^{1/4}. \quad (2.23)$$

As seen in the introduction of the scattering problem, as long the mean interparticle spacing far exceeds  $r_0$ , the exact details of the interaction potential are insignificant. It is then convenient to replace the complicated VdW interaction potential with an effective zero range potential

$$V_{\text{eff}}(r) = \underbrace{\frac{4\pi\hbar^2 a}{M}}_{g_{3D}} \delta^{(3)}(r) \quad (2.24)$$

where  $\delta^{(3)}(r)$  is the normalized Dirac Delta function. This effective potential accurately reproduces the asymptotic scattering behavior. For two colliding  ${}^6\text{Li}$  atoms,  $r_0 \approx 6 \times 10^2 a_0 = 30 \text{ nm}$  [25]. The typical interparticle spacing in our experiment is on the order of  $r \approx 1 \times 10^4 a_0 = 500 \text{ nm}$ . Therefore, we can replace the VdW with the effective zero range potential.

### 2.3.3 Scattering in (quasi-)2D

The measurements carried out in the scope of this thesis were all performed in a quasi-2D geometry. While the concepts discussed above also hold for a 2D geometry, there are some key differences between the 2D and 3D case, which we will discuss in this section. *The discussion is based on [26, 27].*

As in 3D (see Eq. (2.5)), the total wave function in 2D is given by the superposition of an

incoming plane wave and an outgoing circular wave

$$\psi_{\mathbf{k}}(\mathbf{r}) \xrightarrow{r \rightarrow \infty} e^{i\mathbf{k}\mathbf{r}} + f(k, \theta) \frac{e^{ikr}}{\sqrt{r}}. \quad (2.25)$$

The partial wave expansion of  $f(k, \theta)$  in 2D is

$$f(\mathbf{k}) = \sqrt{\frac{2i}{k\pi}} \sum_{l=0}^{\infty} (2 - \delta_{l0}) \cos(l\theta) e^{i\delta_l} \sin \delta_l, \quad (2.26)$$

with the Kronecker delta  $\delta_{l0}$ .

In absence of higher order partial wave resonances, we can again assume that  $f(\mathbf{k}) \approx f_0(k)$ , i.e. we take only the  $l = 0$  partial wave into account. Analogously to Eq. (2.7) the scattering cross-section is obtained by integrating  $|f_0(k)|^2$  over all scattering angles. This results in

$$\sigma(k) = \frac{4}{k} \sin^2 \delta_0(k). \quad (2.27)$$

Note that the scattering cross-section in 2D has the dimension of a length, whereas it has the dimension length squared in 3D. The maximum s-wave scattering cross-section for a given  $k$  in 2D is  $\max(\sigma(k)) = 4/k$ .

To obtain the low energy behavior of the phase shift, we rewrite

$$f_0(k) = \sqrt{\frac{2i}{k\pi}} e^{i\delta_0} \sin \delta_0 = \sqrt{\frac{2}{k\pi}} \frac{1}{\cot \delta_0 - i} \quad (2.28)$$

and expand it as

$$\cot \delta_0 = \frac{2}{\pi} \ln(ka_{2D}) + \mathcal{O}(k^2) \quad (2.29)$$

where we define  $a_{2D}$  as the 2D scattering length. In contrast to the 3D system, the scattering phase shift and the scattering amplitude tend to zero as  $k \rightarrow 0$  in 2D. The scattering cross-section is given by

$$\sigma(k) = \frac{4}{k} \left( 1 + \frac{4}{\pi^2} \ln^2(ka_{2D}) \right)^{-1}. \quad (2.30)$$

The maximum scattering cross-section (for a given  $k$ ) is obtained for  $\ln(ka_{2D}) = 0$ , i.e. for  $a_{2D} = k^{-1}$ .

In 2D an interaction potential  $V(r) < 0$  of any depth supports a bound state [22, 24]. The energy of this bound state is given by

$$E_B = \frac{\hbar^2}{ma_{2D}^2}. \quad (2.31)$$

As a bound state exists for all values of  $a_{2D}$  – unlike in the 3D system, where it only exists for  $a > 0$  – we can use  $E_B$  in lieu of  $a_{2D}$ , when convenient.

As the scattering properties are always logarithmically dependent on both  $k$  and  $a_{2D}$ , we use  $\ln(ka_{2D})$  as the *interaction parameter* to describe scattering in 2D. Analogously to the 3D

system, we can introduce an effective interaction potential with

$$V_{\text{eff}} = \frac{-2\pi\hbar^2}{\underbrace{M \ln(ka_{2D})}_{g_{2D}}} \delta^{(2)}(r). \quad (2.32)$$

The experiments carried out within the scope of this thesis are performed in a quasi-2D geometry. The contribution of the third direction is essentially frozen out, as the atoms are tightly confined along one spatial dimension. In a harmonic potential with angular frequency  $\omega_z$  in the strongly confined direction, this is achieved when  $\hbar\omega_z$  is larger than all other energy scales of the system. Then the dynamics take place only in a 2D plane, perpendicular to the direction of tight confinement and the low energy (low  $k$ ) physics is essentially 2D. However, the van der Waals interaction range  $r_0 \approx 30$  nm is always significantly below the length scale associated to  $\omega_z$  ( $l_{\text{HO},z} \approx 400$  nm). Hence, locally scattering is always 3D. The asymptotic scattering behavior in quasi-2D can be described by a 2D model, where the effective 2D scattering length is set by the confinement in the tightly confined direction (via  $l_{\text{HO},z}$ ) and the 3D scattering length  $a$ . The 2D scattering length is then given by [26, 28]

$$a_{2D} = l_{\text{HO},z} \sqrt{\frac{\pi}{A}} \exp\left(-\sqrt{\frac{\pi}{2}} \frac{l_{\text{HO},z}}{a}\right), \quad (2.33)$$

with  $A = 0.905$ .

### 2.3.4 Feshbach resonances

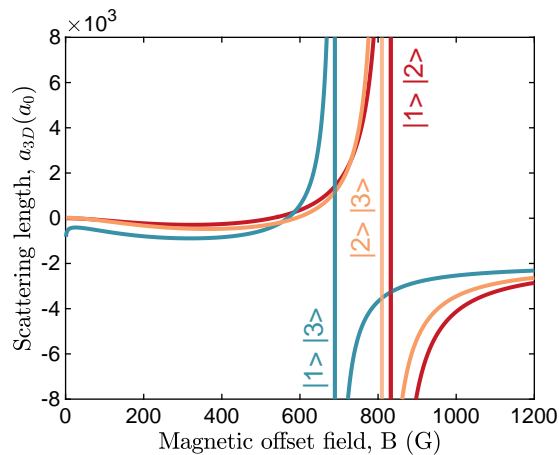


**Figure 2.3: Feshbach resonances of  ${}^6\text{Li}$ .**  ${}^6\text{Li}$  exhibits a broad Feshbach resonance for each combination of the three lowest hyperfine states, allowing free and accurate tunability of the 3D scattering length. Plotted data from [23].

One of the distinguishing features of many cold atom experiments is that the interaction parameter is freely tuneable via (magnetic) Feshbach resonances. A Feshbach resonance occurs when the energy of a bound molecular state approaches the energy of the scattering state. Here, even weak coupling between the scattering states and the bound state can lead to a significant phase shift of the scattered wave function. *The following discussion is based on [20, 22, 29].*

The interaction potential of two atoms depends on the relative orientation of their electronic spin - i.e. whether they are in a singlet or triplet state. Let us consider two atoms initially in a triplet state. If there is no coupling to the singlet state, the scattering process will result in a fixed phase shift  $\delta_0$ . However, the phase shift can be altered by coupling to a bound state in the molecular potential of the spin singlet state. This state is commonly referred to as 'closed channel' as its energy at large particle separations exceeds the energy of the atoms in the triplet state ('open channel'). Due to energy conservation, the atoms have to remain in the open channel after scattering. Nonetheless, when the spin singlet exhibits a bound state close to the energy of the incoming atoms, virtual coupling to this bound state can significantly alter the scattering phase shift.

A magnetic Feshbach resonance occurs when the two channels have different magnetic moments. Then, the energy of the bound state relative to the energy of the incoming atoms can be tuned by the magnetic offset field. The scattering length as a function of the magnetic field  $B$  around a magnetic Feshbach resonance (located at  $B = B_0$ ) is given by [30]

$$a(B) = a_{\text{bg}} \left( 1 - \frac{\Delta}{B - B_0} \right), \quad (2.34)$$

where  $a_{\text{bg}}$  is the background scattering length and  $\Delta$  is the distance from  $B_0$  to the magnetic field at which  $a(B)$  crosses zero.

Here,  ${}^6\text{Li}$  is a particularly good choice of atomic species as it features a broad magnetic Feshbach resonance, allowing free and accurate tunability of the s-wave scattering properties of the lower three hyperfine states (see Section 2.2). The Feshbach resonances were measured by Zuern et al. in [23] and are shown in Fig. 2.3. For all measurements performed in this thesis, we utilize a  $|1\rangle |3\rangle$  mixture. This Feshbach resonance is located at a field of  $B_0 = 689.7 \text{ G}$ , with a width of  $\Delta = -166.6 \text{ G}$ . The background scattering length is  $a_{\text{bg}} = -1770 a_0$ .

## 2.4 Optical Dipole Traps

*This section aims to give a short introduction on optical dipole traps, based on [31]. We refer the reader to this reference for a comprehensive discussion of optical dipole traps.*

Optical dipole traps make use of light far detuned from any transition of the atom to trap atoms while limiting residual photon scattering. Consider an atom placed in a laser field: Here, the electric field ( $\mathbf{E}$ ) of the laser induces a dipole moment  $\mathbf{p}$  in the atom. The interaction potential of the induced dipole in the driving field is given by

$$U_{\text{dip}} = -\frac{1}{2} \langle \mathbf{p} \mathbf{E} \rangle, \quad (2.35)$$

where  $\langle \dots \rangle$  denotes the time average over the rapidly oscillating terms. The amplitude of  $\mathbf{p}$  is directly proportional to the amplitude of  $\mathbf{E}$  with a complex proportionality factor  $\alpha$ . The potential can then be expressed as

$$U_{\text{dip}} = -\frac{1}{2\epsilon_0 c} \text{Re}(\alpha) I, \quad (2.36)$$

where  $I = 2\epsilon_0 c |\mathbf{E}|^2$  is the field intensity. The scattering rate (i.e. the rate at which the atom absorbs and reemits photons from the laser beam) is given by

$$\Gamma_{\text{sc}} = \frac{1}{\hbar\epsilon_0 c} \text{Im}(\alpha) I. \quad (2.37)$$

The proportionality factor  $\alpha$  (commonly referred to as the complex polarizability) can be calculated within the (classical) Lorentz model, modelling the motion of the electron bound to the nucleus as a driven, damped harmonic oscillator with eigenfrequency  $\omega_0$ , driving frequency  $\omega$  and damping rate  $\Gamma$  - the natural linewidth of the transition. The polarizability is then given by

$$\alpha = \frac{e^2}{m_e} \frac{1}{\omega_0^2 - \omega^2 - i\omega\Gamma}. \quad (2.38)$$

When the atom can be described as an ideal two-level system and the detuning  $\Delta \equiv \omega - \omega_0$  fulfills  $|\Delta| \ll \omega_0$  (permitting the rotating wave approximation), the dipole potential and scattering rate are given by

$$U_{\text{dip}} = \frac{3\pi c^2 \Gamma}{2\hbar\omega_0^3 \Delta} I(\mathbf{r}) \quad (2.39)$$

and

$$\Gamma_{\text{sc}} = \frac{3\pi c^2}{2\omega_0^3} \left( \frac{\Gamma}{\Delta} \right)^2 I(\mathbf{r}), \quad (2.40)$$

respectively.

Here, we can see two essential features of optical dipole traps. Firstly, the prefactor of the potential depends on the sign of the detuning. When the frequency  $\omega$  is below the atomic resonance ('red-detuned'), the dipole potential is negative and the potential minima are found at the intensity maxima ('the atoms are attracted by high intensities'). When  $\omega > \omega_0$  ('blue detuned'), the potential minima are found at the intensity minima ('the atoms are repelled by high intensities'). Secondly, we can see that the scattering rate  $\Gamma_{\text{sc}} \propto I\Delta^{-2}$ , while the potential depth  $U_{\text{dip}} \propto I\Delta^{-1}$ . Hence, we can minimize the scattering rate at a given trap depth by choosing a higher detuning and higher intensity over a smaller detuning and lower intensity. Within the scope of this thesis, we utilize only optical dipole traps at a wavelength of  $\lambda = 2\pi c/\omega = 1064 \text{ nm}$ , red-detuned from both the D1 and D2 line of  ${}^6\text{Li}$  ( $\lambda_0 \approx 2\pi c/\omega_0 = 671 \text{ nm}$ ) (see Sec. 2.2).



# 3 | Experimental setup and techniques

Yes, of course duct tape works in a near-vacuum. Duct tape works anywhere. Duct tape is magic and should be worshiped.

ANDY WEIR  
*The Martian, 2001*

This chapter introduces the experimental methods used to cool  ${}^6\text{Li}$  to quantum degeneracy and the techniques used to obtain few fermionic atoms in the ground state of a quasi-two-dimensional harmonic oscillator potential – the starting point for all experiments discussed in the scope of this thesis. Beyond that, we discuss the single-atom and spin-resolved imaging technique employed to investigate the system.

*More information on the experimental setup can be found in previous PhD thesis [32–34]. A detailed discussion of the imaging scheme can be found in [35–37]. An in-depth treatment of the newly implemented matterwave magnification setup can be found in Chapter 4.*

## 3.1 Reaching quantum degeneracy

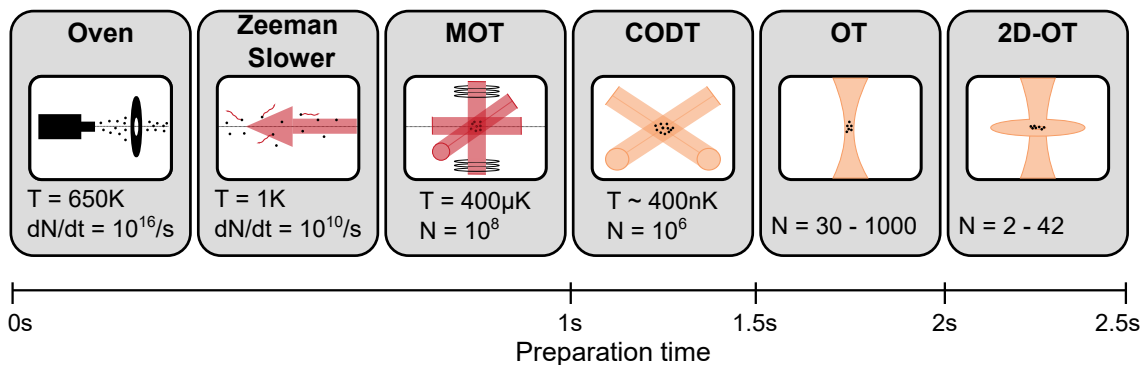


**Figure 3.1: Schematic sketch of the experimental sequence.** The experimental cycle starts in the oven, where a collimated beam of  ${}^6\text{Li}$  atoms is produced. The atomic beam is decelerated in a Zeeman slower, allowing us to capture the atoms in the MOT. We load the MOT in this manner for around 1 s. Subsequently, the atoms are transferred to the CODT where we evaporatively cool them for 500 ms, followed by a fast evaporation ( $\approx 20$  ms) to quantum degeneracy in the OT. We then perform a transfer to a quasi-2D geometry. The entire experimental cycle takes 2.5 s. Figure adapted from [33].

The experimental cycle used to obtain few fermionic  ${}^6\text{Li}$  in the ground state of a quasi-2D harmonic oscillator potential is illustrated in Figure 3.1. The experimental sequence starts in the oven, where isotope enriched  ${}^6\text{Li}$  is heated to a temperature of  $T \approx 650$  K. The mean

velocity of the atoms –  $v_{\text{rms}} = \sqrt{8k_B T / \pi m} = 1600 \text{ m s}^{-1}$  – at this stage is comparable to the top speed of hypersonic, rocket-powered aircraft. The oven produces a collimated beam of atoms with a flux of  $dN/dT \approx 10^{16} \text{ s}^{-1}$ . This atomic beam is decelerated by a counter-propagating laser beam, resonant to the  $D_2$ -line (see Sec. 2.2). When an atom absorbs a photon, its velocity in direction of the atomic beam is reduced by  $v \approx 0.1 \text{ m s}^{-1}$ . Due to the Doppler shift, this decrease in velocity shifts the atomic transition out of resonance. We compensate this effect by applying a magnetic field gradient, decreasing along the beam direction. In this way, the Zeeman shift compensates the Doppler shift, ensuring that the atomic transition stays on resonance with the laser beam – hence the name Zeeman slower [38–41]. The thermal velocity at the final stage of the Zeeman slower is  $v_{\text{rms}} = 50 \text{ m s}^{-1}$  (comparable to a fast regional train).

With this final velocity, the atoms are slow enough to be captured in the magneto-optical trap (MOT). The MOT is made up of three pairs of retro-reflected laser beams – red-detuned to the  $D_2$ -line – and a spatially dependent magnetic field.

Let us first consider the force acting upon an atom in the presence of two red-detuned counter-propagating beams in a one-dimensional (1D) geometry [42]. When the atom is at rest, the forces exerted by the two laser beams exactly cancel each other. However, if the atom is moving in direction of one of the two red-detuned laser beams, the counter-propagating beam becomes closer to resonance due to the Doppler shift, while the co-propagating beam is detuned even further. Hence, the force acting upon the atom is velocity dependent, equivalently to a friction force. This setup is commonly referred to as an *optical molasses* [43].

The counter propagating laser beams alone do not form a trap. To obtain a trap, the force additionally needs to be spatially dependent. This is achieved by introducing a spatially dependent magnetic field which gives rise to a spatially dependent Zeeman shift. By an appropriate choice of beam polarizations, one can achieve a restorative, dissipative force, that confines and cools the atoms [44]. The minimum temperature that can be achieved in the MOT is set by the Doppler temperature  $T_D = \hbar\Gamma/2k_B \approx 140 \mu\text{K}$ . Here  $\Gamma/2\pi = 5.872 \text{ MHz}$  is the natural linewidth of the optical transition [19]. At low offset fields the natural linewidth exceeds the hyperfine splitting (4.4 MHz) of the  $^2P_{3/2}$  state. Thus, light resonant to the  $|^2S_{1/2}, F = 3/2\rangle \rightarrow |^2P_{3/2}, F = 5/2\rangle$  transition is also resonant to the  $|^2S_{1/2}, F = 3/2\rangle \rightarrow |^2P_{3/2}, F = 3/2\rangle$  transition. Atoms in  $|^2P_{3/2}, F = 3/2\rangle$  can also decay to  $|^2S_{1/2}, F = 1/2\rangle$ . Consequently, light resonant to both the  $|^2S_{1/2}, F = 3/2\rangle \rightarrow |^2P_{3/2}, F = 5/2\rangle$  (cooler) transition and the  $|^2S_{1/2}, F = 1/2\rangle \rightarrow |^2P_{3/2}, F = 3/2\rangle$  (repumper) transition is needed to close the optical transition. This is the case for both the MOT and the Zeeman slower. A detailed discussion of the MOT and Zeeman slower setup in our experiment can be found in [45].

To further cool the sample, we transfer the atoms from the MOT to a crossed-beam optical dipole trap (CODT). The CODT is formed in the intersection of two laser beams with a wavelength of  $\lambda = 1064 \text{ nm}$  and a power of  $P = 200 \text{ W}$ . To optimize this transfer, we first spatially compress the MOT by reducing the detuning to the optical transition. Thereafter, we reduce the power in the repumper beam before reducing that of the cooler beam to ensure that the atoms accumulate in the lower hyperfine manifold. At non-zero magnetic field, the atoms then populate states  $|1\rangle$  and  $|2\rangle$ . We jump the magnetic offset field (produced by the so-called Feshbach coils) from  $B = 0 \text{ G}$  to  $B = 795 \text{ G}$ , and apply a 50 ms (exceeding the decoherence

---

<sup>1</sup>At this temperature the thermal velocity is  $v_{\text{rms}} = 2.75 \text{ km h}^{-1}$  – I can finally easily outwalk the atoms!

time) long RF pulse to balance the population in states  $|1\rangle$  and  $|2\rangle$ . Subsequently, we ramp the magnetic offset field to  $B = 580$  G (ensuring minimal interactions between states  $|1\rangle$ ,  $|2\rangle$  and  $|3\rangle$ ), where we transfer atoms from hyperfine state  $|2\rangle \rightarrow |3\rangle$  via a Landau-Zener passage.

We evaporatively cool the balanced mixture by slowly lowering the depth of the CODT, allowing the hottest atom to escape from the trap. Elastic collisions between the remaining atoms reestablish thermal equilibrium at a lower temperature. We ensure fast thermalization, i.e. high elastic collision rates, by setting the magnetic offset field to  $B = 795$  G, slightly above the Feshbach resonance of the  $|1\rangle - |3\rangle$  mixture. After an evaporation time of  $t \approx 500$  ms, the sample is cold enough so that we can transfer around 1000 atoms into a tightly focused optical tweezer (OT).

The OT is created by a Gaussian beam with a wavelength of  $\lambda = 1064$  nm, focused onto the atomic plane with a high-resolution microscope objective with a numerical aperture (NA) of 0.6 and a focal length  $f = 20.3$  mm. For more information on the objective see [46]. The Gaussian beam is shaped by a liquid crystal spatial light modulator (SLM) – placed in the Fourier plane – allowing us to tailor the optical potential. More information on the SLM setup can be found in [32, 33].

The waist of the tightly focused optical tweezer is close to the diffraction limit of the objective ( $w \approx 1$   $\mu\text{m}$ ). The axial trap frequency is on the order of  $\omega_z/2\pi = 100$  kHz, the ratio of the trap frequencies in the three spatial directions is  $\omega_x : \omega_y : \omega_z = 7 : 7 : 1$ . The geometry of the tightly focused optical tweezer is consequently quasi-1D. The high densities in the OT increases the thermalization rate significantly. We can evaporatively cool the atoms to quantum degeneracy ( $T/T_F \approx 0.05$ ) in  $t \approx 10$  ms. At the end of this evaporation sequence around 300 atoms remain in the OT.

## 3.2 Deterministic state preparation

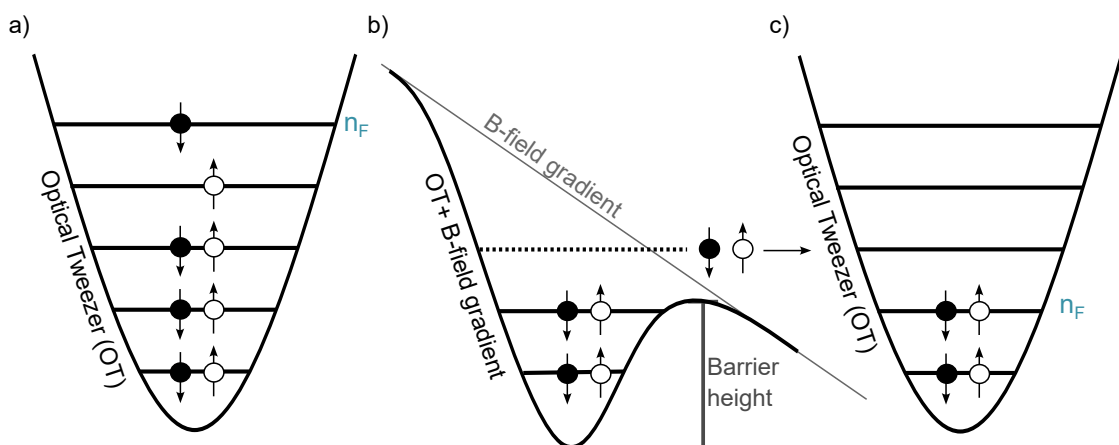


**Figure 3.2: Conceptual illustration of the spilling protocol.** a) We prepare a degenerate, spin-balanced Fermi gas in a 1D harmonic oscillator potential. b) We apply a magnetic field gradient and lower the trap depth. We can control the number of bound states remaining in the potential by altering the barrier height (set by the magnetic field gradient and the trap depth). c) The remaining atoms occupy the ground state of the optical potential - a discrete quantum state. Figure adapted from [47].

All experiments conducted in the scope of this thesis are based on deterministic preparation of few fermions in the ground state of a quasi-2D harmonic oscillator potential. This potential is created by two optical traps: the (weaker) radial ( $r$ - direction) confinement is provided by the optical tweezer, the (strong) axial ( $z$ - direction) confinement is provided by a single layer of a standing wave optical dipole trap (SWT). The SWT is created by the interference of two elliptical Gaussian beams under an angle of  $14^\circ$ . The resulting potential is a stack of quasi-two dimensional potentials, where the central layer has a radial and axial trap frequency of  $(\omega_{\text{SWT},r}, \omega_{\text{SWT},z})/2\pi = (16.9(1), 7432(3))$  Hz, respectively. The waist in radial direction is on the order of  $600 \mu\text{m}$ , the separation between the layers is  $4.4 \mu\text{m}$ . More information on the SWT can be found in [34].

To transfer the atoms from the 1D geometry of the tightly focused optical tweezer to a quasi-2D geometry, we first reduce the number of atoms in the tightly focused OT. This is done to ensure that we only load a single layer of the SWT. Here, we perform the spilling procedure first discussed by Serwane et al. in [47]: Starting out with a degenerate Fermi gas of around 300 atoms in the tightly focused OT we apply a magnetic field gradient of  $\delta B/\delta z = 23 \text{ G cm}^{-1}$  along the  $z$ -direction and lower the power of the OT to  $P_{\text{spill}}$ . We can tune the number of bound states remaining in the potential by altering  $P_{\text{spill}}$ . The power is kept at  $P_{\text{spill}}$  for  $t = 40 \text{ ms}$  before we increase it to its original value and adiabatically turn off the magnetic field gradient. This sequence is sketched in Figure 3.2. We set  $P_{\text{spill}}$  such that we end up with around 30 – 50 atoms in the OT.

Subsequently, we adiabatically ramp the SWT on and simultaneously increase the waist of the OT from  $1 \mu\text{m}$  to  $5 \mu\text{m}$ . This done by changing the aperture phase pattern on the SLM in a single frame update. The slow response time of the liquid crystals ( $\approx 80 \text{ ms}$ ) ensures a smooth aperture ramp. To further reduce the extent of the cloud, we increase the interaction strength (specifically, we set the magnetic offset field to  $705 \text{ G}$ ). The strong interactions also ensure that the atoms remain in the ground state during the transfer [33].

The combined potential of SWT and OT is referred to as 2D optical tweezer (2D-OT). As the axial confinement of the OT is far weaker than that of the SWT, the axial trap frequency is set by the SWT and vice versa for the radial confinement. The radial trap frequency is tuneable in the range  $\omega_r/2\pi = 100 - 3000 \text{ Hz}$  by using different aperture phase patterns on the SLM. Typically, we use a radial trap frequency of  $\omega_r/2\pi \approx 1000 \text{ Hz}$ . With the axial trap frequency of  $\omega_z/2\pi \approx 7432(3) \text{ Hz}$ , the resulting potential is quasi-2D with an aspect ratio of  $\omega_r : \omega_z = 1 : 7$ .

To deterministically prepare ground state configurations in this quasi-2D geometry, we employ a similar technique as in 1D: We apply a magnetic field gradient of  $\delta B/\delta z = 70 \text{ G cm}^{-1}$  and lower the optical power of the OT. The power of the SWT remains constant. The number of bound states remaining is once again set by the power of the OT. Fig. 3.3a) shows the measured atom number as a function of the optical power of the OT. The stable plateaus correspond to closed shell configurations of the 2D harmonic oscillator potential sketched in Fig. 3.3b. The  $n$ th level of the 2D harmonic oscillator exhibits an  $n + 1$ -fold degeneracy. This results in closed shell (i.e. all states up to and including  $n$  are occupied) configurations of 1, 3, 6, 10, 15, 21, .. atoms per spin state. We achieve a preparation fidelity of 80 % for a system of 6 atoms each in states  $|1\rangle$  and  $|3\rangle$  (denoted as 6+6).

We can also prepare higher atom numbers of up to [42] atoms (21 atoms per spin state),

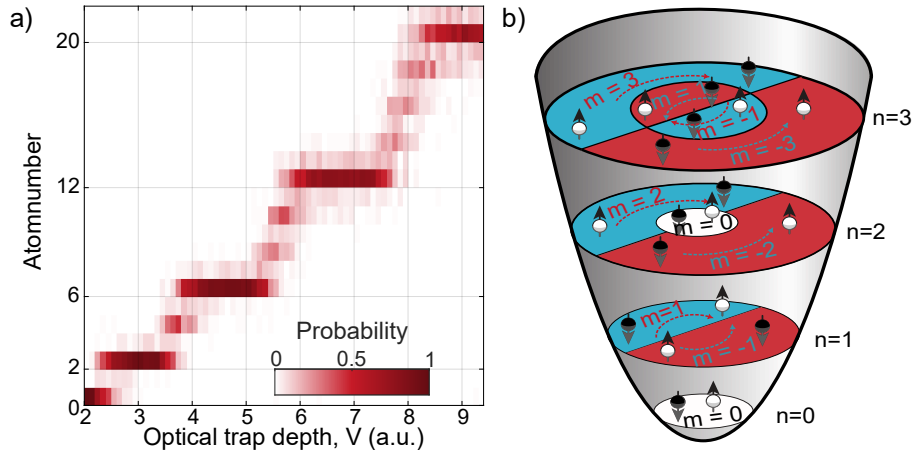


**Figure 3.3: Preparing closed shell configurations in an isotropic 2D harmonic oscillator potential.** We prepare the system the ground state of a rotationally symmetric, 2D harmonic oscillator potential. The harmonic oscillator levels, labelled by their principal quantum number  $n$  and the angular momentum quantum number  $m$  are sketched in b) . Here we also marked the closed shell configuration of 10 + 10 atoms. a) shows the number of atoms remaining in the trap as a function of the optical trap depth. We can see stable plateaus corresponding to closed shell configurations of the harmonic oscillator potential.

corresponding to six filled shells of the harmonic oscillator potential. To prepare these in a quasi-2D-geometry, we start with around 70 atoms before the 2D-transfer. During the 2D-transfer, we reduce the radial trap frequency of the OT to around  $\omega_r/2\pi = 350$  Hz, allowing us to remain in a quasi-2D geometry. The resulting atom number as a function of the optical trap depth is shown in Fig. 3.4. We observe plateaus corresponding to the closed shell configurations. However, the preparation fidelity is greatly reduced as holes in the Fermi distribution due to non-zero temperature become more likely. In addition, it becomes more difficult to discern different atom numbers.

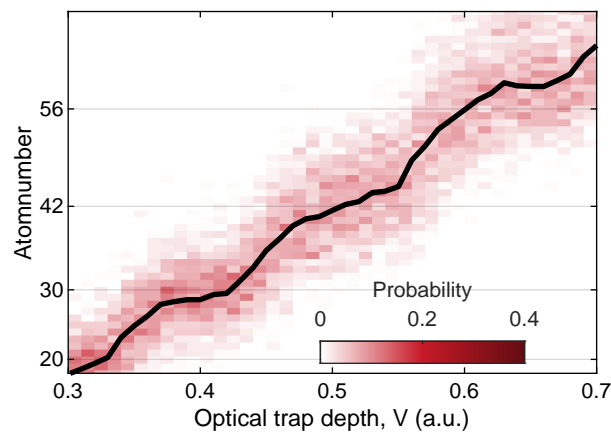


**Figure 3.4: Preparing higher atom numbers.** Atom number remaining in the 2D-OT as a function of the optical trap depth. The black line marks the mean atom number. We observe plateaus at the atom numbers corresponding to filled shells of the 2D harmonic oscillator potential.

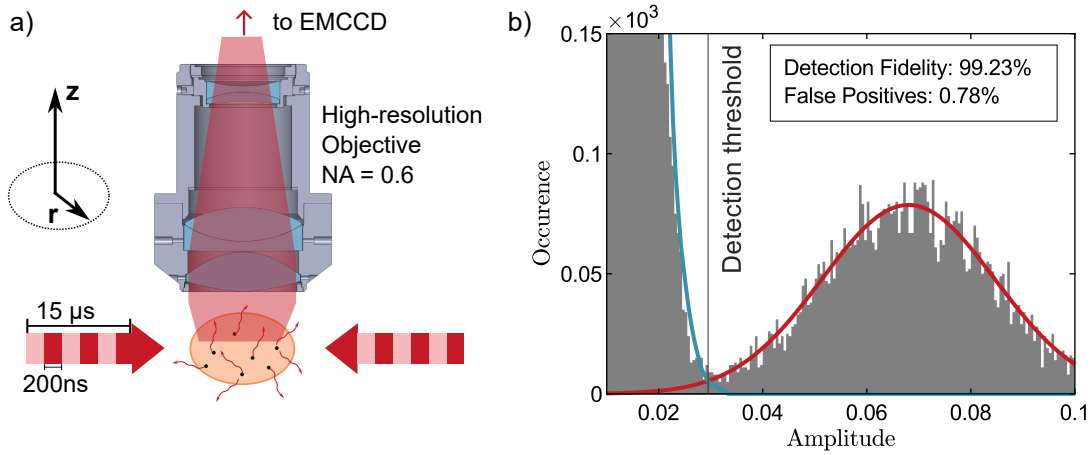


**Figure 3.5: Single atom resolved fluorescence imaging.** a) We illuminate the atoms with two counter-propagating laser beams, subsequently turned on for 200 ns. We collect the spontaneously emitted photons with the high resolution objective and image them onto an EM-CCD camera. In this process, around 8 % of the emitted photons are measured by the camera. b) We identify the atoms by performing a low pass filter of the resulting image. The histogram shows the amplitudes of the local maxima in 2000 filtered images, each containing  $\approx 6$  atoms. The randomly distributed noise leads to peaks with low amplitude in the low passed atoms. The photons emitted by atoms form a cluster, leading to high amplitudes. The two peaks are clearly separable. a) adapted from [35].

### 3.3 Single atom resolved imaging

We utilize a fluorescence imaging technique to image the atom positions with single atom and spin resolution in free space [48, 49]. Our imaging scheme is sketched in Fig. 3.5a). To image the atoms, they are illuminated with two counter-propagating laser beams, resonant to the  $D2$  line, driving a  $\sigma^-$  transition from  $m_j = -1/2$  to  $m_j = -3/2$ . An atom absorbing a photon from one of the two laser beams and then reemitting a photon experiences a momentum transfer of  $\hbar k$  by the absorption of the photon and an additional  $\hbar k$  due to the emission. The momentum transferred by stimulated absorption or emission is directional, with a direction set by the incident laser beam. Using two counter-propagating beams thus minimizes the effective momentum imparted by stimulated absorption or emission. The two beams are alternately pulsed on for a time of 200 ns, to avoid a rapid diffusion of the atoms at slight power imbalance (we refer the reader to [50] for an in-depth treatment of this effect). The direction of the momentum imparted by the spontaneous emission is random, with a distribution set by the dipole radiation pattern [36]. In our case, the quantization axis is oriented along the axial ( $z$ -) direction. This results on the one hand in an increased scattering probability in  $z$ -direction, i.e. in direction of the microscope objective. On the other hand, the dipole radiation pattern is radially symmetric in the atom plane. The momentum transfer by the spontaneous emission can not be balanced and causes a random walk of the atoms.

To minimize the diffusion of the atom due to this random walk, we minimize the time required to collect enough photons to identify the atom with high fidelity. This entails on the one hand maximizing the number of photons *scattered* by the atoms. On the other hand, we need to maximize the number of photons *detected* by our camera.

The photon scattering rate

$$\Gamma_{\text{sc}} = \frac{\Gamma}{2} \frac{s}{1 + s + (2\delta/\Gamma)^2} \quad (3.1)$$

is set by the natural linewidth  $\Gamma$ , the detuning from the transition  $\delta$  and the intensity, given in units of the saturation intensity  $s = I/I_{\text{sat}}$ . Hence, the photon scattering rate is capped at half the natural linewidth,  $\Gamma/2 = 18.4 \text{ photons}/\mu\text{s}$ . We typically work at intensities of  $s \approx 8$ , resulting in  $\Gamma_{\text{sc}} \approx 16 \text{ photons}/\mu\text{s}$ .

To optimize the number of photons detected by our camera, we utilize the high NA objective – used also to project the OT onto the atoms – to collect the scattered photons. Considering all photons that remain undetected due to the NA, the dipole radiation pattern and imperfect optics, approximately 10 % of the scattered photons reach our camera. We utilize an electron multiplying CCD camera (EM-CCD) (Nüvü HNü 512) with a high quantum efficiency ( $q = 95 \%$  at  $\lambda = 671 \text{ nm}$ ) and choose a  $5\sigma$  detection threshold, setting the photo-electron detection fidelity to 82 %. This results in an effective scattering rate of 1.24 photons/ $\mu\text{s}$ . For more details see [36].

To discern the atom signal from unwanted photo-electrons – created either by clock induced charges (CICs), or remaining background light – we apply a low-pass filter with a width of  $\sigma = 5 \text{ px}$  to each image. While the CICs are randomly distributed, the photons emitted from an atom form a cluster – the low pass filter thus allows us to discern the ‘real’ signal from the unwanted background. A histogram of the peak amplitudes of 2000 filtered images, each containing  $\approx 6$  atoms is shown in Fig. 3.5b). Here we used an imaging time of 15  $\mu\text{s}$ , resulting in  $\approx 19 \text{ photons/atom}$  detected by the camera. We observe a bimodal distribution, where the signal at low amplitudes stems from the randomly distributed noise, while the signal at high amplitudes stems from photon clusters. The separation of the two peaks determines the ability to distinguish noise from a true atom signal. We fit the low amplitude signal with an exponential function and the high amplitude signal with a Gaussian function. The detection threshold – defined as the amplitude at which a peak is identified as an atom – is set at the intersection of these two curves. Here, the peaks are well separated, enabling correct atom identification with a probability of 99.23 %. The probability of falsely identifying noise as an atom is 0.78 %, determined by the area of the exponential curve above the threshold.

Due to the random walk of the atoms during the imaging time, the effective imaging resolution is worse than that of the microscope objective. We determine the point spread function (PSF) of a single atom by repeated measurements of the atom position. The resulting distribution is shown in Fig. 3.6. The root-mean-square (RMS) width of the PSF in  $x$ –direction, i.e. along the direction of the imaging beams is broader than the RMS width in  $y$ –direction. We believe this effect originates from events where a photon is absorbed from one beam and subsequently undergoes stimulated emission into the counter-propagating beam, resulting in a momentum transfer of  $2\hbar k$  in the direction of the first beam. Because the two counter-propagating beams create a symmetric configuration, this process is equally probable in both directions. However, this symmetry is ultimately broken by the end of the imaging process. The mean RMS width of the PSF is  $\delta_{\text{psf}} = 4.9(3) \mu\text{m}$  in the atom plane. Consequently, the imaging resolution is on the same order as the system size, necessitating the implementation of a matterwave magnification scheme to be able to resolve the length scales of interest. It is discussed in-depth in Chapter 4.

To image atoms in both spin states, we take two images with a delay of 162  $\mu\text{s}$ . In the scope

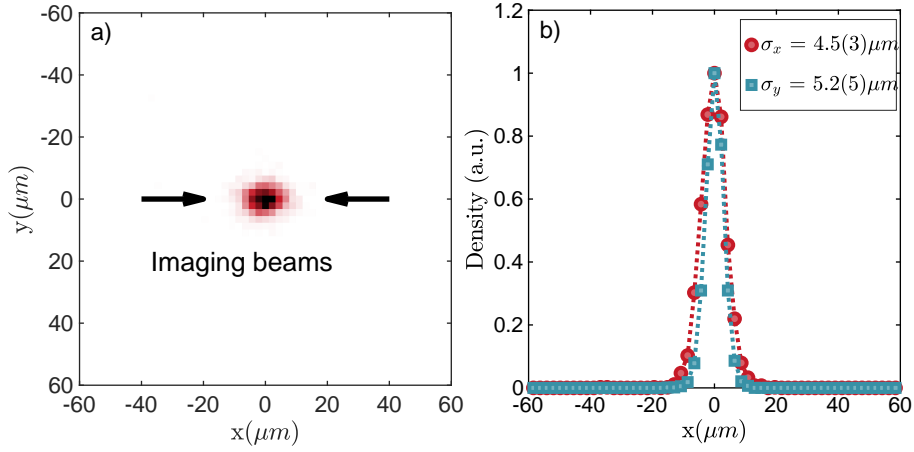


**Figure 3.6: Effective point spread function.** We show the position of a single atom, averaged over  $\approx 2400$  experimental implementations. a) shows a 2D histogram of the atom positions, the arrows mark the direction of the imaging beams. b) shows the normalized signal, integrated over one spatial direction. The RMS width is larger in direction of the imaging beams.

of this thesis, we solely image atoms in  $|3\rangle$ . When imaging atoms in  $|1\rangle$  or  $|2\rangle$ , there is a finite possibility that they decay to  $|5\rangle$  or  $|4\rangle$  during the imaging process, because the transition is not closed [19, 35]. As this limits the imaging fidelity, we instead transfer them to state  $|3\rangle$  – which exhibits a closed imaging transition – prior to imaging. Specifically to image a  $|1\rangle$ - $|3\rangle$  mixture, we first transfer atoms in state  $|3\rangle \rightarrow |4\rangle$  (see also Sec. 4.2.1) and subsequently use two RF transitions to transfer atoms from state  $|1\rangle$  to  $|3\rangle$  via  $|2\rangle$ . We then take the first image of state  $|3\rangle$  (i.e. of the atoms originally in state  $|1\rangle$ ) and subsequently transfer the atoms 'parked' in  $|4\rangle$  back to  $|3\rangle$  using a microwave (MW) transfer. After  $162\ \mu\text{s}$  we again image state  $|3\rangle$  (this time imaging the atoms originally in  $|3\rangle$ ). This sequence provides two significant benefits: First, the imaging fidelity is greatly increased as the number of scattered photons is not limited by the non-zero decay probability into another state. Second, we guard the atoms parked in  $|4\rangle$  from off-resonant scattering, as state  $|4\rangle$  is separated from state  $|3\rangle$  by  $\approx 2\ \text{GHz}$ . The lower three hyperfine states are only separated by  $80\ \text{MHz}$  - the probability for atoms in state  $|1\rangle$  or  $|2\rangle$  to scatter a photon from the imaging laser is non-zero. Due to the temporal separation of the two images, the momentum transferred by the off-resonantly scattered photon causes a broadening of the PSF in the second image. More information on the two spin state imaging scheme can be found in [48, SB1].

## 4 | Matterwave manipulation

“It has long been an axiom of mine that the little things are infinitely the most important.”

---

ARTHUR CONAN DOYLE  
*The Adventures of Sherlock Holmes*

Single-particle resolved imaging techniques have revolutionized our ability to probe microscopic observables, providing access to higher-order correlation functions that are essential for understanding many-body quantum systems. However, when the spatial resolution of the imaging system approaches the mean interparticle spacing, direct imaging becomes impossible. In this regime, various techniques have been developed to magnify the system before imaging [51, 52]. Crucially, any magnification method must preserve the correlations of the initial state to ensure accurate reconstruction of the system’s properties.

In our experiment, we utilize a fluorescence imaging technique, allowing us to image the atoms in real space with single particle and spin resolution. However, the resolution of this imaging technique is on the same order as our initial system size. To overcome this limitation, we implement a magnification scheme based on phase-space rotations in potentials tailored for accurate magnification of all relevant length scales. By combining two such rotations in potentials with different trap frequencies, we magnify the matterwave in real space by a factor of approximately 50. Alternatively, by performing a single phase-space rotation, we map the initial momentum space wave function onto real-space, granting direct access to the momentum distribution. These matterwave optics techniques enable us to explore correlations and microscopic observables in both real and momentum space in a continuous system.

*The experimental results on the matterwave magnifier presented in this chapter are adapted from the publication*

*”Magnifying the Wave Function of Interacting Fermionic Atoms”*  
Sandra Brandstetter\*, Carl Heintze\*, Keerthan Subramanian\*,  
Paul Hill, Philipp M. Preiss, Maciej Gałka, Selim Jochim  
arXiv: [2409.18954](https://arxiv.org/abs/2409.18954) (2024) [SB2]

*and are presented with modifications and additions.*

## 4.1 Rotating in phase space

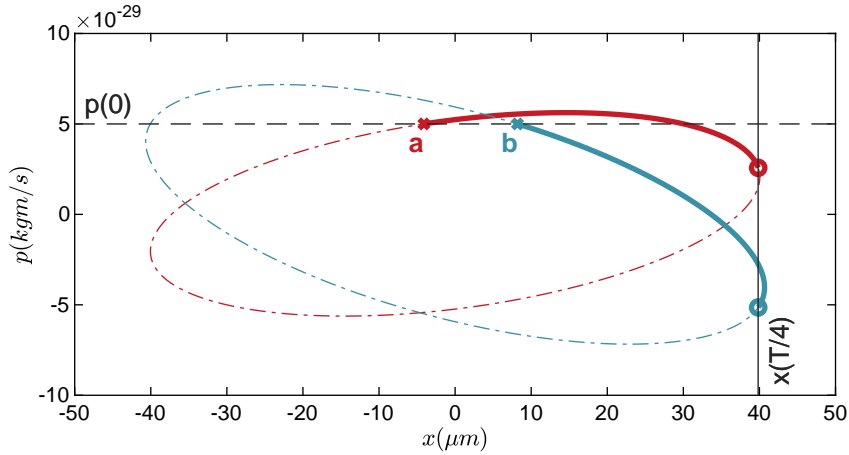


**Figure 4.1: A single phase space rotation.** The phase space trajectory for 2 particles a and b with the same mass and initial momentum, but different initial positions. The red (blue) curves show the phase space trajectory for particle a (b). The dashed line marks the entire phase space evolution, the full curve shows the phase space trajectory completed up to  $t = T/4$ , mapping the initial momenta onto positions and vice-versa.

To understand the principles of matterwave magnification, it is instructive to first consider the motion of a single, classical, particle of mass  $m_a$ , with initial ( $t = 0$ ) position  $x(0)$  and momentum  $p(0)$  in a one-dimensional harmonic oscillator potential,  $U(x) = \frac{1}{2}m_a\omega^2x^2$ , with harmonic oscillator frequency  $\omega$ . In classical mechanics, the Hamiltonian describing this system is given by

$$H = \frac{p^2}{2m_a} + \frac{m_a\omega^2x^2}{2}. \quad (4.1)$$

We obtain the phase space trajectory by solving Hamilton's equations  $\dot{x} = p/m_a$  and  $\dot{p} = -m_a\omega^2x$ , resulting in

$$p^2 \frac{1}{2m_a} + x^2 \frac{m_a\omega^2}{2} = \underbrace{\frac{p(0)^2}{2m_a} + \frac{m_a\omega^2x(0)^2}{2}}_{\text{const.}}, \quad (4.2)$$

spanning an ellipse in the  $x - p$  plane. Parametrizing this equation<sup>1</sup> gives

$$x(t) = x(0) \cos(\omega t) + p(0) \frac{1}{m_a\omega} \sin(\omega t) \quad (4.3)$$

$$p(t) = p(0) \cos(\omega t) - x(0)m_a\omega \sin(\omega t). \quad (4.4)$$

Thus, the position of the particle at  $t = T/4 = \frac{1}{4}\frac{2\pi}{\omega}$  is directly proportional to its initial momenta and vice versa with a scaling factor given by the mass and the harmonic oscillator frequency. This framework can easily be extended to higher dimensions, as the equations of motion are separable for a single particle in a harmonic oscillator potential.

The phase space trajectories of two particles (a and b) of equal mass with the same initial momenta  $p_a(0) = p_b(0) = p(0)$  but different initial positions  $x_a(0) \neq x_b(0)$  in the same harmonic

<sup>1</sup>or simply solving the problem using Newtonian mechanics

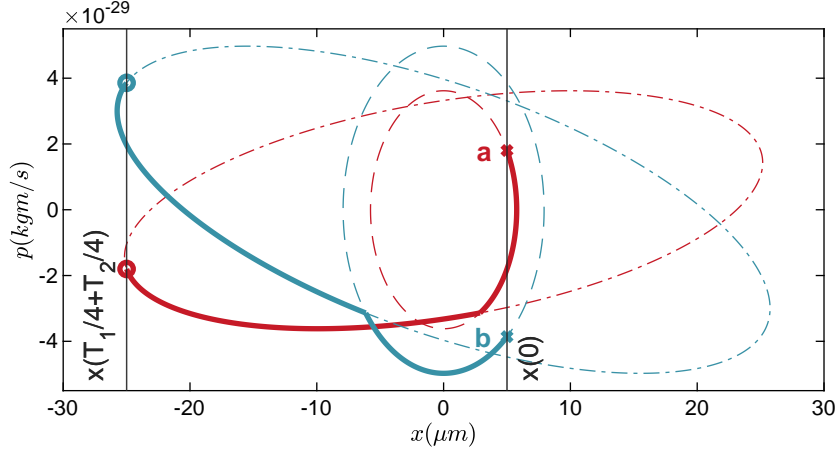


**Figure 4.2: Combining two phase space rotations.** Phase space trajectories for particles a (red) and b (blue). The particles first propagate through a harmonic oscillator with frequency  $\omega_1$  - marked by the dashed line. At time  $t = T_1/4$ , the phase space trajectory is set by a harmonic oscillator with frequency  $\omega_2 < \omega_1$ , shown by the dashed-dotted line. The solid line marks the combined phase space trajectories, i.e. two subsequent evolutions for a quarter time period, magnifying the initial position  $x(T_1/4 + T_2/4) = -\omega_2/\omega_1 x(0)$

oscillator potential are illustrated in Fig. 4.1. Owing to the different starting conditions, they follow different trajectories. At  $t = T/4$ , the particles have completed a scaled  $\pi/2$  Rotation in phase space, i.e. the final position is set by their initial momentum. Extending our considerations to an ensemble of particles with an initial momentum distribution  $\phi(p, t = 0)$  and real space distribution  $f(x, t = 0)$ , we obtain a scaled Fourier transform of these distributions at  $t = T/4$ . This however only holds when there are no interactions between the particles during the evolution in the harmonic potential.

We can achieve a magnification of the initial position by combining two subsequent  $T/4$  evolutions in harmonic potentials with different frequencies  $\omega_1 > \omega_2$ , where the index denotes the temporal sequence of potentials. The phase space coordinates after two subsequent  $T/4$  evolutions are

$$\begin{bmatrix} x(T_1/4 + T_2/4) \\ p(T_1/4 + T_2/4) \end{bmatrix} = \begin{bmatrix} -\omega_1/\omega_2 & 0 \\ 0 & -\omega_2/\omega_1 \end{bmatrix} \begin{bmatrix} x(0) \\ p(0) \end{bmatrix}, \quad (4.5)$$

The magnification factor  $M$  is determined by the magnification of the initial position

$$x(T_1/4 + T_2/4) = -x(0) \frac{\omega_1}{\omega_2} \underset{M}{}. \quad (4.6)$$

The phase space trajectories are illustrated in Fig. 4.2 for two identical particles (denoted as a and b) with the same initial position  $x_a(0) = x_b(0) = x(0)$ , but different initial momenta  $p_a(0) \neq p_b(0)$ . Each particle first follows the phase space trajectory set by the first harmonic potential. After a quarter time period the initial momenta are mapped onto positions and vice versa - a  $\pi/2$  rotation in phase space. Thereafter, the phase space trajectory is set by the second harmonic oscillator potential. Even though the two particles follow completely different phase space trajectories, they arrive at the same position  $x(T_1/4 + T_2/4) = -M \cdot x(0)$  after evolving for a quarter time period in the second harmonic potential. Again extending our considerations

to an ensemble of particles, we can see that a magnification of the initial position distribution is achieved by combining two Fourier transforms with different scaling factors.

### 4.1.1 Analogy to optics

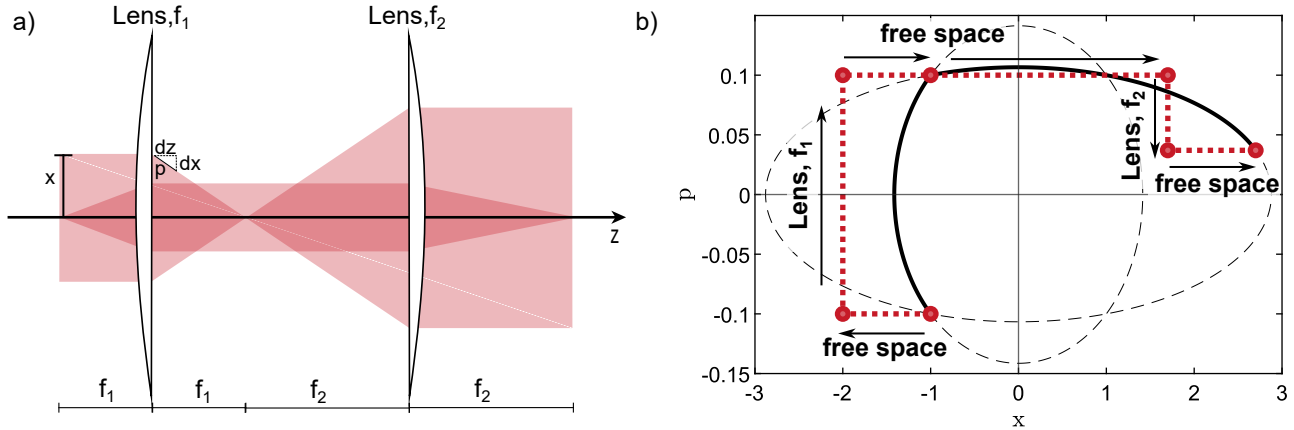


**Figure 4.3: Beam expander.** a) Conceptual sketch of a beam expander in 4f-configuration comprised of two thin lenses with focal lengths  $f_1$  and  $f_2$ , placed in a distance  $f_1 + f_2$ . b) Comparing the phase space trajectories of the 4f setup (red) with that in a harmonic oscillator potential (black).

The magnification of the initial position distribution by two scaled Fourier transforms is strongly reminiscent of an optical beam expander in the 4f imaging setup. This setup consists of two lenses with focal lengths  $f_1$  and  $f_2$ , placed in a distance  $d = f_1 + f_2$ , as sketched in Fig. 4.3a). The object plane is placed in a distance  $f_1$  of the first lens. The first lens performs a Fourier transform of the input field, with the spatial frequency coordinates scaled by the focal length  $f_1$ . The second lens performs another Fourier transform, mapping the Fourier components back to the spatial domain. In the image plane, placed in a distance  $f_2$  of the second lens, the final image is magnified by a factor  $M = -f_2/f_1$ .

However, the differences between the two systems can be seen by employing phase-space optics. Here each optical ray is equivalent to a single point in optical phase space, with coordinates corresponding to the distance  $x$  from the optical axis and the angle to the optical axis, referred to as the optical momentum  $p$ . Within the paraxial approximation, the transfer matrix formalism can be used to compute the phase space trajectories [53]. The propagation in free space is equivalent to a shearing along  $x$ -direction (transforming angle to position). A thin lens causes a shearing along  $p$ , as it changes the angle in dependence on the distance from the optical axis. The comparison of the phase space trajectories of a single optical ray in an optical beam expander and the phase space trajectory in a harmonic oscillator potential is sketched in Fig. 4.3b). While both systems map the initial point to the same final point in phase space the paths taken differ significantly. A propagation in a harmonic oscillator potential results in a smooth rotation through phase space. In the optical beam expander, the scaled rotations in phase space are each decomposed into three shearing operations.<sup>2</sup> Smooth rotations through optical phase space can be realized by utilizing gradient-index lenses.

<sup>2</sup>The decomposition of an arbitrary rotation into three shears was commonly used as a fast method to rotate bitmaps in the early days of computer graphics [54].

### 4.1.2 Quantum mechanical picture

Following a similar derivation as in the classical case for the quantum mechanical system, we can write the time evolution of the single particle operators in a one-dimensional harmonic oscillator potential as

$$\begin{bmatrix} \hat{x}(t) \\ \hat{p}(t) \end{bmatrix} = \begin{bmatrix} \cos \omega t & \frac{1}{m_a \omega} \sin \omega t \\ -m_a \omega \sin \omega t & \cos \omega t \end{bmatrix} \begin{bmatrix} \hat{x}(0) \\ \hat{p}(0) \end{bmatrix}. \quad (4.7)$$

in the Heisenberg picture. Due to the separability of the equations of motions along the different directions, the extension to a higher dimensional harmonic oscillator potential is trivial. Analogously to the classical case, letting the wave function evolve for a quarter time period is equivalent to a scaled Fourier transform. This allows us to map momentum onto real space by a single  $T/4$  evolution in a harmonic potential. Additionally, we can also magnify the initial wave function by combining two subsequent phase space rotations in two harmonic potentials. It is important to note that this mapping only holds for multiple particles when they are non-interacting during the expansion. A more detailed derivation of the quantum mechanical picture can be found in [55].

It is interesting to consider the momentum and position uncertainty after two  $T/4$  evolutions. For a system with an initial momentum (position) uncertainty  $\delta_p(0) = \sqrt{\langle \hat{p}(0)^2 \rangle}$  ( $\delta_x(0) = \sqrt{\langle \hat{x}(0)^2 \rangle}$ ), the uncertainty after two  $T/4$  evolutions is given by

$$\begin{aligned} \delta_x(T_1/4 + T_2/4) &= \delta_x(0) \frac{\omega_1}{\omega_2} \\ \delta_p(T_1/4 + T_2/4) &= \delta_p(0) \frac{\omega_2}{\omega_1}. \end{aligned} \quad (4.8)$$

It is evident (also following Liouville's theorem) that  $\delta_x(T_1/4 + T_2/4)\delta_p(T_1/4 + T_2/4) = \delta_x(0)\delta_p(0)$ . Assuming that uncertainty in real and momentum space is initially equivalent in natural units of the harmonic oscillator with frequency  $\omega_2$ , i.e.  $\delta_x(0)/l_{\text{HO}} = \delta_p(0)/p_{\text{HO}}$ , allows us to verify that  $\delta_x(T_1/4 + T_2/4)/l_{\text{HO}} > \delta_p(T_1/4 + T_2/4)/p_{\text{HO}}$ . Consequently, the system is in a squeezed state after matterwave magnification.

## 4.2 Experimental implementation

We can now use these concepts to implement two different matterwave manipulation protocols in our experiment. A single phase space rotation allows us to access momentum space observables. Combining two phase space rotations in potentials with different trap frequencies results in a magnification of the initial wave function in real space.

The phase space rotations discussed in Section 4.1 are however only valid for harmonic potentials. In reality, no potential is ever truly harmonic at all length scales. Experimentally, we can create potentials that can be approximated by a harmonic potential in a limited region around the trap center. This can be achieved utilizing either magnetic traps (as demonstrated in [51]) or optical dipole traps. When the particles probe the anharmonic region during the phase space evolution, the final (measured) position is dependent on both the initial momentum and

position. As a consequence, the clean mapping breaks down, giving rise to *Matterwave aberrations*. In the following I will discuss the experimental implementation, design considerations and limitations for achieving both momentum and real space resolution.

### 4.2.1 Interaction switch-off

The ability to switch off the interactions between the atoms on a timescale faster than any other timescale of the system is essential for all matterwave manipulation techniques. This is due to the fact that the mapping in Eq. (4.7) only holds for multiple atoms if they are non-interacting [55]. Such an interaction switch off can be performed by ramping the magnetic offset field to the zero crossing of the Feshbach resonance. However, due to the broad Feshbach resonance of  ${}^6\text{Li}$ , the zero-crossing (located at 568 G for the  $|1\rangle - |3\rangle$  mixture) is separated by  $\Delta \approx 200$  G from the offset fields typically used in the experiment (see also Sec. 2.3.4). The maximum ramp speed of our Feshbach coils is  $dB/dt \lesssim 1 \text{ G } \mu\text{s}^{-1}$ . Switching off the interactions in this manner would take around 200  $\mu\text{s}$ . This timescale is comparable to the timescale set by the radial trap frequency of the 2D-OT.

Instead, we switch off the interactions by performing a spin flip from hyperfine state  $|3\rangle$  to  $|4\rangle$ . There is no Feshbach resonance for the resulting  $|1\rangle - |4\rangle$  mixture. Consequently, the scattering length is set by the singlet scattering length  $a_s/a_0 = 47(3)$  [56]. We realize this spin flip by a two-photon Raman transition, experimentally implemented using two co-propagating laser beams. The first laser is locked between the  $D1$  and  $D2$  line, the second laser is phase-locked to the first laser, with a frequency offset equivalent to the energy difference between states  $|3\rangle$  and  $|4\rangle$  at a given magnetic field (typically  $\omega/2\pi \approx 2$  GHz). We measure a Rabi frequency of  $\Omega/2\pi = 1.613$  MHz, allowing us to transfer  $|3\rangle$  to  $|4\rangle$  in  $\tau = 310$  ns, a timescale much faster than any other timescale of the system. Hence, the transfer can be considered as instantaneous. More information on the Raman setup can be found in [57].

### 4.2.2 Momentum space

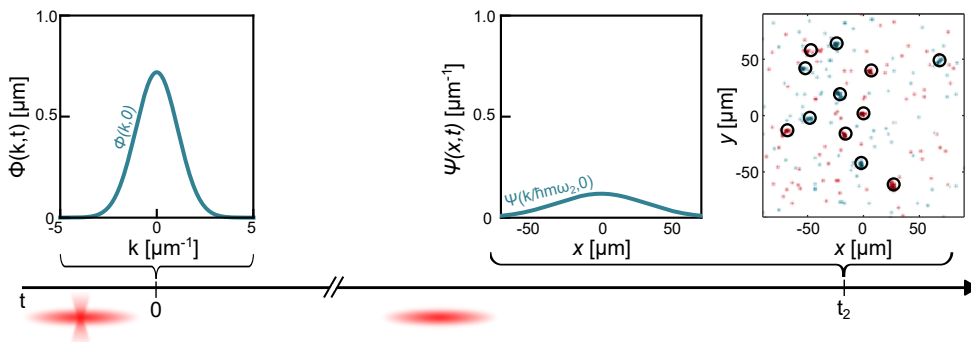


**Figure 4.4: Conceptual illustration of Matterwave mapping of momentum space onto real space.** The initial momentum space wave function is mapped onto real space by a long, non-interacting expansion time  $t_2$  in the weak radial potential of the standing wave optical dipole trap. We image the atom positions after this long expansion time, allowing us to infer the initial momentum. The sequence of traps is illustrated below the timeline.

There are two experimental approaches for mapping momentum space onto real space. In free space, a long, ballistic (i.e. non-interacting), time of flight (TOF) maps momenta onto

positions. This is only fully independent of the initial position spread for an infinite expansion time. However, for large enough time of flights, the influence of the initial position on the final position becomes negligible, and momentum resolution can be obtained. An alternative approach is performing an (again non-interacting) evolution for a quarter time period in a harmonic potential [55, 58, 59], as discussed above. This allows for a clean mapping between real and momentum space. In our experiment, we use a combination of the two techniques.

The matterwave mapping from momentum to real space is illustrated in Fig. 4.4. We realize the potential for the phase space rotation by a combination of a magnetic trap (set by the curvature of the magnetic offset field) ( $\omega_{r,B}/2\pi = \pm 10.9(3)$  Hz) and the radial curvature of the standing wave optical dipole trap ( $\omega_{r,SWT}/2\pi = 16.9(1)$  Hz). The combined trap frequency is given by  $\omega_2 = \sqrt{\omega_{r,SWT}^2 \pm \omega_{r,B}^2}$ , where the sign of  $\omega_{r,B}$  depends on the hyperfine state that the atoms evolve in (negative for low field seekers, positive for high field seekers). While our system is initially prepared in the high field seeking hyperfine states of  ${}^6\text{Li}$  ( $|1\rangle$  and  $|3\rangle$  to be specific), the interaction switch off prior to the phase space evolution is realized by a spin flip from  $|3\rangle$  to the low field seeking state  $|4\rangle$  (see Sec. 2.2 and Sec. 4.2.1). Therefore, the effective trap frequency is different for the two spin states ( $\omega_2/2\pi = 20.1$  Hz (12.9 Hz) for the high(low)-field seeking states), leading to different phase space trajectories and different  $T/4$  times. When the spatial extent  $\delta_x(t) = \sqrt{\langle \hat{x}(t)^2 \rangle}$  after a finite expansion time  $t$  is significantly larger than the initial spatial extent  $\delta_x(0)$ , we can neglect the influence of  $\delta_x(0)$  on  $\delta_x(t)$ . This allows for a mapping from momentum onto real space also for  $t \neq T/4$ .

The assumption  $\delta_x(t=0) = 0$ , leads to an error when mapping the measured position back to an initial momentum. In our system, the initial extent of the wave function is on the order of the harmonic oscillator length of the 2D-OT,  $l_{\text{HO},r} = \sqrt{\hbar/m_a\omega_r}$ . For the propagation in a harmonic oscillator potential, this error is given by

$$\Delta p_0/p_{\text{HO}} \approx \frac{\omega_2}{\omega_r} \cot(\omega_2 t_2) \quad (4.9)$$

where  $p_{\text{HO}} = \sqrt{\hbar m_a \omega_r}$  is the harmonic oscillator momentum. For a typical expansion time,  $t_2 = 12$  ms,  $\Delta p_0 \approx 1 \times 10^{-3} p_{\text{HO}}$  for the high field seekers and  $\Delta p_0 \approx 8 \times 10^{-3} p_{\text{HO}}$  for the low field seekers. This error is significantly smaller than that caused by our finite imaging resolution. The RMS width of a single atom, imaged using our free space fluorescence scheme is  $\delta_{\text{psf}} = 4.9(3)$   $\mu\text{m}$  (for more details see Sec. 3.3). This causes an uncertainty on the initial momentum given by

$$\Delta p_{\text{psf}} = \delta_{\text{psf}} \frac{m_a \omega_2}{\sin(\omega_2 t_2)}. \quad (4.10)$$

For  $t_2 = 12$  ms the uncertainty on the initial momentum due to the imaging resolution is  $\Delta p_{\text{psf}} \approx 6 \times 10^{-2} p_{\text{HO}}$ .

In the limit where the initial position spread can be neglected, we can find a direct mapping from  $\hat{p}(0)$  to  $\hat{x}(t)$ , even for potentials exhibiting slight deviations from perfect harmonicity. To achieve this, we create a look-up table mapping the measured final position onto the corresponding initial momentum, by numerically solving the trajectory in the combined potential of magnetic

trap (Harmonic) and the SWT (Gaussian). The combined potential is given by

$$U_{\text{tof}} = \frac{m_a (w_r \omega_{\text{SWT},r})^2}{4} \left( 1 - \exp\left(\frac{-2x^2}{w_r^2}\right) \right) \pm \left( \frac{1}{2} (x\omega_{\text{B},r})^2 m_a \right). \quad (4.11)$$

Here  $m_a$  is the mass of the atom,  $w_r = 600 \mu\text{m}$  is the waist of the SWT,  $\omega_{\text{SWT},r}$  and  $\omega_{\text{B},r}$  are the trap frequencies of the SWT and the magnetic trap, respectively. The sign of the second term is determined by whether the atoms are in a high (+) or low (-) field-seeking state. Using

$$F = -\frac{\partial U}{\partial x} = m_a \ddot{x} \quad (4.12)$$

and substituting  $\tilde{x} = x/w_r$  and  $\tilde{t} = t \cdot 2\pi/T_{\text{opt}}$  where  $T_{\text{opt}} = 2\pi/\omega_{\text{SWT},r}$ , we can simplify the differential equation to

$$\ddot{\tilde{x}} = -\tilde{x}(\tilde{t}) \exp(-2\tilde{x}^2(\tilde{t})) \pm (\omega_{\text{B},r}/\omega_{\text{SWT},r})^2. \quad (4.13)$$

We create a separate look up tables for the high and low field seeking states by solving the differential equation for different initial momenta.

### 4.2.3 Real space

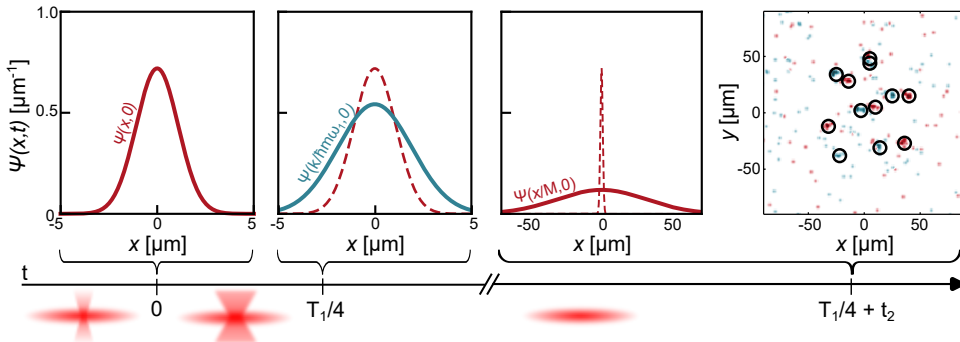


**Figure 4.5: Conceptual illustration of the matterwave magnification protocol.** The initial, micron-sized wave function is released from the 2D-OT and magnified by two subsequent evolutions in harmonic potentials. The first  $T/4$  evolution – performed in the magnifier trap (MT) – is equivalent to a scaled Fourier transform of the initial wave function. A second, expansion time  $t_2$  in the weak radial potential of the SWT is equivalent to a second Fourier transform of the wave function. The initial real space wave function is magnified by a factor  $M$ , given by the ratio of the two trap frequencies. This magnification allows us to obtain a snapshot of the wave function with single particle and spin resolution. The sequence of traps is illustrated below the timeline. The initial wave function (dashed curve) is shown as a reference in each time step. Figure adapted from [SB2].

To achieve a magnification of the initial matterwave we perform two subsequent evolutions: a  $T/4$  evolution in a potential with large trap frequency and a second evolution in a weak potential. For the first evolution, we implemented a new potential (magnifier trap (MT)) – tailored for accurate magnification of the initial wave function. The second evolution is performed in the weak radial potential created by the SWT and the magnetic trap, that is also

utilized to map the initial momenta onto real space, as described in Sec. 4.2.2. The evolution of the wave function and the sequence of traps is illustrated in Fig. 4.5. The following section aims to serve as an instruction for the experimental implementation of a matterwave magnifier.

### Design considerations for the first potential

Accurate magnification of the initial matterwave requires on the one hand a magnification large enough that the smallest structure sizes of interest are resolvable by our imaging scheme after magnification. On the other hand, the potential used for the first  $T/4$  evolution has to be tailored such that the matterwave remains in the harmonic region of the trap during the entire evolution. These two considerations allow us to obtain an estimate of the required trap parameters.

The smallest structure size of interest in the 2D limit is – for a fermionic system – set by the harmonic oscillator length in  $z$  direction,  $l_{\text{HO},z} = \sqrt{\hbar/m_a\omega_z}$ . In our system,  $\omega_z/2\pi = 7432(3)$  Hz, setting  $l_{\text{HO},z} = 480$  nm (see also Chapter 3). Thus, to be able to resolve the length scales of interest, we need to magnify the initial matterwave such that

$$M \cdot l_{\text{HO},z} \gg \delta_{\text{psf}}. \quad (4.14)$$

Here  $\delta_{\text{psf}} = 4.9(3)$   $\mu\text{m}$  is the RMS width of a single atom, imaged using our free space fluorescence scheme (for more details see Sec. 3.3). Consequently, we require a magnification factor  $M = \omega_1/\omega_2 \gg 9$ . The second phase space rotation is again performed in the potential detailed in Sec. 4.2.2, with a trap frequency of  $\omega_2/2\pi = 20.2(3)$  Hz for the low-field seeking states. Because the radial trap frequency is lower for the high field states – leading to a larger magnification – we consider the low-field seekers for the following design considerations. For the first rotation, we require a trap frequency  $\omega_1/2\pi \gg 180$  Hz. As the maximum achievable magnetic trap frequency in our system is only  $\omega_B/2\pi \approx 20$  Hz, we realize the first phase space rotation in an optical potential created by a focused laser beam.

The potential created by a focused Gaussian laser beam with frequency  $\omega$  is given by

$$U_G(r) = \tilde{\alpha}I(r) = \tilde{\alpha} \frac{2P}{\pi w^2} \exp\left(\frac{-2r^2}{w^2}\right), \quad (4.15)$$

where  $P$  is the power of the laser beam, and  $w$  is the beam waist in the atom plane. The factor  $\tilde{\alpha}$  is given by

$$\tilde{\alpha} = \frac{3\pi c^2}{2\hbar\omega_0^3} \frac{\Gamma}{\omega - \omega_0}, \quad (4.16)$$

where  $\omega_0$  is the frequency of the optical transition,  $\omega$  is the optical frequency of the laser beam and  $\Gamma$  is the natural linewidth (see also Sec. 2.4). Considering the series expansion of the Gaussian potential

$$U_G(r) = \frac{2P\tilde{\alpha}}{\pi w^2} \left(1 - 2\frac{r^2}{w^2} + 2\frac{r^4}{w^4} - \frac{4}{3}\frac{r^6}{w^6} + \mathcal{O}(r^8)\right) \quad (4.17)$$

it can be approximated as a harmonic potential

$$U_{\text{harm}}(r) = -\frac{1}{2}\omega_1^2 m_a r^2, \quad (4.18)$$

for  $r \ll w$ . Consequently, to ensure accurate magnification, we have to ensure that the spatial extent of the wave function  $\delta_x(t) = \sqrt{\langle \hat{x}(t)^2 \rangle}$  remains much smaller than the waist of the first potential. The waist directly sets the *field-of-view (FOV)* of the matterwave magnifier, as  $\delta_x(0) \ll w$ . The angular trap frequency is

$$\omega_1 = \sqrt{\frac{8P\tilde{\alpha}}{\pi w^4 m_a}}. \quad (4.19)$$

The maximum extent of the wave function during the evolution is given by

$$\max(\delta_x(t)) = \sqrt{\delta_x(0)^2 + \left(\frac{1}{m_a \omega_1} \delta_p(0)\right)^2}, \quad (4.20)$$

assuming a Gaussian initial state with  $\langle \hat{x}\hat{p} \rangle = \langle \hat{p}\hat{x} \rangle = 0$ . Here,  $\delta_p(t) = \sqrt{\langle \hat{p}(t)^2 \rangle}$  is the extent of the wave function in momentum space. Therefore, accurate magnification is ensured when both the initial spatial extent  $\delta_x(0)$  and the extent at  $t = T/4$ ,

$$\delta_x(T/4) = 1/m_a \omega \delta_p(0), \quad (4.21)$$

are much smaller than the waist.

A lower limit for the initial momentum distribution is – following Heisenberg’s uncertainty relation – set by the smallest structure sizes in the initial system  $\sigma_x$ , which results in  $\delta_p(0) \geq \hbar/2\sigma_x$ . The *diffraction limit* is then given by

$$\sigma_x \gg \frac{\sqrt{\pi}\hbar w}{4\sqrt{2|\tilde{\alpha}|Pm_a}}. \quad (4.22)$$

Following these considerations, we can formulate a list of requirements for a matterwave magnifier optimized for our system. According to Eq. (4.14), we need a trap frequency of  $\omega_1/2\pi \gg 180$  Hz, ensuring that the smallest structure sizes are resolvable by our fluorescence imaging scheme after magnification. The required FOV – set by the beam waist – is dictated by the largest system we want to explore. The system size can be approximated by the Thomas Fermi radius  $r_F = \sqrt{2E_F/m_a\omega_r^2}$ , where  $E_F$  is the Fermi energy and  $\omega_r$  is the frequency of the 2D-OT in radial direction. The largest system explored in the scope of this thesis is a system with  $E_F = 6\hbar\omega_r$  (i.e. 21 atoms per spin state) at a radial trap frequency of  $\omega_r/2\pi = 655(2)$  Hz, resulting in  $r_F \approx 5.5 \mu\text{m}$ . Consequently, we require a waist radius  $w \gg 5.5 \mu\text{m}$  to ensure that the system is initially in the FOV. This excludes the possibility of using the 2D-OT for the magnification, as its radial waist is only  $\approx 5 \mu\text{m}$ .

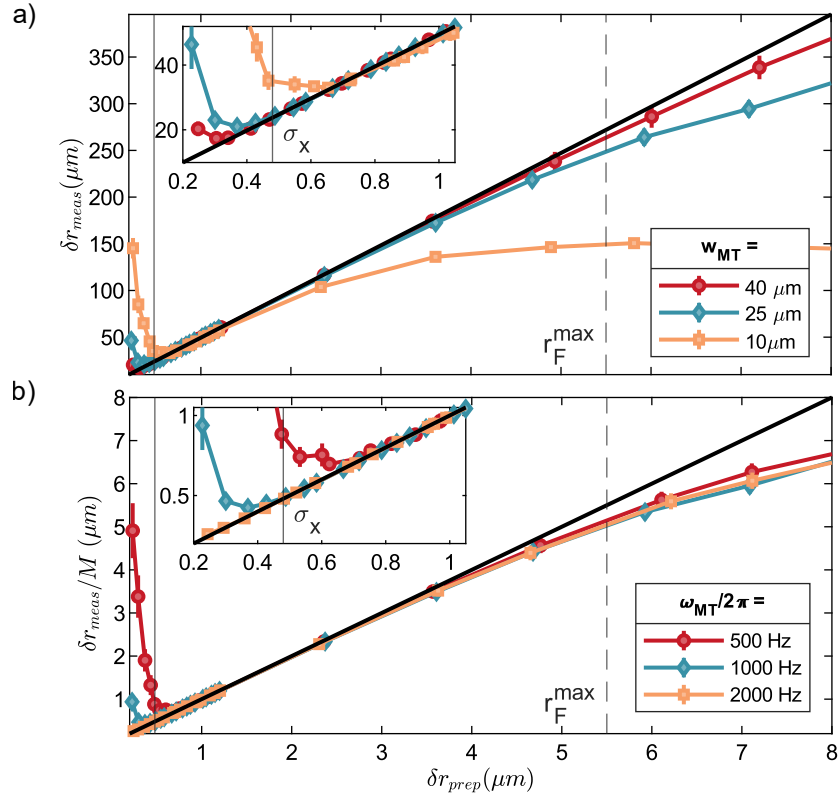


**Figure 4.6: Simulation of the matterwave magnifier for different waists and frequencies.** We simulate the matterwave magnification protocol by propagating the starting conditions set by the width of the real space distribution  $\delta r_{\text{prep}}$  and Heisenberg's uncertainty principle and plot the final RMS width  $\delta r_{\text{meas}}$ . We simulate the expansion for different waists ( $w_{\text{MT}}$ ) a) and frequencies ( $\omega_{\text{MT}}$ ) b) of the MT. Note that we divide the final width by the magnification factor in b), to compare the performance at different magnifications. The largest system size implemented in our experiment  $r_{\text{F}}^{\text{max}}$  and smallest structure sizes  $\sigma_x$ , set the requirement for the field-of-view and the resolution, respectively. The black diagonal line shows the expectation for an ideal matterwave magnifier.

### Simulating the matterwave magnification

We perform a simulation of the matterwave magnification protocol, to gain more accurate estimate of the required beam parameters. We approximate the magnifier trap with a Gaussian potential

$$U_{\text{MT}} = \frac{m_a (w_{\text{MT}} \omega_1)^2}{4} \left( 1 - \exp\left(\frac{-2x^2}{w_{\text{MT}}^2}\right) \right), \quad (4.23)$$

here  $m_a$  is the mass of the atom,  $w_{\text{MT}}$  and  $\omega_1$  are the waist and trap frequency of the MT, respectively.

Using

$$F = -\frac{\partial U}{\partial x} = m_a \ddot{x} \quad (4.24)$$

and substituting  $\bar{x} = x/w_{\text{MT}}$  and  $\bar{t} = t \cdot 2\pi/T_1$  where  $T_1 = 2\pi/\omega_1$ , gives the differential equation

$$\ddot{\bar{x}} = -\bar{x}(\bar{t}) \exp(-2\bar{x}^2(\bar{t})) \quad (4.25)$$

describing the expansion in the MT. We can simulate the evolution in the MT by numerically

solving Eq. (4.25) for different initial conditions. We then use the numerically calculated values for  $x(T/4)$  and  $p(T/4)$  as input parameters for Eq. (4.13), describing the evolution in the second potential.

To obtain the FOV and the resolution from the simulation, we employ a semi-classical approach. The initial position distribution is set by a Gaussian distribution with RMS width  $\delta r_{\text{prep}}$ . The corresponding momentum width is obtained by assuming a Heisenberg limited system. To obtain the magnified widths  $\delta r_{\text{meas}}$  in dependence of the initial width of the system,  $\delta r_{\text{prep}}$  we sample the real and momentum space distributions 1000 times for each  $\delta r_{\text{prep}}$ . We propagate the initial parameters through both differential equations and calculate the RMS of the final positions to obtain  $\delta r_{\text{meas}}$ . The results of this simulation for different parameters of the MT are shown in Fig. 4.6. In an aberration free system, i.e. for a harmonic potential, the measured widths follow the linear relation

$$\delta r_{\text{meas}} = M \cdot \delta r_{\text{prep}}, \quad \forall \delta r_{\text{prep}}. \quad (4.26)$$

However, when the matterwave probes the anharmonic regions of the MT, we observe a deviation from this relation. This occurs for very small initial widths, i.e. high initial momenta, and for very large initial widths. The FOV is set by the deviation from the linear relation at large  $\delta r_{\text{prep}}$ , the resolution by the deviation at small  $\delta r_{\text{prep}}$ .

While changing the waist of the magnification trap (Fig. 4.6a) changes both the FOV and the resolution, changing the trap frequency at constant waist only significantly alters the resolution (Fig. 4.6b). However, as long as the FOV is large enough, choosing a larger trap frequency  $\omega \propto \sqrt{P}w^{-2}$  over a larger waist reduces the required laser power. From the simulations we can see that a magnifier trap with frequency  $\omega_{\text{MT}}/2\pi = 1000$  Hz and waist  $w_{\text{MT}} = 25 \mu\text{m}$  provides accurate magnification from the smallest structures  $\sigma_x$  up to the largest system sizes  $r_{\text{F}}^{\text{max}}$ .

### Implementing the Matterwave magnifier

The experimental setup used to create the magnifier trap is sketched in Fig. 4.7. The potential for the first step in the magnification is created by a focused laser beam with a wavelength of  $\lambda = 1064$  nm. We focus the beam onto the atoms using a lens with a focal length  $f = 80$  mm, placed below the vacuum chamber. Note that great care has to be taken to align the lower lens on the optical axis of the microscope objective, such that the magnifier trap and the optical tweezer can be overlapped. Additionally, the alignment of the laser beam on the lens is crucial to ensure that the MT is radially symmetric, otherwise the matterwave magnification will suffer from an astigmatism. The waist in the atom plane is expected to be on the order of  $w_{\text{MT}} = 22 \mu\text{m}$ . With a laser power stabilized to  $P = 4$  W, we can achieve a trap frequency of  $\omega_1/2\pi = 1130(10)$  Hz. The second stage of the matterwave magnification is realized in the weak radial potential (described in Sec. 4.2.2), created by the weak optical trap provided by the SWT and the magnetic trap, with a trap frequency of  $\omega_2/2\pi = 20.1$  Hz (12.9 Hz) for the high(low)-field seeking states. Hence, we can achieve a maximum magnification factor of  $M = 56(1)$  for the high field seeking hyperfine states and  $M = 87(1)$  for the low-field seeking states.

We test the performance of the matterwave magnifier using a single atom in the ground state of

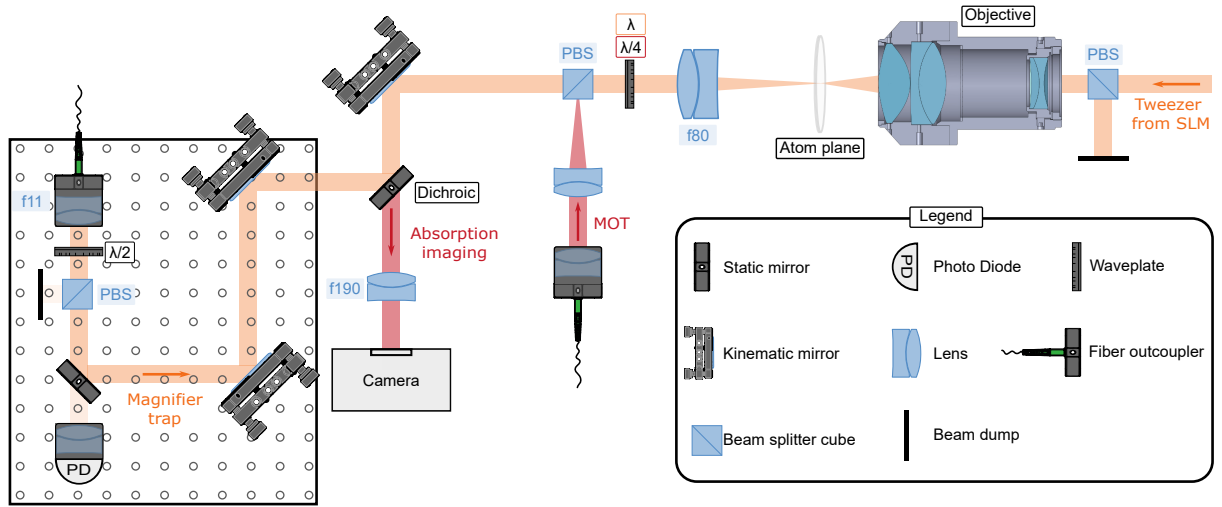


**Figure 4.7: Experimental setup for the implementation magnification trap.** A sketch of the optical setup used to create the magnifier trap. The collimated beam is focused onto the atomic plane with  $f = 80$  mm lens (CVI Laser Optics, LAI-80.0-25.0). After the optical chamber, the beam is reflected onto a beam dump by a polarizing beam splitter cube. This is done to protect the spatial light modulator.

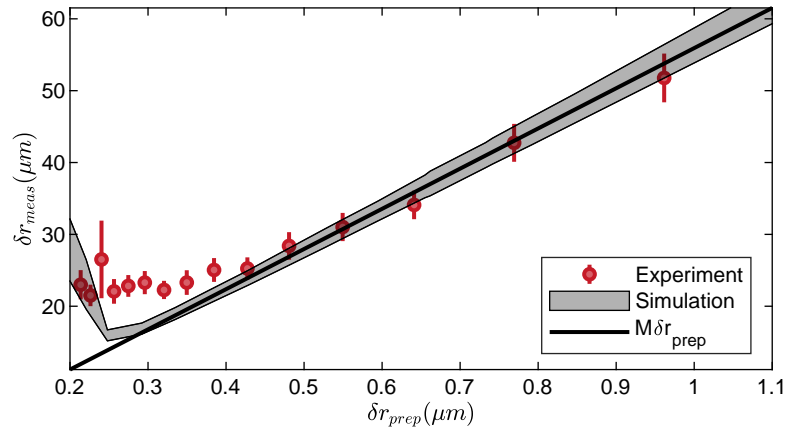


**Figure 4.8: Resolution of the Matterwave magnifier.** Measured  $\delta r_{\text{meas}}$  versus prepared width  $\delta r_{\text{prep}}$  for a system of a single  ${}^6\text{Li}$  atom in the ground state of the 2D-OT. We vary the prepared width by varying the radial trap frequency of the 2D-OT. The black line marks the ideal, aberration free matterwave magnifier. We deviate from this ideal case for  $\delta r_{\text{prep}} < 300$  nm. The gray band marks the result of the simulated propagation. All error bars represent the 95% confidence interval and were obtained using a bootstrapping technique. Figure taken from [SB2].

## 4.2. Experimental implementation

the 2D optical tweezer as a test target. Here, the momentum spread at a given position spread is Heisenberg limited, allowing us to compare our experimental results to the simulation discussed above. By varying the radial trap frequency of the 2D-OT, we vary the prepared width  $\delta r_{\text{prep}}$  of the system and determine the RMS width after magnification  $\delta r_{\text{meas}}$  from many experimental implementations of the same quantum state – see Fig. 4.8. For large  $\delta r_{\text{prep}}$ , the measured widths follow the expectation for an ideal matterwave magnification ( $\delta r_{\text{meas}} = M \cdot \delta r_{\text{prep}}$ ). We define the resolution of the matterwave magnifier as the point where  $\delta r_{\text{meas}} > \sqrt{2}M\delta r_{\text{prep}}$ , resulting in a resolution of  $\delta r_{\text{res}} = 300$  nm. The measured resolution is larger than that expected in the simulation. This discrepancy can be explained by the uncertainty on the exact shape of the MT in the atom plane.

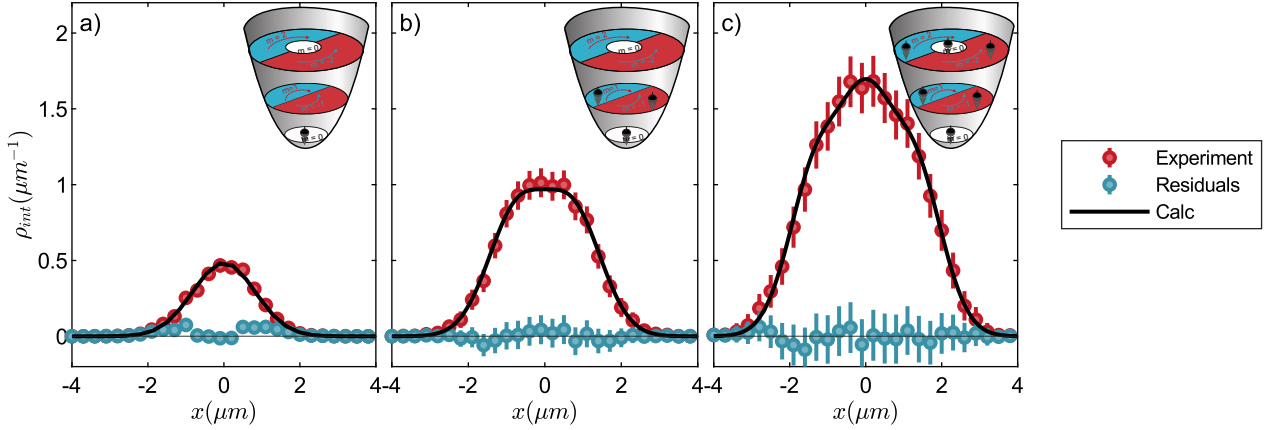


**Figure 4.9: Ground state densities.** Real space density (integrated along one spatial direction) of 1 a) , 3 b) and 6 c)  ${}^6\text{Li}$  atoms in the ground state of a harmonic oscillator potential. The red dots show the experimental measurement, the black line represents the calculated density. The blue dots show the residuals, i.e. the difference of the experimental and theoretical result. The inset shows the occupation of the harmonic oscillator levels. The error bars represent the standard errors of the mean.

The matterwave magnifier can also be used to magnify the wave function of multiple atoms. We verify this using  $N$  spin-down atoms, prepared in the ground state of the 2D-OT (with radial trap frequency  $\omega_r/2\pi = 1420(2)$  Hz) as a test target. Due to Pauli’s exclusion principle, the atoms occupy the harmonic oscillator shells as sketched in the insets of Fig. 4.9. Given the radial trap frequency, the ground state density can be calculated analytically from the 2D harmonic oscillator wave functions. Experimentally, we determine the density by 1000 repeated measurements of the atom positions after magnification. The comparison of the measured and calculated density – both integrated over one spatial direction – are shown in Fig. 4.9, for  $N = 1, 3$  and 6 atoms (a), b), c), respectively). The residuals show no significant deviation of the experimental results from the analytic calculations.

Additionally, we benchmark our ability to accurately magnify the wave function of interacting atoms. We prepare one spin up and one spin down atom in the ground state of the 2D-OT. The magnetic Feshbach resonance allows us to tune the interactions between atoms in different spin states and thus the two-body binding energy  $E_B$  (for more details see Sec. 2.3.4). At a given radial and axial trap frequency, relative wave function of two interacting atoms in the ground state of a radially symmetric harmonic oscillator can be calculated analytically, following the derivation of Idziaszek et al. [60].

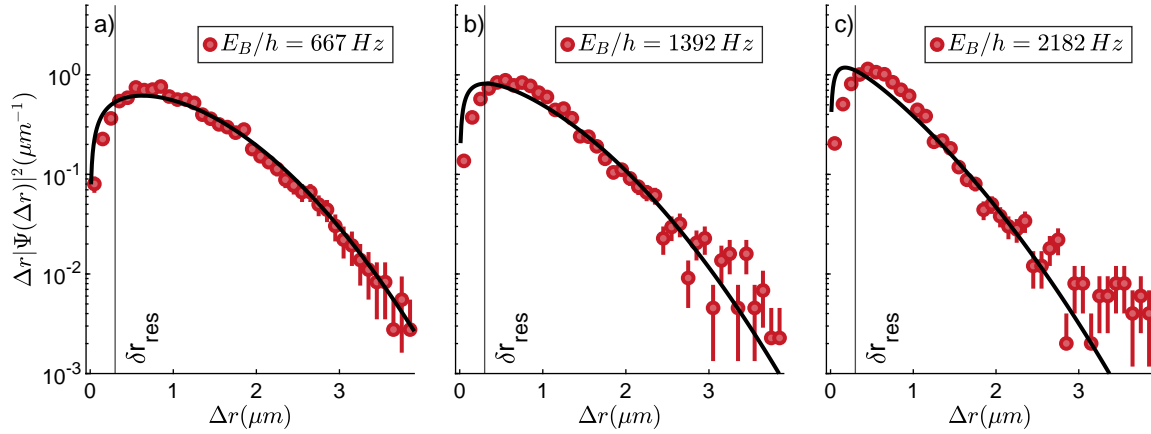


**Figure 4.10: Squared relative wave functions of two interacting atoms.** Normalized occurrence of distances  $\Delta r$ , measured in a system of two  ${}^6\text{Li}$  atoms with binding energy  $E_B$  in the ground state of a quasi 2D harmonic oscillator potential. We compare the experimental results (red data-points) to the analytically calculated squared relative wave function (black line). The error bars represent the standard errors of the mean.

The comparison of analytically calculated and measured squared relative wave function  $|\psi(\Delta r)|^2$  for different  $E_B$  are shown in Fig. 4.10. For  $E_B/h \lesssim 1400$  Hz, we find good agreement between the measurements and the analytically calculated wave function. However, at larger binding energies we start to observe a deviation from the analytical calculation, that is not restricted to small relative distances  $\Delta r$ . Owing to matterwave aberrations, the magnified distance of two atoms with very small initial distances, i.e. very large relative momenta, is larger than the magnified distance expected for perfect matterwave magnifier. Hence, small initial separations are observed as larger separations.

Like in optical systems, this effect could be reduced by implementing a finite aperture, removing the parts of the wave function probing the anharmonic regions of the trap. This could be realized by a magnifier trap that is a confining potential for  $x < w$  and anti-confining for  $x > w$ . While such a potential is experimentally achievable using a beam shaping device such as a digital micro-mirror device or a Laguerre Gauss beam, it would come at the cost of losing atoms during the matterwave magnification.

### 4.3 Conclusion

In conclusion, we have demonstrated two techniques for matterwave manipulation based on evolutions in optical potentials. First, a single scaled Fourier transform of the initial matterwave maps momentum onto position space. Combined with our single atom and spin resolved imaging technique, this unlocks access to the initial momentum distribution. Second, a magnification of the initial wave function by a factor of  $\approx 56$  was achieved by two subsequent evolutions in optical potentials. We tailored the optical potentials for accurate magnification of all relevant length scales. This was verified by experimental measurements using quantum systems with known wave functions as test-targets. The magnification of the initial wave function unlocks access to observables in real space, which were initially obfuscated by the imaging resolution.



## 5 | Emergence of elliptic flow

Simple fluids are easier to drink than to understand.

---

A. C. NEWELL AND V. E. ZAKHAROV  
*Optical Turbulence, 1995*

Hydrodynamics is one of the most prominent frameworks in physics, describing phenomena spanning several orders of magnitudes in both length and energy scales. The remarkable versatility of hydrodynamics is evident in its ability to describe systems as diverse as galaxies [61], atomic nuclei [62] or the movement of planktonic microorganisms in the ocean [63]. One of the fundamental assumptions of hydrodynamics is that the exact microscopic properties can be disregarded [64]. Instead, the dynamics of the system are described by effective macroscopic quantities, such as velocity and pressure. Hydrodynamics then treats the system in terms of macroscopic fluid cells that are both much smaller than the system size and much larger than the interparticle spacing and the mean free path.

A hydrodynamic framework has also been successfully employed to model the expansion of the exotic state of matter created in high energy heavy-ion collisions: the quark-gluon plasma (QGP) [65–67]. Surprisingly, elliptic flow, a key signature of hydrodynamic behavior observed in the expansion of the QGP, has also been observed in the expansion of the medium produced in high energy proton-proton collisions with only few tens of final state hadrons [68]. Here, the separation of scales required for a hydrodynamic description is not present.

Motivated by these experimental observations, we explore the emergence of interaction-driven elliptic flow on the other end of the temperature scale. Compared to high-energy particle collisions, ultracold atom experiments offer a significantly higher degree of control over particle number, interaction strength and initial geometry. This enables us to explore the emergence of collectivity from the bottom up, in a controlled setting. In addition, we have access to observables that remain elusive in high energy physics, as we can observe the expansion of the system in real and momentum space, with time and single particle resolution.

*The experimental and theoretical results in this chapter are adapted from the publication*

*“Emergent interaction-driven elliptic flow of few fermionic atoms”*

S. Brandstetter\*, P. Lunt\*, C. Heintze, G. Giacalone, L. H. Heyen, M. Gałka,  
K. Subramanian, M. Holten, P. M. Preiss, S. Floerchinger, and S. Jochim,  
Nature Physics, 10.1038/s41567-024-02705-8 (2025) [SB3]

*and are presented with modifications and additions.*

## 5.1 Hydrodynamics in high energy physics

*This section aims to provide a concise overview on the small system size puzzle in the context of high energy physics, based on review articles [69, 70]. There, one can also find a more comprehensive overview on the subject.*

At the temperatures and densities found in today's universe quarks and gluons are bound into hadrons (e.g. protons and neutrons). However, in its early stages – from roughly 10 ps to 10  $\mu$ s after the big bang – the universe is thought to have taken the form of a quark-gluon plasma, an exotic state of matter, in which quarks and gluons are deconfined [65]. In more recent history, the QGP is created in high energy collisions of heavy ions. The temperatures of  $\approx 400$  MeV (equivalent to 5 TK) reached in these collisions are high enough to deconfine the quarks and gluons [71–74]. In the initial time after the collision, the system is strongly out of equilibrium. After a highly complex, yet to be understood evolution phase, commonly referred to as pre-hydrodynamization phase, the QGP expands, following the laws of relativistic hydrodynamics. It is interesting to note that the idea that the expansion follows the laws of hydrodynamics was already conjectured by Landau in 1956 [66]. During the expansion process the quark-gluon plasma cools, eventually crossing the transition temperature of 170 MeV (equivalent to 2 TK) [75]. Here, hadrons form out of the quarks and gluons. The resulting hadrons continue to expand. First, they scatter both inelastically and elastically, until the so-called chemical freeze out. Thereafter, they scatter elastically until their mean free path far exceeds the system size – the kinetic freeze out. Here, the redistribution of momenta ceases. These final momenta of the hadrons are then measured on the particle detectors.

Experimentally, hydrodynamic behavior is inferred from the angular distribution of the measured hadron momenta [67]. Typically, the collision region of two nuclei is not rotationally symmetric but elliptic or almond-shaped, as the collision is peripheral. The exact geometry is set by the impact parameter, which can be determined from the number of participating nucleons [67]. The anisotropic shape gives rise to anisotropic pressure gradient forces, resulting in an anisotropic distribution of final momenta. This behavior, commonly known as *elliptic flow*, is considered as a smoking gun of hydrodynamics.

Relativistic hydrodynamics has proven to accurately describe the expansion of matter created in the collisions of two heavy ions such as gold [72] or lead [76]. Surprisingly, the signatures of elliptic flow observed in these systems are also present in much smaller systems, produced for example in the collision of two protons [68]. These systems are expected to be too small to produce a quark-gluon plasma or to justify a hydrodynamic approach. Nonetheless, a hydrodynamic description has proven to successfully model the expansion of these small systems with only a few tens of final state particles. In addition, experiments with different initial system geometries (created in the collision of gold with either a proton, deuterium or  $^3\text{He}$ ) have shown that the final distribution of particles can be successfully linked to the initial geometry by relativistic hydrodynamics [77–80]. These observations have sparked interest in finding the number of final state particles for which this collective description breaks down. These attempts [81, 82] have however remained inconclusive, as other sources of correlations mask the weak signal attributed to collective flow.

## 5.2 Elliptic flow in a mesoscopic Fermi gas

Here, we study the emergence of interaction driven elliptic flow on the other end of the temperature scale. Elliptic flow has previously been observed in the expansion of interacting, ultracold quantum gases with large number of constituents [83–86]. In these systems, the characteristic inversion of the aspect ratio was observed by imaging the expanding cloud at different time steps during the expansion. We employ a similar approach to explore interaction driven elliptic flow in a system of few, fermionic  ${}^6\text{Li}$  atoms. Imaging the system in real and momentum space allows us to distinguish collective and single particle dynamics. In addition, our control over both interaction strength and atom number allows us to study the emergence of collectivity in a controlled setting.

### 5.2.1 Preparing an elliptic cloud

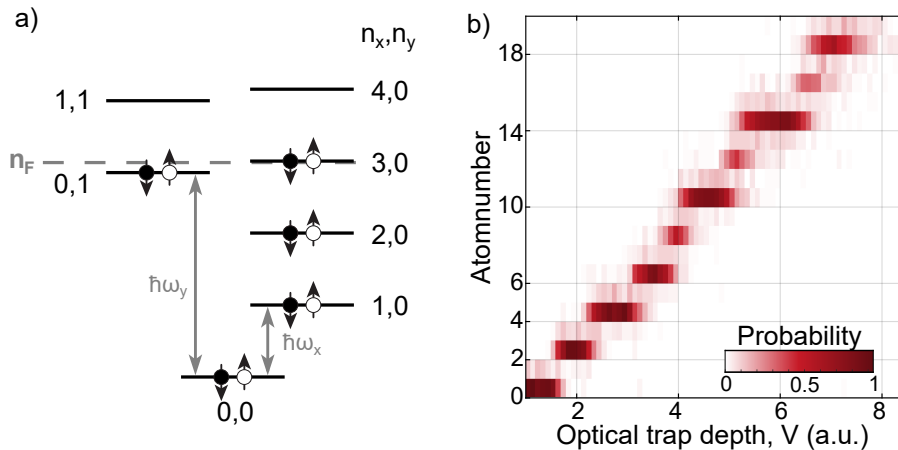


**Figure 5.1: Preparing closed shell configurations in an anisotropic potential.** We prepare the system the ground state of an anisotropic two-dimensional harmonic oscillator potential. The harmonic oscillator levels, labelled by their quantum numbers  $n_x$  and  $n_y$  are sketched in a). Here we mark the closed shell configuration of  $5 + 5$  atoms. Here  $n_F$  b) shows the number of atoms remaining in the trap as a function of the optical trap depth. We can see stable plateaus corresponding to closed shell configurations of the harmonic oscillator potential. Figure adapted from [SB3].

Experimentally, we prepare a spin balanced system in closed shell configurations of a 2D, anisotropic harmonic oscillator potential. The anisotropic potential is created by utilizing an anisotropic aperture phase pattern on the SLM, transforming the initially isotropic beam into an elliptic beam. The ratio of the trap frequencies along the two major axis of the ellipse is indirectly proportional to the ratio of the waists along the two directions. We have chosen the anisotropy such that the trap frequencies are  $(\omega_x, \omega_y)/2\pi = (1280(1), 3384(7))$  Hz.

The anisotropy of the harmonic oscillator potential leads to different closed shell configurations compared to the isotropic case. In the anisotropic case, the harmonic oscillator states are best described by separating the two spatial directions. The Hamiltonian describing the two-dimensional system is separable into the Hamiltonians describing the two independent directions. We choose the spatial directions such that they are aligned with the axis of the ellipse.

## 5.2. Elliptic flow in a mesoscopic Fermi gas

The eigenstates are then given by the quantum numbers  $n_x$  and  $n_y$ , with eigenenergies

$$E_{x(y)} = (n_{x(y)} + 0.5)\omega_{x(y)}. \quad (5.1)$$

As  $\omega_x \neq \omega_y$ , the degeneracy of levels with  $n_x = n_y$  is lifted. The level structure is sketched in Fig. 5.1b). As in the isotropic system (see Sec 3.2), we can prepare closed shell ground state configurations with very high fidelity by lowering the trap depth of the optical tweezer and 'spilling' out atoms. In the anisotropic potential, stable plateaus appear at  $1 + 1$ ,  $2 + 2$ ,  $3 + 3$ ,  $5 + 5$ ,  $7 + 7, \dots$  atoms, as shown in Fig. 5.1a).

### 5.2.2 Observing elliptic flow

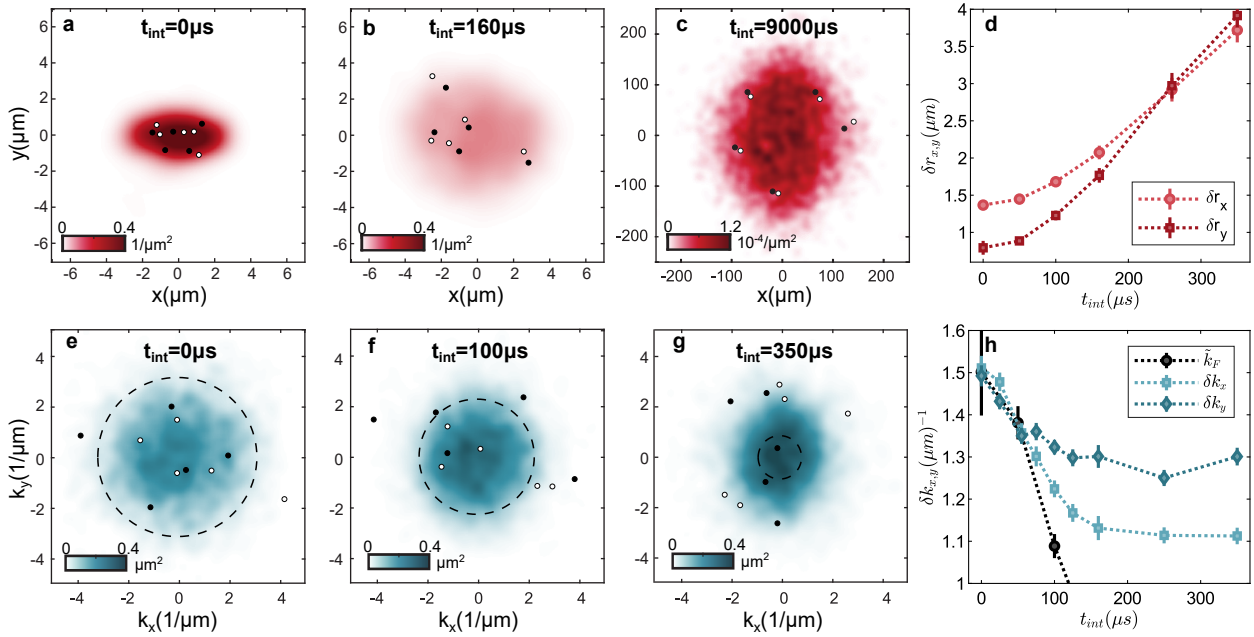


**Figure 5.2: Observation of elliptic flow.** We explore the interacting expansion of a system of  $5+5$  atoms released from an anisotropic 2D harmonic oscillator potential. The initial interaction parameter is  $\ln(k_F^0 a_{2D}) = 1.22$ . We measured their positions (a-c) and momenta (e-g) after different interacting expansion times. The 2D histograms show the measured density distributions, obtained from many experimental realizations of the same quantum states. The densities are overlaid with a single, randomly chosen snapshot of the wave function (white and black dots). The black dashed circles in (e-g) mark the Fermi momentum  $k_F$ , obtained from the real-space peak density. The RMS values of the positions(momenta) along x- and y- direction are shown in d(h). The black data points in h) show a comparison to the Fermi momentum, rescaled to match the initial RMS momentum. All error bars represent the 95 % confidence interval and were obtained using a bootstrapping technique. The connecting line serves as a guide to the eye. Figure adapted from [SB3].

We prepare a system of  $5+5$  atoms in the ground state of the elliptical tweezer, with an initial interaction parameter  $\ln(k_F^0 a_{2D}) = 1.22$  (for more details on the interactions in (quasi)-2D see Sec. 2.3). Here, we approximate the typical momentum with the Fermi wave-vector  $k_F^0 = \sqrt{2mE_F^0/\hbar}$ , where  $E_F^0 = (n_F^x + 1.5)\hbar\omega_x$  is the energy of the non-interacting system, determined by the last filled shell  $n_F^x = 3$ .

To explore the expansion dynamics, we instantaneously quench the radial potential – provided by the OT – off, while keeping the axial confinement – provided by the SWT – on. We image the system in real and momentum space after different expansion times  $t_{\text{int}}$ , utilizing the previously discussed matterwave manipulation techniques (see Chap. 4). At the longest expansion time,  $t_{\text{int}} = 9000 \mu\text{s}$ , the system has expanded enough to be resolvable without matterwave magnification. We obtain the real and momentum space densities from  $\approx 1000$  repeated measurements. The measured densities in real (a-c) and momentum (e-g) space are shown in Fig. 5.2. The density profiles are superimposed with a single, randomly chosen, snapshot of the wave function, shown as black and white points. We quantify the widths of the real and momentum space distribution by their RMS widths,  $\delta r$  and  $\delta k$ , respectively. The measured RMS widths are shown in Fig. 5.2d), real space, and Fig. 5.2h), momentum space.

Initially ( $t_{\text{int}} = 0 \mu\text{s}$ ), the real space density is anisotropic (Fig. 5.2a)), the momentum space distribution however is isotropic (Fig. 5.2e)). In contrast to bosonic systems and the one-body case – where the momentum distribution is sensitive to the anisotropy of the potential [87] – an isotropic momentum space distribution is expected for a degenerate Fermi gas in the many-body limit. If the expansion was purely ballistic, we would observe an isotropic real space distribution after a long expansion time, as the initial momentum distribution is mapped onto real space (see Section. 4.2.2). However, we observe faster expansion along the initially tighter confined  $y$ - direction, which leads to an inversion of the initial aspect ratio after  $t_{\text{int}} = 150 \mu\text{s}$ . Thus, we observe interaction-driven elliptic flow in a system of  $5 + 5$  particles.

We can calculate the Fermi momentum  $k_{\text{F}}(t_{\text{int}}) = \sqrt{4\pi\rho(t_{\text{int}})}$  from the real space density peak density  $\rho(t_{\text{int}}) = N/(2\pi\delta r_x(t_{\text{int}})\delta r_y(t_{\text{int}}))$ .<sup>1</sup> The momentum space width is set by the Fermi-momentum, for times  $t_{\text{int}} < 75 \mu\text{s}$ , as shown in Fig. 5.2h). The decrease in  $\delta k$  occurs concurrently with the decrease of  $\rho(t_{\text{int}})$ . During this initial time, the system remains isotropic in momentum space. The built-up of momentum space anisotropy begins when the Fermi momentum drops significantly below the measured RMS widths (at  $t_{\text{int}} \approx 75 \mu\text{s}$ ) and subsides at  $t_{\text{int}} \approx 120 \mu\text{s}$ .

Our experimental observations demonstrate interaction-driven elliptic flow in a system of only  $5+5$  constituents. Elliptic flow is usually considered as a smoking gun of hydrodynamic behavior. The separation of scales separation of scales commonly associated with a collisional hydrodynamic framework is characterized by the Knudsen number

$$\text{Kn}_i = \frac{\ell_{\text{mfp}}}{\delta r_i}, \quad (5.2)$$

giving the ratio of mean-free path  $\ell_{\text{mfp}}$  and system-size  $\delta r_i$ . Equivalently, the Knudsen number can also be expressed as the ratio of expansion and scattering rate [86]. A collisional hydrodynamic description is justified when  $\text{Kn} \ll 1$ , i.e. when mean free path is much smaller than the system size [58].

In our system of  $5+5$  atoms, the initial system size is  $(\delta r_x, \delta r_y) = (1.37(6), 0.79(9)) \mu\text{m}$ . The mean free path is given by  $\ell_{\text{mfp}} = \sigma/\rho_0$ , where  $\sigma$  is the scattering cross-section (see also Eq. (2.30)). At an interaction strength of  $\ln(k_{\text{F}}^0 a_{2\text{D}}) = 1.22$ , the scattering cross-section is

<sup>1</sup>Note that  $k_{\text{F}}(0) = 3 \mu\text{m}$  is slightly above the Fermi momentum estimated from the non-interacting density  $k_{\text{F}}^0 = 2.3 \mu\text{m}$ . This is due to the fact that the real space density increases with increasing (attractive) interactions.

$\sigma = 1.08 \mu\text{m}$ , slightly below the maximum scattering cross-section of  $\sigma_{\text{max}} = 1.73 \mu\text{m}$ . The measured peak density is  $\rho_0 = 0.73 \mu\text{m}^{-2}$  - resulting in a mean free path of  $\ell_{\text{mfp}} = 1.5 \mu\text{m}$ . This results in a Knudsen number of  $\text{Kn}_x = 1.1$  and  $\text{Kn}_y = 1.89$  along the two spatial directions. Consequently, a collisional hydrodynamic description is not expected to be applicable to our system.

### 5.2.3 Modelling elliptic flow

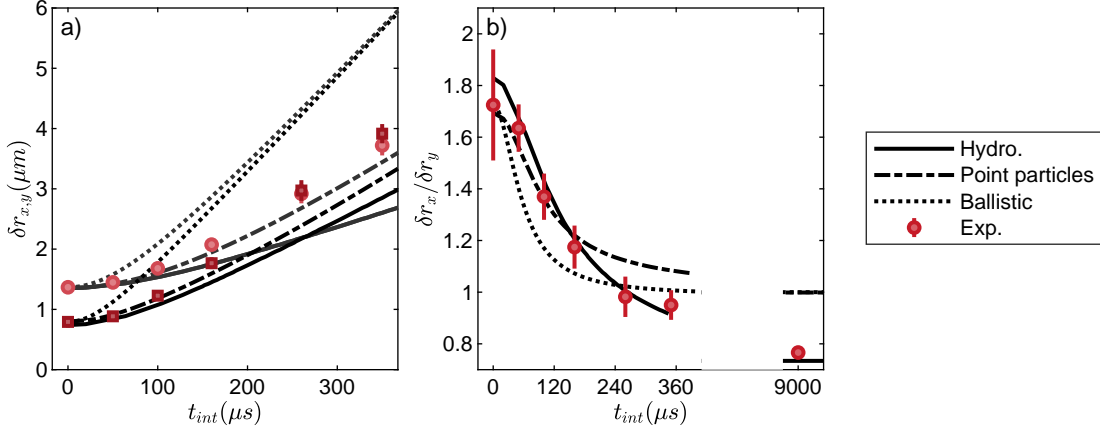


**Figure 5.3: Modelling elliptic flow.** We compare the measured (red data points) real space RMS widths a) and their aspect ratio b) to the results of different simulations. The result of a ballistic expansion of the initial wave function is represented by the black dotted curve. The dashed-dotted curve shows the results of a simulation approximating the scattering process as that of point particles. The full curve shows the results of an ideal hydrodynamic expansion. We observe a quantitative agreement between the observed evolution of the aspect ratio and the prediction of a hydrodynamic evolution. Figure partially adapted from [SB3].

It is instructive to compare the experimental data to different simulations: a ballistic (i.e. non-interacting) expansion of the initial wave function, a simplified scattering model and a hydrodynamic evolution. We compare the results of these different simulations to the measured RMS width in  $x$  and  $y$  direction,  $\delta r_x$  and  $\delta r_y$ , respectively and to the aspect ratio  $\delta r_x / \delta r_y$ . The comparison is shown in Fig. 5.3.

We compute the ballistic, i.e. non-interacting expansion, from the time evolution of the position operator  $\hat{x}(t)$ , see also Equation (4.7). The time evolution of the position operator is given by

$$\hat{x}(t) = \hat{x}(0) \cos(\omega_2 t) + \hat{p}(0) \frac{1}{m_a \omega_2} \sin(\omega_2 t), \quad (5.3)$$

where  $\omega_2 / 2\pi = 20.2(3) \text{ Hz}$  is the trap frequency of the combined radial potential set by the SWT and the magnetic field curvature (for more details see Chap. 4). The RMS width at time  $t$  is given by  $\delta r_x(t) = \sqrt{\langle \hat{x}(t)^2 \rangle}$ . We use the measured RMS widths in real and momentum space as starting conditions and assume a Gaussian initial state with  $\langle \hat{x}\hat{p} \rangle = \langle \hat{p}\hat{x} \rangle = 0$ . We compute the expansion along the two spatial directions independently, as they separate in the non-interacting limit. The comparison to the experimental measurements shows that the ballistic expansion is significantly faster than the observed expansion. This could stem from the fact that the ballistic expansion is not slowed by the redistribution of momenta among the two

axis. The ballistic expansion shows a round aspect ratio after a long expansion time, reflecting the initial momentum space distribution.

For a simplified scattering model, we model the scattering between atoms as elastic scattering of Newtonian, point-like particles. The simulation models the time evolution of six particles in a 2D plane, reflecting that every atom has five potential scattering partners of opposite spin. The initial momenta and positions are randomly drawn out of distributions set by the measured real and momentum space distributions. The particle positions are updated at each time step. When two particles come within a distance given by the 2D scattering cross-section  $\sigma = 1.08 \mu\text{m}$ , an elastic collision occurs and the velocities of the collision partners are updated accordingly. We obtain the RMS of the distribution at different time steps by running the simulation 3000 times. This allows us to compare the results of this classical scattering model to our measurements - see Fig. 5.3. We find good agreement between the widths predicted by the simplified scattering model and the measured RMS widths for times up to  $t_{\text{int}} = 150 \mu\text{s}$ , corresponding to the time at which the redistribution of momenta ceases. The inversion of the aspect ratio at later times is not predicted by the simplified scattering model. Hence, the observed interaction-driven elliptic flow can not be explained by this collisional model. This is expected as the Knudsen number  $Kn_i > 1$ .

For the hydrodynamic simulation, we assume the properties of the corresponding many-body system, with an initial density matched to the measured initial density. The expansion is modelled by solving the Euler

$$\frac{\partial \mathbf{v}}{\partial t} + (\mathbf{v} \nabla) \mathbf{v} = -\frac{1}{\rho} \nabla P \quad (5.4)$$

and continuity equation

$$\frac{\partial \rho}{\partial t} + \nabla(\rho \mathbf{v}) = 0, \quad (5.5)$$

where  $\rho$  is the density,  $P$  is the pressure and  $\mathbf{v} = (v_x, v_y)$  is the fluid velocity vector. The solutions of these equations were obtained using the pyro simulation toolbox [88]. Additionally, the equation of state (EOS) is required, giving the pressure as a function of density. Here, we utilize the EOS of the corresponding many-body system [89]. As the many-body system is a superfluid, we do not add any viscous correction terms. It is important to note that the hydrodynamic equations can be derived from elastic scattering of particles in the limit of infinite particle number and collision rate (i.e.  $N \rightarrow \infty$  and  $Kn \rightarrow 0$ ). The mathematical connection between the macroscopic and microscopic description is a famous example of Hilbert's sixth problem (formulated in 1902) [90] and has only recently been proven mathematically [91, 92].

Looking at the comparison to the experimental results, the hydrodynamic simulation does not capture the RMS width after a time of  $t_{\text{int}} = 100 \mu\text{s}$ . However, the measured aspect ratio is accurately reproduced by the hydrodynamic simulation at all times, including the final inversion of the aspect ratio. This is truly remarkable, considering that both interparticle spacing and mean-free path are comparable to the system size, or, alternatively, that  $N = 5$  and  $Kn > 1$ .

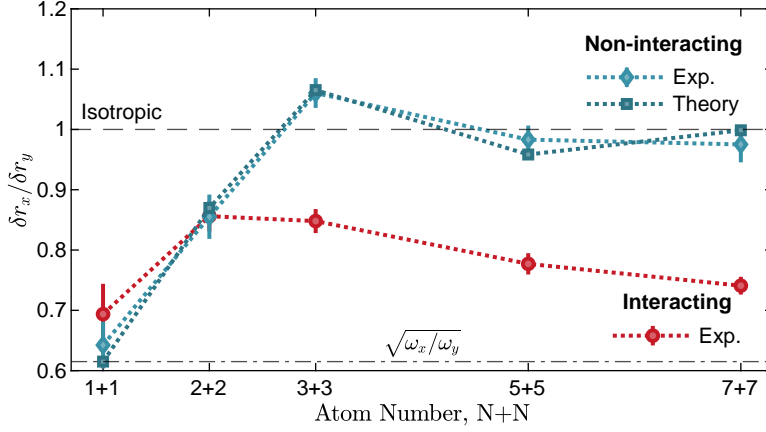


**Figure 5.4: Emergence of elliptic flow.** Aspect ratio of the real space density after an expansion time of  $9000 \mu\text{s}$  for different atom numbers  $N + N$ . The system is prepared in different closed shell configurations of the anisotropic 2D harmonic oscillator potential. We compare the final aspect ratio of a strongly interacting system (red) to that of a non-interacting system (blue dots experimental measurement, blue squares analytical calculation). We observe an interaction-driven inversion of the initial aspect ratio starting from  $3 + 3$  atoms. All error bars represent the 95% confidence interval and were obtained using a bootstrapping technique. The connecting lines serve as a guide to the eye. Figure adapted from [SB3].

### 5.3 Emergence of interaction-driven elliptic flow

Our deterministic control over the atom number allows us to identify the atom number at which collective behavior seizes. Naturally, this number is not expected to be universal, but depends on the specific system parameters such as geometry and interaction strength. Fig. 5.4 shows the measured aspect ratio  $\delta r_x / \delta r_y$  after a long expansion time  $t_{\text{int}} = 9000 \mu\text{s}$  for different atom numbers  $N + N$ . These correspond to closed shell configurations of the anisotropic harmonic oscillator (see Sec. 5.2.1). To verify the emergence of interaction-driven elliptic flow, we compare the measured final aspect ratio of the strongly interacting system to measurements in the non-interacting limit.

In the non-interacting limit, the long expansion time is equivalent to a mapping of momentum space on real space. Consequently, our measurements show the built-up of an isotropic momentum space distribution with increasing atom number. For a single atom, the aspect ratio is (within the error) equal to  $\sqrt{\omega_x / \omega_y}$ , as is expected considering that the harmonic oscillator momentum is proportional to  $\sqrt{\omega_i}$ . As more particles are added to the system, the distribution becomes isotropic. As the system is non-interacting, the initial momentum space density is given by the ground-state density of an anisotropic harmonic oscillator which can be analytically calculated. We find excellent agreement between the calculated and measured aspect ratios.

In the interacting system, we observe an inversion of the initial aspect ratio for all atom numbers. However, for  $1 + 1$  and  $2 + 2$  atoms, there is no significant deviation between the final aspect ratio measured in the interacting and non-interacting system. Starting from  $3 + 3$  atoms, the aspect ratio after the interacting expansion differs significantly from that observed after the non-interacting expansion. Here, the inversion of the aspect ratio is driven by interactions and

is not just due to the initial momentum space distribution.

## 5.4 Interaction dependence

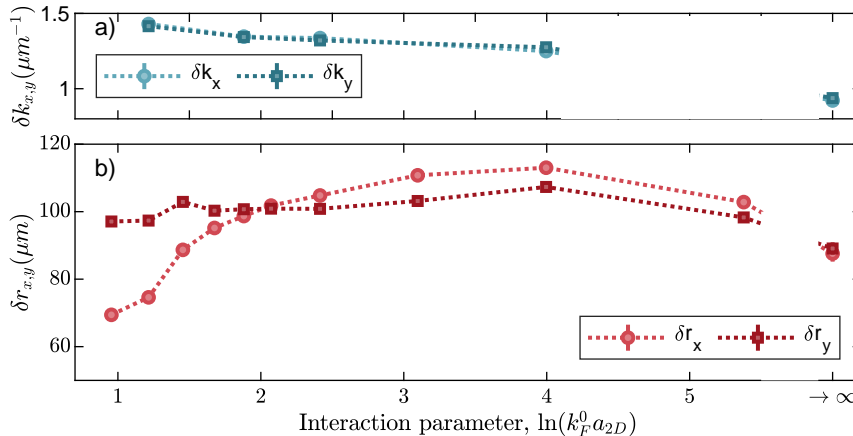


**Figure 5.5: Interaction dependence.** Measured initial momentum space RMS widths a) and real space widths after an interacting expansion time  $t_{\text{int}} = 9000 \mu s$  b) for a system of 5+5 atoms with different initial interaction parameters. We observe an interaction driven inversion of the initial aspect ratio for  $\ln(k_F^0 a_{2D}) < 2$ . All error bars represent the 95% confidence interval and were obtained using a bootstrapping technique. The connecting lines serve as a guide to the eye. Figure adapted from [SB3].

The tunability of the interaction strength allows us to investigate the expansion of a system of 5+5 atoms at different interaction strengths. The initial momentum space widths  $\delta k$  are shown in Fig. 5.5a), the measured widths after a long, interacting expansion time are shown in Fig. 5.5b). The initial momentum space widths increase with increasing interaction strength (i.e. decreasing  $\ln(k_F^0 a_{2D})$ ). This reflects the decrease of the real space width with increasing attractive interactions. The initial momentum space width is isotropic at all interaction strengths. As a consequence, any anisotropy of the final real space distribution is necessarily due to interactions.

In the strongly interacting system with  $\ln(k_F^0 a_{2D}) < 2$ , we observe elliptic flow. Here, the real space density is anisotropic with  $\delta r_x < \delta r_y$  after a long interacting expansion time. While the width along the initially strongly confined  $y$ -direction stays almost constant as a function of interaction strength, the width in  $x$ -direction decreases with increasing interaction strength. Thus, the final aspect ratio  $\delta r_x / \delta r_y$  decreases with increasing interaction strength. At an interaction strength of  $\ln(k_F^0 a_{2D}) = 2$ , the density is isotropic with  $\delta r_x = \delta r_y$ .

In the non-interacting limit ( $\ln(k_F^0 a_{2D}) \rightarrow \infty$ ), the final aspect ratio is isotropic ( $\delta r_x = \delta r_y$ ), reflecting the initial aspect ratio in momentum space. However, at intermediate interaction strengths  $\ln(k_F^0 a_{2D}) > 2$ , we observe a peculiar behavior. Here,  $\delta r_x > \delta r_y$ , reflecting the anisotropy of the initial real space distribution. Similar behavior has been predicted for a weakly-interacting, macroscopic, three-dimensional Fermi gas in the normal phase [93]. There, the system is assumed to be collisionless and the expansion is modelled using the Vlasov equations [94], in which the interactions are incorporated as a mean-field term [93, 95]. For attractive interactions, this mean field term causes a slower expansion along the initially tightly confined

direction. As a consequence the density after a long interacting expansion exhibits a weak anisotropy, reflecting the initial anisotropy of the system. In our 2D system, the mean-field interactions are attractive, for  $\ln(k_F^0 a_{2D}) > 0$ , potentially resulting in a similar expansion behavior.

## 5.5 Conclusion and Outlook

In conclusion, we have observed interaction-driven elliptic flow in a system of few fermionic atoms, where the separation of scales required for a hydrodynamic description is absent, drawing a connection to the collective behavior observed in proton-proton collisions. We compare our experimental measurements to different theoretical models and find that the evolution of the aspect ratio is captured remarkably well by a hydrodynamic model, but not by a collisional model.

By tuning the particle number, we investigate the emergence of collective behavior from the bottom up and observe interaction-driven elliptic flow starting from a system of 3+3 atoms. Tuning the interaction strength reveals two different interaction regimes: A regime of strong interactions, where the initial aspect ratio is inverted after a long interacting expansion time and a regime of weak interactions, where the aspect ratio is not inverted but rather preserved. In a collisionless many-body system, such an effect is the consequence of an attractive mean-field interaction.

### 5.5.1 On the question of superfluidity

A tempting explanation for the observed behavior is that our system can be described by superfluid hydrodynamics in the strongly interacting regime. While the hydrodynamic behavior in a normal fluid stems from collisions among the particles, in a superfluid, it is the result of the occurrence of an order parameter [87, 96].

Let us take a quick detour to a bosonic system to understand the significance of the order parameter, based on considerations in [87, 96]. The single particle density matrix  $\rho(\mathbf{r}, \mathbf{r}', t)$  is defined as

$$\rho(\mathbf{r}, \mathbf{r}', t) \equiv \langle \hat{\Psi}^\dagger(\mathbf{r}, t) \hat{\Psi}(\mathbf{r}', t) \rangle \quad (5.6)$$

where  $\hat{\Psi}(\mathbf{r}, t)$  is the bosonic field operators creating a particle in point  $\mathbf{r}$ . This single particle density matrix is Hermitian and can thus be written as

$$\rho(\mathbf{r}, \mathbf{r}') = \sum_i n_i \xi_i^*(\mathbf{r}) \xi_i(\mathbf{r}') \quad (5.7)$$

where  $n_i$  are the real eigenvalues of  $\rho(\mathbf{r}, \mathbf{r}')$  and  $\xi_i$  are the corresponding, normalized, eigenvectors, forming a complete orthogonal set. When one eigenvalue is of the same order as the particle number  $N$ , the system exhibits Bose-Einstein condensation [97]. This is equivalent to the existence of off-diagonal long-range order in the system [98]. The order parameter is then defined as

$$\psi(\mathbf{r}, t) \equiv \sqrt{N_0} \xi_0(\mathbf{r}, t) \quad (5.8)$$

where  $N_0$  and  $\xi_0$  are the eigenvalue and eigenvector of the state with eigenvalue on the order of  $N$ .

The dynamics of the order parameter are described by a time-dependent Schrödinger-like equation, which can be rewritten in the form of the classical Euler and continuity equation (see Eq. (5.4) and (5.5)) for an inviscid, irrotational fluid using the Madelung transformation [99, 100]. The (superfluid) velocity  $\mathbf{v}_s(\mathbf{r}, t)$  is connected to the phase  $\varphi(\mathbf{r}, t)$  of the order parameter with

$$\mathbf{v}_s(\mathbf{r}, t) \equiv \frac{\hbar}{m_a} \nabla \varphi(\mathbf{r}, t). \quad (5.9)$$

In a fermionic system, none of the eigenvalues of  $\rho(\mathbf{r}, \mathbf{r}')$  can be higher than unity. This is set by Pauli's exclusion principle. However, a macroscopic occupation (on order  $N$ ) of eigenstates of the two particle density matrix  $\rho_2(\mathbf{r}_1, \mathbf{r}_2, \mathbf{r}'_1, \mathbf{r}'_2, t)$  is possible [98]. We can then write the order parameter as [96]

$$F(\mathbf{r}, \mathbf{r}') \equiv \sqrt{N_0} \xi_0(\mathbf{r}, \mathbf{r}', t) \quad (5.10)$$

similarly as in the bosonic system. The superfluid velocity can also be defined as above, replacing the mass of a single atom with that of a pair.

From these considerations we can see that the formation of pairs is a necessary (but not sufficient) criterion for superfluidity in fermionic systems. The formation of pairs in a mesoscopic Fermi gas is discussed in depth in Chapter 6. We can also see that the expansion of the superfluid system is described by the same equations as the expansion of a collisional fluid. Therefore, the previously discussed measurements fundamentally do not allow us to distinguish between a superfluid and a collisional fluid. To make this distinction we would have to test the rotational properties of the system [101] or verify that it fulfills the Landau criterion [102].

Experimentally, superfluidity has been observed in the rotational behavior of a system comprising only 60  $^4\text{He}$  atoms immersed in a  $^3\text{He}$  droplet [103]. Monte-Carlo simulations predict superfluid like behavior in even smaller clusters of 13  $p - H_2$  molecules [104]. Considering these observations it would be interesting to explore the emergence of superfluid behavior in a mesoscopic Fermi gas.



## 6 | Pairing: from shell to bulk

'And then there's quantum of course' the monk  
sighed 'there's always bloody quantum'

---

SIR TERRY PRATCHETT  
*Night Watch, 2002*

The (closely related) phenomena of superconductivity and superfluidity result from the macroscopic occupation of a quantum state. In bosonic systems, this occurs when the constituents condense in a single-particle state. However, in a system of fermions, Pauli's exclusion principle permits, at maximum, unity occupation of each single-particle state. This fundamental limitation means that individual fermions cannot form a coherent, macroscopically occupied state. However, the macroscopic occupation of a two-particle state is not excluded by Pauli's principle [98]. Consequently, the fundamental ingredient for superconductivity and superfluidity in fermionic systems is the formation of pairs.

When the attractive interactions between fermions are sufficiently strong, pairs of fermions may form tightly bound molecules, and the system can behave like a collection of composite bosons. At weaker interactions, fermions of opposite momentum close to the Fermi surface form Cooper pairs. In continuous systems, this mechanism was established by Cooper [105], leading to the well-known Bardeen, Cooper, and Schrieffer (BCS) theory [106].

Anderson [107] generalized pairing between states of opposite momentum to pairing between time-reversed states. This extended framework allows for a description of so-called 'dirty' superconductors, where translation invariance is broken by physical or chemical impurities. Beyond that, it also applies to nuclear systems, where translational symmetry is broken by the nuclear mean-field potential, allowing for a description of pairing between nucleons [108, 109].

In this chapter, we report on the observation of distinct pairing regimes in a 2D harmonic oscillator potential. By tuning the system parameters, we transition from a regime where pairing is best described by time-reversed harmonic oscillator states to a regime where the discrete level structure becomes negligible, and the potential primarily determines the local density. We here bridge the gap between the Cooper picture and the more generalized Anderson framework, shedding light on how confinement influences pairing correlations.

*This chapter is based on a paper in preparation. The experimental work and data analysis were conducted by the author, Carl Heintze, Maciej Galka and Selim Jochim, the calculations in the potential-dominated regime were done by Georg Bruun. Fabian Brauneis and Stephanie Reimann performed the numerical exact diagonalization. The measurements in momentum space are partially based on [SB1].*

## 6.1 Translation invariant systems

The discussion in this section is based on books [87, 96, 110, 111] and review articles [22] on BCS theory. We refer the reader to these references for a more in-depth discussion.

A system of  $2N$  fermions of mass  $m_a$ , in two spin states (with  $N$  atoms per spin-state), interacting via contact interactions (with coupling constant  $g$ ), is described by the Hamiltonian

$$\hat{H} = \sum_{i=1}^{2N} \left( \frac{\hat{\mathbf{p}}_i^2}{2m_a} \right) + g_{(D)} \sum_{k,l} \delta^{(D)}(\hat{\mathbf{r}}_k - \hat{\mathbf{r}}_l), \quad (6.1)$$

in  $D$  dimensions and in absence of a confining potential. The indices  $k$  and  $l$  denote the two different spin states,  $\hat{\mathbf{p}}$  and  $\hat{\mathbf{r}}$  are the momentum and position operators, respectively. The first term of the Hamiltonian represents the kinetic energy, the second term the interactions between two particles of different spin.

Let us first consider the simplified scenario of two weakly interacting fermions on top of a non-interacting Fermi sea - the famous *Cooper problem* [105]. While in a 2D system the interaction potential always supports a two-body bound state (see Sec. 2.3), this is not necessarily the case in a  $D$ -dimensional system (as for example in 3D). However, as shown by Cooper [105], the presence of a Fermi sea modifies the density of scattering states. The density of states is constant at the Fermi surface, giving rise to a bound state at arbitrarily weak interactions also in 3D. As the number of available scattering states is largest for pairs with zero center-of-mass momentum, Cooper pairs form between atoms of opposite momentum on the Fermi surface [22, 110].

The considerations of Cooper only account for the interactions of the two atoms on top of a non-interacting Fermi sea. Based on the insight of Cooper that pairing occurs between atoms of opposite momenta, Bardeen, Cooper, and Schrieffer formulated a model Hamiltonian describing the many-body system in second quantization [106]

$$\hat{H}_{\text{BCS}} = \sum_{p\sigma} \epsilon_p \hat{a}_{p,\sigma}^\dagger \hat{a}_{p,\sigma} + \frac{g_{(D)}}{V} \sum_{p,p'} \Gamma_{p,p'} (\hat{a}_{p,\uparrow}^\dagger \hat{a}_{-p,\downarrow}^\dagger \hat{a}_{-p',\downarrow} \hat{a}_{p',\uparrow}), \quad (6.2)$$

limiting the interaction term of 6.1 to pairs of opposite momenta. Here,  $V$  is the volume and the operator  $\hat{a}_{p,\sigma}^\dagger$  ( $\hat{a}_{p,\sigma}$ ) creates (annihilates) a fermion with spin  $\sigma$  and momentum  $p$ . The energy  $\epsilon_p = \frac{p^2}{2m} - \mu$  denotes the energy of the state with momentum  $p$ , relative to the chemical potential  $\mu$ . At weak interactions, the matrix element  $\Gamma_{p,p'}$  is non-zero only in a small region around the Fermi surface. In this regime of weak interactions, the chemical potential can be approximated by the Fermi energy.

We can obtain an approximate solution to this problem by employing a mean-field approach [110, 111]. Here, the pair operator

$$\hat{P} = \frac{g_{(D)}}{V} \hat{a}_{p,\uparrow} \hat{a}_{-p,\downarrow} \quad (6.3)$$

is replaced with its mean-field expectation value  $\sum_p \langle \hat{P} \rangle = \Delta$ , resulting in

$$\hat{H}_{\text{BCS}} = \sum_{p\sigma} \epsilon_p \hat{a}_{p,\sigma}^\dagger \hat{a}_{p,\sigma} + \sum_p (\Delta \hat{a}_{p,\uparrow}^\dagger \hat{a}_{-p,\downarrow}^\dagger + \Delta \hat{a}_{p,\uparrow} \hat{a}_{-p,\downarrow}) + \frac{V|\Delta|^2}{g_{\text{(D)}}}. \quad (6.4)$$

The parameter  $\Delta$  sets the size of the superfluid gap [110, 111]. It is vital to note that the mean-field Hamiltonian does not conserve particle number, as is evident due to the  $\hat{a}_{p,\uparrow}^\dagger \hat{a}_{-p,\downarrow}^\dagger$  term.

The mean-field Hamiltonian can be diagonalized with the Bogoliubov de Gennes transformation [112], i.e. by introducing quasi particle operators

$$\begin{aligned} \hat{\gamma}_{p,\uparrow} &= u_p \hat{a}_{p,\uparrow} - v_p \hat{a}_{-p,\downarrow}^\dagger \\ \hat{\gamma}_{p,\uparrow}^\dagger &= u_p \hat{a}_{p,\uparrow}^\dagger + v_p \hat{a}_{-p,\downarrow}, \end{aligned} \quad (6.5)$$

where  $u_p$  and  $v_p$  are solutions of

$$E_p \begin{bmatrix} u_p \\ v_p \end{bmatrix} = \begin{bmatrix} \epsilon_p & \Delta \\ \Delta & -\epsilon_p \end{bmatrix} \begin{bmatrix} u_p \\ v_p \end{bmatrix}. \quad (6.6)$$

This leads to  $v_p^2 = \frac{1}{2} \left(1 - \frac{\epsilon_p}{E_p}\right)$  and  $u_p^2 = \frac{1}{2} \left(1 + \frac{\epsilon_p}{E_p}\right)$ , with  $E_p = \sqrt{\epsilon_p^2 + |\Delta|^2}$ . The BCS ground state wave function is then given by [106]

$$|\psi_{\text{BCS}}\rangle = \mathcal{N} \prod_p \hat{\gamma}_{-p,\downarrow} \hat{\gamma}_{p,\uparrow} |0\rangle = \prod_p (u_p + v_p \hat{a}_{p,\uparrow}^\dagger \hat{a}_{-p,\downarrow}^\dagger) |0\rangle \quad (6.7)$$

where  $|0\rangle$  is the vacuum state of the particle operators  $\hat{a}_{p,\sigma} |0\rangle = 0$ <sup>1</sup>. The BCS ground state is free of excitations, consequently  $\hat{\gamma}_{p,\sigma} |\psi_{\text{BCS}}\rangle = 0$ .

The occupation probability  $n_p$  of the state with momentum  $p$  is

$$\begin{aligned} n_p &= \langle \psi_{\text{BCS}} | \hat{a}_{p,\uparrow}^\dagger \hat{a}_{p,\uparrow} | \psi_{\text{BCS}} \rangle = \langle \psi_{\text{BCS}} | \hat{a}_{p,\downarrow}^\dagger \hat{a}_{p,\downarrow} | \psi_{\text{BCS}} \rangle \\ &= v_p^2 = 1 - u_p^2. \end{aligned} \quad (6.8)$$

The coefficients  $v_p^2$  and  $u_p^2$  thus give the particle and hole occupation probabilities, respectively. For  $\Delta = 0$ ,  $n_p$  takes the form of the characteristic step function, where all states below the chemical potential (which here coincides with the Fermi energy) are fully occupied, and all states above are unoccupied. For small  $\Delta$  the occupation of a few states around the Fermi energy is altered. As the interaction strength increases, the change in occupation extends to progressively more states.

The pair wave function can be expressed as [22]

$$\langle \psi_{\text{BCS}} | \hat{a}_{p,\uparrow}^\dagger \hat{a}_{-p,\downarrow}^\dagger | \psi_{\text{BCS}} \rangle = u_p v_p. \quad (6.9)$$

Hence, pair formation occurs in states with both a non-zero particle and non-zero hole occupation probability. Considering the change in  $n_p$  discussed above, we can see that for weak

<sup>1</sup>Note that we use a compact notation throughout this thesis, writing  $\hat{a}_{p,\sigma} |0\rangle = 0$  instead of  $\hat{a}_{p,\sigma} |0\rangle = 0 |0\rangle$ .

interactions, pairing is constrained to few states around the Fermi surface – the *Cooper pair regime*. As we increase the interactions, pairing is no longer constrained to the Fermi surface. When the occupation of each state becomes far smaller than unity, the fermionic nature of the constituents of the pair can be disregarded [22]. The system can then be effectively described as a gas of tightly bound bosonic molecules. These two regimes define the limits of the BEC-BCS crossover.

## 6.2 Broken translational symmetry

*The general introduction on pairing in systems with broken translational symmetry is based on the original publication by Anderson [107], books [113] and lecture notes [114]*

Motivated by the observation that superconductivity persists in dirty superconductors, i.e. superconductors that exhibit a high degree of (non-magnetic) impurities, Anderson introduced the notion of pairing between time-reversed eigenstates of the single-particle Hamiltonian [107]. This notion extends the BCS framework to systems with broken translational symmetry (e.g. due to impurities in the dirty superconductor), for which momentum is not a good quantum number. Time-reversed states are connected by the time reversal operator

$$\hat{T} : t \rightarrow -t, i \rightarrow -i. \quad (6.10)$$

While  $\hat{T}$  does not change the position operator, it reverses the sign of e.g. the momentum  $\hat{p} = -i\hbar \frac{\partial}{\partial x}$  and angular momentum operator [115]. As the states  $p \uparrow$  and  $-p \downarrow$  are a time-reversed pair, Anderson's theory is a generalization of the original BCS theory [106].

The approach of Anderson is to first find the eigenstates of the single-particle Hamiltonian and then solve the BCS problem in terms of these states and their time-reversed partners. The most general single-particle Hamiltonian describing a system with broken translational symmetry is given by

$$\hat{H}_{\text{SP}} = \frac{\hat{\mathbf{p}}^2}{2m_a} + V(\hat{\mathbf{r}}), \quad (6.11)$$

where  $m_a$  is the mass of the particle,  $\hat{\mathbf{p}}$  is the momentum operator and  $V(\hat{\mathbf{r}})$  is some position dependent potential. Given that the Hamiltonian  $\hat{H}_{\text{SP}}$  is time reversal symmetric, i.e.

$$[\hat{H}_{\text{SP}}, \hat{T}] = 0 \quad (6.12)$$

every eigenstate  $\psi_{n,\sigma}$  of  $\hat{H}$  has a time-reversed partner,  $\hat{T}\psi_{n,\sigma}$ , that is degenerate in energy. Pairing takes place between these time-reversed states. This description in terms of single-particle states is valid as long as the superfluid gap is smaller than the single-particle gap of the spatially varying potential  $V(\hat{\mathbf{r}})$  [107].

This approach is also utilized to understand properties of the nucleus [108]. The nucleus is a self-bound system in which the average interactions between all nucleons gives rise to a position dependent potential  $V(\hat{\mathbf{r}})$  - the nuclear mean-field. The individual nucleons then occupy the single-particle states of this mean-field potential. This description of the nucleus is referred to as the shell model [116, 117]. In addition to the mean-field potential, the short range part of the nuclear force gives rise to pairing - as is evident from the observation that nuclei with

an even number of protons or neutrons are more strongly bound than nuclei with odd proton or neutron numbers. As the pairing force is weak compared to the single particle gap of the nuclear mean field, pairing can be modelled as pairing between time-reversed single-particle states around the Fermi surface [107, 113, 118, 119].

### 6.2.1 Broken time-reversal symmetry

To understand the consequence of broken time reversal symmetry, it is interesting to consider a rotation of the confining potential in a reference frame with rotational frequency  $\Omega_{\text{rot}}$ . Here the single-particle Hamiltonian is given by

$$\hat{H}_{\text{rot}} = \hat{H}_{\text{SP}} - \Omega_{\text{rot}} \hat{L}_z, \quad (6.13)$$

where  $\hat{L}_z$  is the projection of the angular momentum operator  $\hat{\mathbf{L}} = \hat{\mathbf{r}} \times \hat{\mathbf{p}}$ . It is evident that this Hamiltonian is not symmetric under time reversal, which causes a sign change of the last part describing the rotation. The time reversed states of  $\hat{H}_{\text{SP}}$  are then separated by a gap, set by the rotational frequency. At a fixed interaction strength, there is thus a critical rotation frequency above which pairing is suppressed.

In nuclear physics a closely related effect – known as the Mottelson-Valatin effect [120] – predicts the break-down of pairing (and thus superfluidity) in nuclei with large angular momenta. This breaking of pairs can give rise to a back-bending of the Yrast<sup>2</sup> line, giving the minimum energy as a function of the angular momentum of the nucleus [113, 122]. Due to the analogy between rotation and magnetic field, these considerations also connect to the breakdown of superconductivity at a critical magnetic field strength, observed in type-I superconductors. Hence, the Mottelson-Valatin effect is commonly referred to as a “nuclear Meissner effect”.

## 6.3 Pairing in a harmonic oscillator potential

We explore pairing in a stationary, rotationally symmetric, 2D harmonic oscillator potential (sketched in Fig. 6.1). The Hamiltonian describing  $2N$  fermions in 2 spin states in a rotationally symmetric 2D harmonic oscillator potential is given by

$$\hat{H} = \sum_{i=1}^{2N} \left( \frac{\hat{\mathbf{p}}_i^2}{2m_a} + \frac{1}{2} \underbrace{m_a \omega_r \hat{\mathbf{r}}_i^2}_{V(\hat{\mathbf{r}})} \right) + g_{2\text{D}} \sum_{i,j} \delta^{(2)}(\hat{\mathbf{r}}_i - \hat{\mathbf{r}}_j), \quad (6.14)$$

where  $\omega_r$  is the angular frequency of the harmonic oscillator. The three terms of the Hamiltonian can be related to three different energy scales: the kinetic energy term is related to the interparticle spacing and thus the Fermi energy  $E_{\text{F}}$ . The harmonic confinement exhibits a shell structure with a single particle gap  $\hbar\omega_r$ . The interactions can be characterized by the two-particle binding energy  $E_{\text{B}}$ , defined as the binding energy per pair. Here it is important to note that the quasi-2D harmonic oscillator potential alters the binding energy compared to the

<sup>2</sup>Sometimes ‘Yrast’ - the superlative of the Swedish word ‘Yr’ is translated as whirligiest (superlative of whirly). However, a dictionary will show you that the literal – and maybe more fitting – translational is dizziest [121].

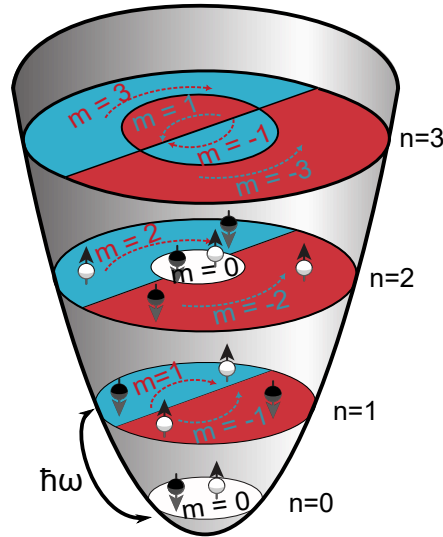


**Figure 6.1: Single-particle spectrum of a 2D harmonic oscillator.** The single-particle states of a rotationally symmetric 2D harmonic oscillator are labelled by the principal quantum number  $n$  and the angular momentum quantum number  $m$ . The  $n$ -th energy level exhibits an  $n + 1$ -fold degeneracy.

uniform 2D case discussed in Sec. 2.3.3. We obtain the two-body binding energy in the trap following calculations in [60]. More details on the deviation can also be found in [32, 33, 123].

In the regime of weak interactions, we can use Anderson's approach to understand pairing in this system. The *single-particle* eigenstates in real space coordinates are given by

$$\langle x|n, m\rangle = \psi_{n,m}(r, \theta) = \underbrace{\sqrt{\frac{k!}{\pi(k + |m|)!}} r^{|m|} \exp(-\frac{r^2}{2}) L_k^{|m|}(r^2) e^{im\theta}}_{R_{n,m}(r)}, \quad (6.15)$$

where  $n$  is the principal/shell quantum number,  $m = -n, -n+2, \dots, +n$  is the angular momentum quantum number,  $k = 0.5(n - |m|)$ ,  $r$  is given in units of the harmonic oscillator length  $l_{\text{HO}} = \sqrt{\hbar/m_a\omega_r}$  and  $L_k^{|m|}$  is the generalized Laguerre polynomial of degree  $k$ . The *single-particle* eigenenergies are given by

$$E_n^0 = (n + 1)\hbar\omega_r. \quad (6.16)$$

As the time reversal operator changes the sign of the angular momentum  $m$ , the time-reversed partner of each eigenstate  $|n, m\rangle$  is  $|n, -m\rangle$ . It is apparent that these time-reversed states are degenerate in energy.

A BCS-like Hamiltonian can now be written in terms of the time-reversed states  $|n, -m\rangle$  and  $|n, m\rangle$  [107, 124]

$$\hat{H} = \sum_{n,m,\sigma} \epsilon_n \hat{a}_{n,m,\sigma}^\dagger \hat{a}_{n,m,\sigma} + \sum_{n,n',m,m'} V_{n,m,n',m'} (\hat{a}_{n,m,\uparrow}^\dagger \hat{a}_{n,-m,\downarrow}^\dagger \hat{a}_{n',-m',\downarrow} \hat{a}_{n',m',\uparrow}) \quad (6.17)$$

where  $\epsilon_n = (n + 1)\hbar\omega_r - E_F$  denotes the energy of state  $n$  relative to the Fermi energy and  $\hat{a}_{n,m,\sigma}^\dagger$  ( $\hat{a}_{n,m,\sigma}$ ) creates (annihilates) a particle with spin  $\sigma$  in state  $|n, m\rangle$ . Following the same

mean-field argument as in Sec. 6.1, the Hamiltonian can be rewritten as

$$\hat{H} = \sum_{n,m,\sigma} \epsilon_n \hat{a}_{n,m,\sigma}^\dagger \hat{a}_{n,m,\sigma} + \sum_{n,m} \Delta (\hat{a}_{n,m,\uparrow}^\dagger \hat{a}_{n,-m,\downarrow}^\dagger + \text{h.c.}), \quad (6.18)$$

where  $\Delta$  is the pairing gap.

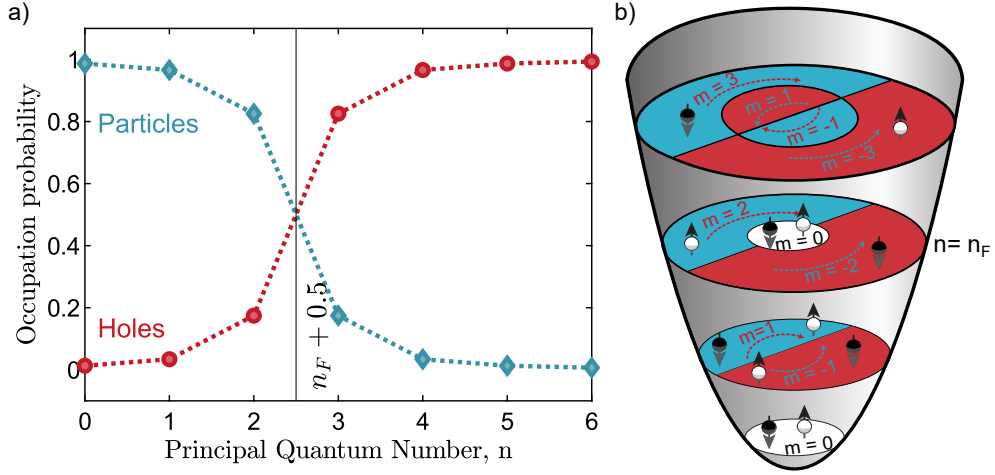


**Figure 6.2: Pair and Hole Occupation probabilities.** The pair and hole occupation probabilities as a function of the principal quantum number for a system with  $E_B > E_B^C$ . b) shows a sketch of the occupied levels.

Analogously to the standard BCS Hamiltonian, this Hamiltonian can be diagonalized using the Bogoliubov de Gennes transformation [112], i.e. by introducing quasi particle operators

$$\begin{aligned} \hat{\gamma}_{n,m,\uparrow} &= u_{n,m} \hat{a}_{n,m,\uparrow} - v_{n,-m}^* \hat{a}_{n,-m,\downarrow}^\dagger \\ \hat{\gamma}_{n,m,\downarrow}^\dagger &= u_{n,-m}^* \hat{a}_{n,-m,\downarrow} + v_{n,m} \hat{a}_{n,m,\uparrow}^\dagger \end{aligned} \quad (6.19)$$

with  $u_{n,m}^2 = 1/2(1 + \epsilon_n/E_n) = 1 - v_{n,m}^2$  and  $E_n = \sqrt{\epsilon_n^2 + \Delta^2}$ . Here  $\epsilon_n = E_n^0 - E_F$  gives the energy of the  $n$ th state relative to the Fermi energy.

As in the uniform case (see Eq. (6.8)),  $v_{n,m}^2$  gives the particle occupation probability of the state  $|n, m\rangle$  and  $u_{n,m}^2$  gives the hole occupation probability. The occupation probabilities for particles and holes for a system with  $E_F/\hbar\omega_r = 4.5$  ( $n_F = 3$ ) and  $\Delta/\hbar\omega_r = 0.6$  are shown in Figure 6.2. The weak interactions only alter the occupation of few states around the Fermi surface, i.e. around  $n_F$ . Pairs form in states with non-zero particle and hole occupation probabilities. As a consequence, pairing is, in this weakly interacting limit, restricted to a few shells around  $n_F$ .

The pairing gap  $\Delta$  depends on the occupation of the last filled harmonic oscillator shell  $n_F$  [124, 125]. When there are unoccupied states in the last shell, the Fermi energy is equal to the energy of the last filled shell  $E_F = (n_F + 1)\hbar\omega_r$ . Here, pairing will occur at arbitrarily weak interactions – similarly to the continuous system discussed in Sec. 6.1 – within the last filled shell  $n_F$ . However, when all states up to and including  $n_F$  are completely filled, the Fermi energy lies between the last filled and the first empty shell  $E_F = (n_F + 3/2)\hbar\omega_r$ . The gap in the single-particle spectrum (set by  $\hbar\omega_r$ ) gives rise to a critical interaction strength, in the many-body limit. At this interaction strength, the system will transition from an unpaired

to a paired state, as pairing is only possible when it is energetically favorable to excite a pair from the Fermi surface to the first unfilled shell. The emergence of this phase transition was predicted in [124, 126] and observed in [127].

The critical binding energy  $E_B^c$  in the filled shell configuration, is given by [124]

$$E_B^c/\hbar\omega_r = \frac{B(n_F)}{\zeta(2)} \left( \sqrt{1 + 4\frac{\zeta(2)}{B(n_F)^2}} - 1 \right), \quad (6.20)$$

where  $B(n_F) = 0.577 + 4 \ln 2 + \ln n_F$  and  $\zeta$  is the Riemann zeta function. Below this critical binding energy, pairing is energetically unfavorable. For binding energies  $E_B$  larger than the critical binding energy, the pairing gap is given by [124]

$$\Delta/\hbar\omega_r = \frac{1}{\sqrt{7\zeta(3)}} \sqrt{\frac{2\hbar\omega_r}{E_B^c} - \frac{2\hbar\omega_r}{E_B} + \zeta(2) \left( \frac{E_B}{2\hbar\omega_r} - \frac{E_B^c}{2\hbar\omega_r} \right)}. \quad (6.21)$$

$\Delta$  is spatially constant and dependent only on the highest filled level  $n_F$  and the binding energy [124]. Note that these results were derived in the mean-field limit. In the few-body limit the phase transition is softened to a crossover, and pairing can also occur below the critical interaction strength [126, 127].

The description of pairing in terms of the time reversed states  $|n, m\rangle$  and  $|n, -m\rangle$  is applicable as long as coupling between states with different principal quantum number  $n$  and  $n'$  is negligible. The pairing strength between states  $|n, m\rangle$  and  $|n', -m\rangle$  is given by the matrix element [125]

$$\langle n, m | \Delta | n', -m \rangle = \int_0^\infty dr r \Delta R_{n,m}(r) R_{n',-m}(r), \quad (6.22)$$

where  $\Delta$  is the pairing gap and  $R_{n,m}(r)$  is the radial part of the harmonic oscillator wave function (see Eq. (6.15)). While  $\Delta$  is - in our case - strictly positive, the sign of  $R_{n,m}(r)$  fluctuates as a function of  $r$ . Hence, the coupling between states in different levels ( $n \neq n'$ ) is suppressed compared to pairing between states in the same level ( $n = n'$ ).

For interaction strengths  $\Delta > 2\hbar\omega_r$  pairing between different levels becomes relevant. At this interaction strength, the size of the Cooper pair [128]

$$\xi \equiv \frac{2\hbar p_F}{m_a \Delta}, \quad (6.23)$$

(with  $p_F = \sqrt{2m_a E_F}$ ) is smaller than the system size

$$r_F = \sqrt{\frac{2E_F}{m_a \omega_r^2}}. \quad (6.24)$$

As  $\xi$  sets the smallest length scale over which the pairing field can vary [125], the system can then be treated as locally homogeneous. In other words, for  $\Delta > 2\hbar\omega_r$ , the harmonic oscillator potential only sets the local density and the level structure can be disregarded [119, 125, 129]. In this regime, pairing is governed by the competition of  $E_F$  and  $\Delta$ , or, equivalently, by the

competition of the mean interparticle spacing

$$1/\sqrt{\rho} = \sqrt{\frac{4\pi\hbar^2}{2m_a E_F}} \quad (6.25)$$

and the coherence length  $\xi$ . The crossover from the Cooper pairing to the molecular regime occurs when  $\Delta > 2E_F$  [130]<sup>3</sup>. Here, the coherence length becomes smaller than the mean interparticle spacing, i.e. the system forms tightly bound molecules. For  $2E_F > \Delta > 2\hbar\omega_r$ , the coherence length is smaller than the system size, but larger than the interparticle spacing. The system is in the Cooper pairing regime.

The different regimes can be accessed by tuning the Fermi and binding energy, as sketched in Fig. 6.3. We approximate the strength of the pairing gap by that of the uniform 2D Fermi gas  $\Delta = \sqrt{2E_F^0 E_B}$  [130], where  $E_F^0 = (n_F + 1.5)\hbar\omega_r$  and  $E_B$  is the two-body binding energy. This overestimates the amplitude of the pairing gap in the potential-dominated regime, given by (6.21). The competition of the different energy scales is encoded in the RGB color code of the diagram, with  $(R, G, B) = (\frac{2\hbar\omega_r}{\Delta}, 1, \frac{\Delta}{2E_F^0})$ . The values are normalized to the maximum of the RGB triple. A system in the red regions of the plot is in the potential-dominated regime ( $\Delta < 2\hbar\omega_r$ ). In the blue region  $\Delta > 2E_F^0$  and the system is in the molecular regime. In the green region, the system is in the Cooper pair regime.

### 6.3.1 Observing pairing regimes

The essential task is to find an observable that allows us to distinguish between different pairing regimes. A natural observable for pairing is the two particle density-density correlator

$$\mathcal{C}^{(2)}(\boldsymbol{\chi}_\uparrow, \boldsymbol{\chi}_\downarrow) = \langle \hat{\rho}_\uparrow(\boldsymbol{\chi}_\uparrow) \hat{\rho}_\downarrow(\boldsymbol{\chi}_\downarrow) \rangle - \langle \hat{\rho}_\uparrow(\boldsymbol{\chi}_\uparrow) \rangle \langle \hat{\rho}_\downarrow(\boldsymbol{\chi}_\downarrow) \rangle, \quad (6.26)$$

where  $\boldsymbol{\chi}_\sigma$  denotes a point in space,  $\hat{\rho}_\sigma$  is the density operator and  $\langle \dots \rangle$  denotes the ground-state expectation value. The correlator gives the conditional probability of finding a spin-down atom at  $\boldsymbol{\chi}_\downarrow$ , given that there is a spin-up atom at  $\boldsymbol{\chi}_\uparrow$ . We subtract the disconnected part of the correlator, which is determined by the lower-order correlation function (i.e. the single-particle density).

#### Potential-dominated regime

In the potential-dominated regime – where pairing occurs between the time-reversed states  $|n, m\rangle$  and  $|n, -m\rangle$  – the most obvious correlation function to look at is

$$\mathcal{C}^{(2)}(m, -m) = \sum_n \langle \hat{a}_{n,m,\uparrow}^\dagger \hat{a}_{n,m,\uparrow} \hat{a}_{n,-m,\downarrow}^\dagger \hat{a}_{n,-m,\downarrow} \rangle - \langle \hat{a}_{n,m,\uparrow}^\dagger \hat{a}_{n,m,\uparrow} \rangle \langle \hat{a}_{n,-m,\downarrow}^\dagger \hat{a}_{n,-m,\downarrow} \rangle. \quad (6.27)$$

However, this correlator is experimentally inaccessible, as we – as of now – lack the ability to measure angular momenta.

<sup>3</sup>Note that this transition occurs when the interaction parameter  $\ln(k_F a_{2D}) = \ln(\sqrt{2E_F/E_B}) = 0$

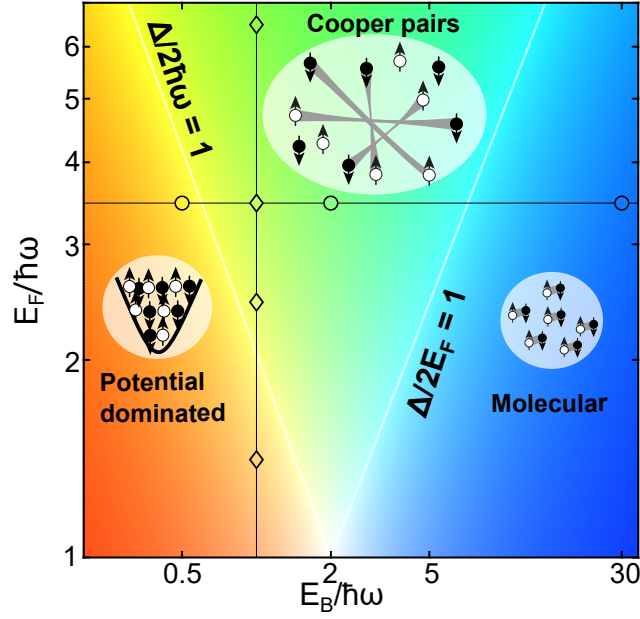


**Figure 6.3: Pairing regimes in a harmonic oscillator potential.** The competition of binding energy  $E_B$ , Fermi energy  $E_F$  and single-particle gap  $\hbar\omega_r$  give rise to three pairing regimes for fermions confined in a two-dimensional harmonic oscillator potential. When the single-particle gap exceeds the pairing gap  $\Delta = \sqrt{2E_B E_F^0}$ , pairing is dominated by the level structure of the harmonic oscillator potential. For  $\Delta > 2\hbar\omega_r$ , the level structure can be disregarded, and the system is in the Cooper pairing regime for  $2E_F > \Delta$  and in the molecular regime for  $\Delta > 2E_F$ . The three energy scales are encoded in the RGB color code  $(R, G, B) = (\frac{2\hbar\omega_r}{\Delta}, 1, \frac{\Delta}{2E_F})$ , normalized to the maximum value of the RGB triple.

Instead, we consider the correlation function in both real and momentum space. To calculate the correlator in real space, we rewrite  $v_{n,m}$  and  $u_{n,m}$  in a spatially dependent manner,

$$\begin{aligned} u_{n,m}(r, \theta) &= u_{n,m} \langle x|n, m \rangle \\ v_{n,m}(r, \theta) &= v_{n,m} \langle x|n, m \rangle \end{aligned} \quad (6.28)$$

where  $\langle x|n, m \rangle = \psi_{n,m}(r, \theta)$ , see Eq. (6.15). In real space, the density-density correlator (Eq. (6.26)) then becomes

$$\begin{aligned} \mathcal{C}^{(2)}(\mathbf{r}_\uparrow, \mathbf{r}_\downarrow) &= \left( \sum_{n,m} v_{n,m}(r_\uparrow, \theta_\uparrow) u_{n,m}(r_\downarrow, \theta_\downarrow) \right)^2 \\ &= \left( \sum_{n,m} v_{n,m} u_{n,m} R_{n,m}(r_\uparrow) R_{n,m}(r_\downarrow) \cos(m(\theta_\uparrow - \theta_\downarrow)) \right)^2. \end{aligned} \quad (6.29)$$

As pairing is local in real space, it is reasonable to simplify the four dimensional correlator  $\mathcal{C}^{(2)}(\mathbf{r}, \mathbf{r})$ , by considering only atoms that sit at the same radial and angular position ( $r$  and  $\theta$ , respectively). Due to the radial symmetry of the trap, the correlator only depends on  $r$ , consequently  $\mathcal{C}^{(2)}(r, \theta, r, \theta) \equiv \mathcal{C}^{(2)}(r, r)$  - henceforth called the *real space pair density*.

We obtain the momentum space correlator from  $v_{n,m}(p, \phi) = v_{n,m} \langle p|n, m \rangle$  (analogously for

$u_{n,m}(p, \phi)$ ) resulting in

$$\mathcal{C}^{(2)}(\mathbf{p}_\uparrow, \mathbf{p}_\downarrow) = \left( \sum_{n,m} v_{n,m} u_{n,m} R_{n,m}(p_\uparrow) R_{n,m}(p_\downarrow) \cos(m(\phi_\uparrow - \phi_\downarrow + \pi)) \right)^2. \quad (6.30)$$

In momentum space, pairing occurs between pairs of atoms of opposite momentum - as dictated by the time reversal symmetry of the paired states. Hence, we define the *momentum space pair density* as  $\mathcal{C}^{(2)}(p, \phi, p, \phi - \pi)$  - denoted as  $\mathcal{C}^{(2)}(p, -p)$ , for clarity. Following equations (6.29) and (6.30),  $\mathcal{C}^{(2)}(r, r)$  and  $\mathcal{C}^{(2)}(p, -p)$  follow the same functional form in the potential-dominated regime.

### Local density approximation

In the limit where the level structure can be disregarded, and the system can be treated as locally homogeneous, the introduction of a *local Fermi energy* is justified, replacing the global Fermi energy in the potential-dominated regime. The Fermi energy is set by the particle density  $\rho(r)$ ,

$$E_F(r) = \frac{\hbar^2}{2m_a} k_F(r)^2 = \frac{4\pi\hbar^2}{2m_a} \rho(r). \quad (6.31)$$

This allows us to define a local pairing gap  $\Delta(r) = \sqrt{2E_F(r)E_B}$ . This approximation is commonly known as the local density approximation (LDA).

For a homogeneous system, the pair density in momentum space is given by

$$\mathcal{C}^{(2)}(p, -p) = \frac{\langle \hat{a}_{p\uparrow}^\dagger \hat{a}_{p\uparrow} \hat{a}_{-p\downarrow}^\dagger \hat{a}_{-p\downarrow} \rangle}{\langle \hat{\rho}(p) \hat{\rho}(-p) \rangle} - \frac{\langle \hat{a}_{p\uparrow}^\dagger \hat{a}_{p\uparrow} \rangle \langle \hat{a}_{-p\downarrow}^\dagger \hat{a}_{-p\downarrow} \rangle}{\langle \hat{\rho}(p) \rangle \langle \hat{\rho}(-p) \rangle} = (v_p u_p)^2 = \frac{\Delta^2}{4(\epsilon_p^2 + \Delta^2)}, \quad (6.32)$$

where  $\langle \dots \rangle \equiv \langle \Psi_{\text{BCS}} | \dots | \Psi_{\text{BCS}} \rangle$  is the ground state expectation value. The momentum space correlator is connected to the real space correlator via a Fourier transform [22]

$$\mathcal{C}^{(2)}(r_\uparrow, r_\downarrow) = \left( \sum_p u_p v_p e^{ip(r_\uparrow - r_\downarrow)} \right)^2 \quad (6.33)$$

$$\stackrel{r_\downarrow = r_\uparrow}{=} \left( \sum_p u_p v_p \right)^2. \quad (6.34)$$

The pair density in real space is spatially constant, as expected for a translationally invariant system.

When the pairing gap varies locally, the real space pair density (see Eq. (6.29)) becomes spatially dependent with

$$\mathcal{C}^{(2)}(r, r) = \left( \int_{p=0}^{p_{\max}} dp \frac{\Delta(r)}{2\sqrt{\left(\frac{p^2}{2m_a} - \mu(r)\right)^2 + \Delta(r)^2}} \right)^2. \quad (6.35)$$

To obtain the pair density in momentum space, we have to consider that the momentum space measurement averages over all positions. Consequently, the momentum space correlator is

$$\mathcal{C}^{(2)}(p, -p) = \mathcal{N} \int_{r=0}^{\infty} d\mathbf{r} \frac{\rho(r)^2 \Delta(r)^2}{4 \left( \frac{p^2}{2m_a} - \mu(r) \right)^2 + \Delta(r)^2}, \quad (6.36)$$

with

$$\mathcal{N} = \frac{\left( \int_{r=0}^{\infty} d\mathbf{r} \rho(r) \right)^2}{\int_{r=0}^{\infty} d\mathbf{r} \rho(r)^2}, \quad (6.37)$$

where the contribution of each point is weighted by the local density. In the BCS limit, we can approximate the chemical potential with the Fermi energy as  $\mu \approx E_F$ . Contrary to the potential-dominated regime,  $\mathcal{C}^{(2)}(p, -p)$  and  $\mathcal{C}^{(2)}(r, r)$  do not follow the same functional form. Consequently, the pair density in real and momentum space is a good observable to distinguish between the regime where pairing is best described by time-reversed harmonic oscillator states and the regime where the discrete level structure becomes negligible, and the potential primarily sets the local density.

### Particle number conservation

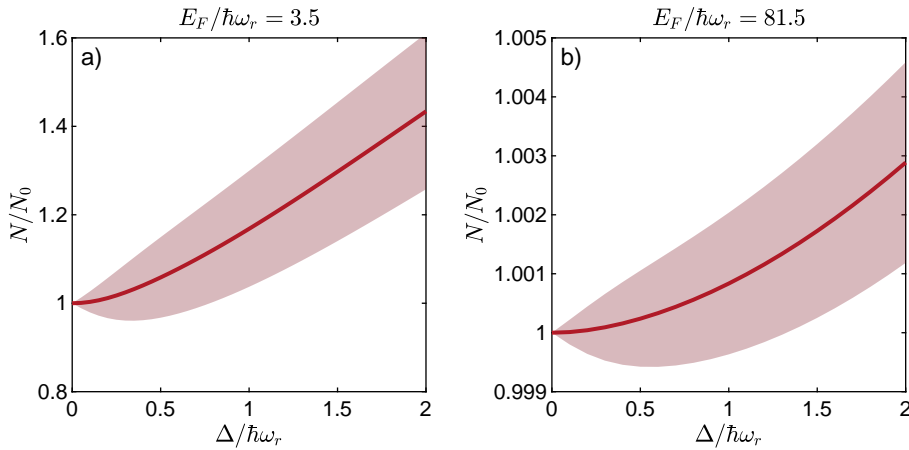


**Figure 6.4: Particle number expectation value and standard error.** Expectation value  $N$  (solid line) and standard deviation  $\Delta N$  (shaded region) of the particle number operator in BCS theory as a function of the pairing gap  $\Delta$ . To compare the relative uncertainty for two different Fermi energies –  $E_F/\hbar\omega_r = 3.5$ , a) and  $E_F/\hbar\omega_r = 81.5$ , b) – the expectation value and standard deviation are normalized to the particle number in the non-interacting limit  $N_0$ .

The theoretically calculated correlators give us a valuable intuition for the correlations expected in the different pairing regimes. However, one essential discrepancy between the theoretical calculations and the experimental result is that a mean-field approximation was used in the theoretical description. Therefore, the calculated wave functions are not an eigenstate of the particle number operator, i.e. particle number is not a conserved quantity. To understand the implications of this fact, it is instructive to consider both the expectation value of the particle number operator

$$\langle \hat{N} \rangle = \sum_{n,m} \langle \hat{a}_{n,m}^\dagger \hat{a}_{n,m} \rangle = \sum_{n,m} v_{n,m}^2 \equiv N, \quad (6.38)$$

and the particle number variance [113, 131]

$$(\Delta N)^2 \equiv \sum_{n,m} \langle \hat{a}_{n,m,\uparrow}^\dagger \hat{a}_{n,m,\uparrow} \hat{a}_{n,m,\downarrow}^\dagger \hat{a}_{n,m,\downarrow} \rangle - N^2 = \sum_{n,m} u_{n,m}^2 v_{n,m}^2. \quad (6.39)$$

Figure 6.4 shows the particle number expectation value and the variance as a function of the pairing gap for two different Fermi energies. In general, both the particle number expectation value and its uncertainty increase with increasing pairing gap. Note that the equivalent discussion also holds for the LDA regime.

The particle number uncertainty influences the correlators. When particle number is conserved, the integrals

$$N_r = \int d\mathbf{r}_\downarrow \int d\mathbf{r}_\uparrow \mathcal{C}^{(2)}(\mathbf{r}_\uparrow, \mathbf{r}_\downarrow) = 0 \quad (6.40)$$

$$N_p = \int d\mathbf{p}_\downarrow \int d\mathbf{p}_\uparrow \mathcal{C}^{(2)}(\mathbf{p}_\uparrow, \mathbf{p}_\downarrow) = 0, \quad (6.41)$$

as

$$\int d\mathbf{r}_\downarrow \int d\mathbf{r}_\uparrow \langle \hat{\rho}(\mathbf{r}_\downarrow) \hat{\rho}(\mathbf{r}_\uparrow) \rangle = \int d\mathbf{r}_\downarrow \int d\mathbf{r}_\uparrow \langle \hat{\rho}(\mathbf{r}_\uparrow) \rangle \langle \hat{\rho}(\mathbf{r}_\downarrow) \rangle = N^2, \quad (6.42)$$

(analogously in momentum space). In contrast, the correlators obtained utilizing a mean-field approximation (both in the LDA and the potential dominated regime) are strictly positive. Consequently,  $N_r > 0$  and  $N_p > 0$ . While this deviation is negligible at large  $N$ , the variance of the particle number operator is significant in the limit of few atoms. The mean-field approximation is only a good approximation in the limit of large  $N$ .

## 6.4 Experimental observation

### 6.4.1 Preparation

To experimentally realize the different pairing regimes, we prepare a system of  $N$  spin-up and  $N$  spin-down atoms (denoted as  $N + N$ ) in a closed shell ground state configuration of the 2D-OT. Altering the number of prepared atoms  $N$ , allows us to tune the Fermi energy  $E_F$ . The 2D scattering length – and thus the binding energy  $E_B$  – is controlled via the magnetic offset field, utilizing the magnetic Feshbach resonance of  ${}^6\text{Li}$  [23]. Using these two tuning knobs, we can experimentally access all three pairing regimes. To ensure that the system remains 2D, both  $E_F$  and  $E_B$  need to be smaller than  $\hbar\omega_z$ , where  $\omega_z/2\pi = 7423(3)$  Hz is the axial trap frequency of the 2D-OT. This is achieved by choosing a lower radial trap frequency in the regime of large  $E_B$  or large  $E_F$ . More details on the preparation can be found in Ch. 3.

We experimentally obtain the density-density correlator  $\mathcal{C}^{(2)}$  in real and momentum space from approximately 1000 repeated measurements of the atom positions or momenta – (see also Ch. 4). We acquire the real space pair density  $\mathcal{C}^{(2)}(r, r)$  by taking into account those pairs of spin up and spin down atoms that sit, within our resolution ( $\delta r_{\text{res}} = 300$  nm), at the same position. For the momentum space pair density  $\mathcal{C}^{(2)}(p, -p)$ , we consider those atoms that sit at opposite momenta – within our resolution  $\delta p_{\text{res}} = 0.06 p_{\text{HO}}$ . Momenta and positions are given in units of the harmonic oscillator momentum ( $p_{\text{HO}} = \sqrt{\hbar m_a \omega_r}$ ) and length ( $l_{\text{HO}} = \sqrt{\hbar/m_a \omega_r}$ ),

respectively.

## 6.4.2 Results

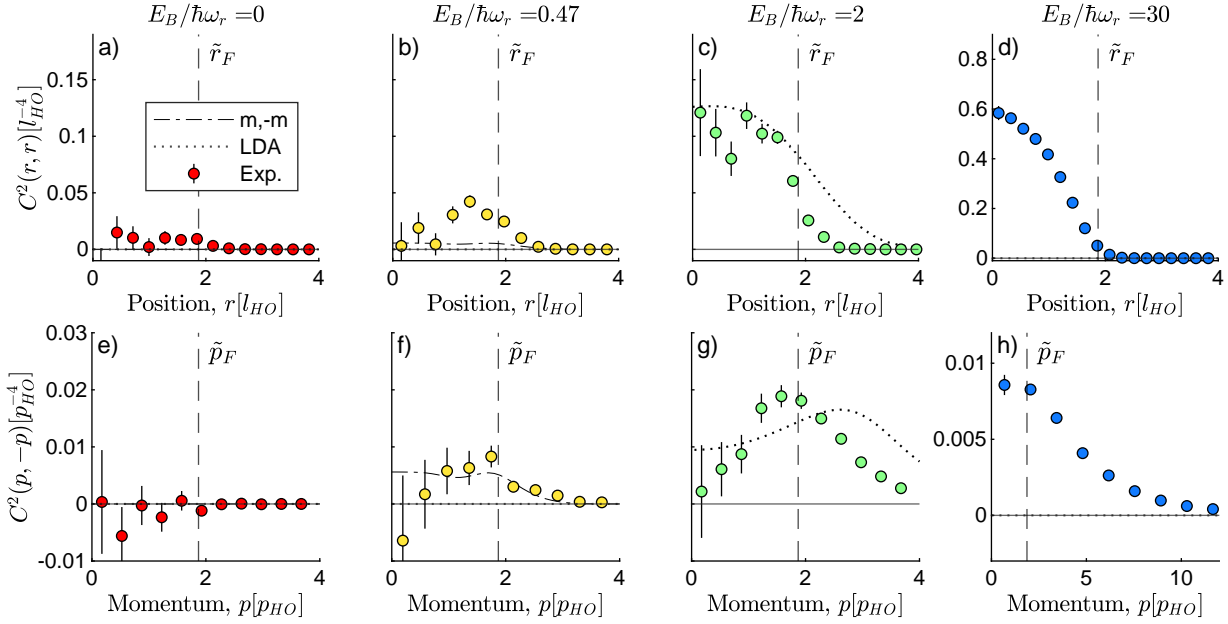


**Figure 6.5: Pair density in real and momentum space at different binding energies.** Pair densities in real (a-d) and momentum (e-h) space of 6 + 6 atoms prepared in the ground state of a 2D harmonic oscillator potential. The color of the data points encodes the relative strength of  $\Delta$ ,  $E_F$  and  $\hbar\omega_r$  via  $(R, G, B) = (\frac{2\hbar\omega_r}{\Delta}, 1, \frac{\Delta}{2E_F^0})$ , normalized to the maximum value of the RGB triple. The measured data points are compared to the pair density calculated in the LDA (dotted) and potential-dominated regime (dashed-dotted). The vertical dashed lines represent the momentum and length scale associated to the Fermi energy. Note the different scales in d and h. The error bars represent the standard errors of the mean.

In Fig. 6.5 we show the measured real (a-d) and momentum space (e-h) pair densities in a system of 6+6 atoms for different interaction strengths. The Fermi energy in the non-interacting system is  $E_F^0/\hbar\omega_r = (n_F + 1.5) = 3.5$ . For a system of 6 + 6 non-interacting atoms, the system size is  $r_F = 2.65 l_{HO}$  and the mean interparticle spacing  $1/\sqrt{\rho} = 1.34 l_{HO}$ . Note that both quantities were calculated for the non-interacting system and consequently only represent an estimate for the interacting system, used to illustrate the competition of length scales. In the weakly interacting regime ( $E_B/\hbar\omega_r = 0.47$ ), the estimated coherence length  $\xi = 2.9 l_{HO}$ , exceeds the system size, i.e.  $\xi > r_F > 1/\sqrt{\rho}$ . By increasing the binding energy  $E_B$ , we decrease the coherence length of the Cooper pair  $\xi$ , while keeping the system size  $r_F$  and mean interparticle spacing  $1/\sqrt{\rho}$  constant. We cross the diagram of Fig. 6.3 along the horizontal line.

The non-interacting system is uncorrelated in both real and momentum space. In the weakly interacting regime ( $E_B/\hbar\omega_r = 0.47$ ), pairs of opposite momentum start forming at the Fermi surface - indicated by the peak at  $\tilde{p}_F = \sqrt{m_a E_F^0}$  - the momentum associated to the Fermi energy  $E_F^0$ , assuming equipartition between kinetic and potential energy. In real space, we also observe a peak in the pair density at the surface of the trap. It lies around  $\tilde{r}_F = \sqrt{E_F^0/m_a \omega_r^2}$  - the length scale associated to the Fermi energy. Such an enhancement of pairs near the surface

has also been predicted for finite nuclei [132–134]. Qualitatively, the pair densities in real and momentum space follow the same functional form, reflecting the symmetry of the projection of the harmonic oscillator states on real and momentum space.

In the intermediate interaction strength ( $E_B/\hbar\omega_r = 2, \xi = 1.4 l_{\text{HO}}$  so  $r_F > \xi \gtrsim 1/\sqrt{\rho}$ ), the real and momentum space pair densities no longer follow the same functional form. In momentum space, the formation of pairs is limited to the Fermi surface - as expected in the Cooper pairing regime. The area below the correlation peak increases compared to the weaker binding energy, as more pairs form. In real space, pairing is no longer limited to a region around  $\tilde{r}_F$ , instead pairs form all over the system. The pair density peaks around the trap center, where the density is highest.

At a binding energy  $E_B/\hbar\omega_r = 30$  ( $\xi = 0.37 l_{\text{HO}}$ , so  $r_F > 1/\sqrt{\rho} > \xi$ ), far surpassing the Fermi energy, the momentum space pair density peaks in the center of the trap, with a width exceeding the width at lower binding energies. Here, pairing is no longer constrained to the Fermi surface and occurs all over the system in momentum space. The fermionic nature of the constituents of the pair can be disregarded, as the occupation of each state is far smaller than unity. This allows for the formation of tightly bound pairs in real space - the system is in the molecular regime. The real space pair density peaks at the trap center - molecules form all over the system.

At low interaction strengths, the pair densities in real and momentum space qualitatively follow the same functional form, as anticipated in the potential-dominated regime due to the symmetry of the projection of the state  $|n, m\rangle$  onto real and momentum space. However, there is a quantitative discrepancy between the observed pair densities in real and momentum space. The pair density in real space surpasses the pair density in momentum space by roughly one order of magnitude. The quantitative difference between real and momentum space can be understood considering that the real space pair density probes the short distance parts of the relative wave function. At very small relative distances  $\delta r$  between particles, the physics is governed by the two-body contact, and the correlation function diverges as  $\ln(\delta r)$  with  $\delta r \rightarrow 0$  in two dimensions [135]. This short distance behavior is not reproduced within BCS theory. Experimentally, the finite resolution of the matterwave magnifier introduces an effective cutoff, as atoms with very small relative position, i.e. high relative momenta are not accurately magnified. We therefore expect that the amplitude of the real space pair density is quantitatively altered by this experimental cutoff.

The pair density calculated assuming pairing between states  $|n, m\rangle$  and  $|n, -m\rangle$  does not exhibit a distinct peak at the Fermi surface, but is roughly constant for positions smaller  $\tilde{r}_F$ . The absence of a distinct peak in theory could likely stem from the fact that particle number is conserved in the experiment, but not in the theoretical calculations where  $\Delta N = 1.09$  (see Eq. (6.39)). When particle number is conserved, pair creation in higher shells has to be accompanied by hole creation in lower shells, which the theory does not account for. While a rigorous treatment is needed to quantify this effect, it provides an intuitive explanation for the expected discrepancy between experiment and theory in the occupation of low- $n$  states. This in turn leads to a discrepancy at small position or momenta, for which the contribution of these lower lying states is dominant. A more accurate description of our system could be achieved with the Hartree-Fock-Bogoliubov (HFB) theory [113], which also takes particle-hole

correlations into account. In nuclear physics, an enhanced pair density near the surface of the nucleus has been predicted by HFB theory [132–134].

Additionally, we compare the measured pair densities with the pair densities calculated within the LDA. To obtain the LDA curves with as few approximations as possible, we use the experimental measurement of the density  $\rho(r)$  as an input. In momentum space, LDA predicts a peak at finite momentum, that moves closer to the trap center with increasing interaction strength. In real space the calculated pair density peaks in the trap center, where the density and thus the gap is highest. Here we have regulated the divergence at small relative distances by setting  $p_{\max}$  in the integral of Eq. (6.35) to the momentum corresponding to the resolution of the matterwave magnifier. With this cutoff, we observe a good agreement between the measured and predicted real space pair density at a binding energy  $E_B/\hbar\omega_r = 2$ . In momentum space, the LDA curve peaks at higher momenta than the measured pair density for  $E_B/\hbar\omega_r = 2$ .

This discrepancy could stem from the fact that the local density approximation is only fully applicable when both the coherence length  $\xi$  and the mean interparticle spacing are much smaller than the system size  $r_F$ . At a binding energy of  $E_B/\hbar\omega_r = 2$ , the coherence length is  $\xi = 1.4 l_{\text{HO}}$ . While the system size ( $r_F = 2.65 l_{\text{HO}}$ ) is the leading length scale, the scales do not fully separate. Additionally, particle number is not conserved within this theory. At a binding energy  $E_B/\hbar\omega_r = 30$ , the ground state consists of tightly bound molecules. Here, the approximation  $\mu \approx E_F$ , used to simplify Equations (6.35) and (6.36) is no longer valid.

### 6.4.3 Few to many

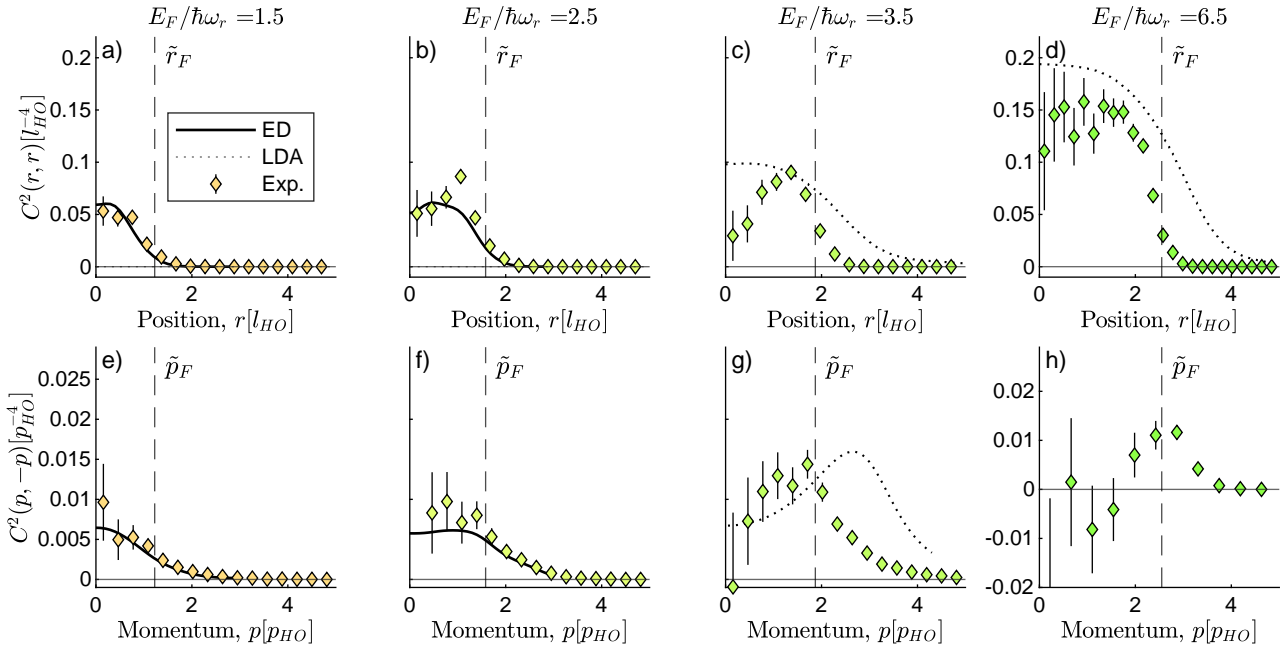


**Figure 6.6: Few to many.** Pair densities in real (a-d) and momentum space (e-h) measured in systems of different atom numbers at a constant binding energy  $E_B/\hbar\omega_r = 1$ . The measurements are compared to the pair density obtained from exact diagonalization of the many body Hamiltonian (solid curve) and LDA (dotted curve). The vertical dashed lines represent the momentum and length scale associated to the Fermi energy. Note the different scale in d) and h). The error bars represent the standard errors of the mean.

Figure 6.6 shows the measured pair density in real (a-d) and momentum (e-h) space for a system

with a binding energy of  $E_B/\hbar\omega_r = 1, \xi = 2 l_{\text{HO}}$  and different particle numbers, i.e. we cross the pairing diagram of Fig. 6.3 along the vertical line. While the estimated coherence length is constant, the system size increases with increasing Fermi energy. The mean interparticle spacing decreases with increasing Fermi energy.

Due to the small number of constituents, mean-field theories are not expected to describe our system fully. However, for systems of up to  $3 + 3$  weakly interacting fermions, it is possible to solve the  $N$ -particle Hamiltonian (6.14) by exact diagonalization [126, 136, 137]. We compare the measurements for a system of  $1 + 1$  (a, e) and  $3 + 3$  (b, f) particles –  $E_F/\hbar\omega_r = 1.5$  and  $E_F/\hbar\omega_r = 2.5$ , respectively – to the results obtained from exact diagonalization – without any free fit parameters. The measured and calculated pair densities agree quantitatively in both real and momentum space.

For  $6 + 6$  atoms ( $E_F/\hbar\omega_r = 3.5, r_F = 2.65 l_{\text{HO}}, 1/\sqrt{\rho} = 1.34 l_{\text{HO}}$ ) – Fig. 6.6(c, g) the system is expected to be in the crossover between the potential-dominated and the Cooper-pairing regime ( $r_F \gtrsim \xi > 1/\sqrt{\rho}$ ). The pair density exhibits a distinct peak in both momentum and real space, at  $\tilde{p}_F$  and  $\tilde{r}_F$ , respectively. Once again, pairs form predominantly at the surface of the trap.

For  $21 + 21$  atoms ( $E_F/\hbar\omega_r = 6.5, r_F = 3.6 l_{\text{HO}}, 1/\sqrt{\rho} = 1 l_{\text{HO}}$ ), the system size exceeds the coherence length of the Cooper pair ( $r_F > \xi > 1/\sqrt{\rho}$ ). In real space, pairs form all over the system, while in momentum space, the formation of pairs is limited to the Fermi surface. The pair density in real space is qualitatively reproduced by the LDA. In momentum space, the pair density is significantly smaller than that predicted by LDA. It is however unclear whether this difference stems from technical issues, as the momentum space density is significantly higher than for measurements with smaller atom numbers. This increases the probability of two atoms in close proximity, which are undetected by our current atom identification regime. A viable option that is currently explored is to utilize machine learning techniques [138], allowing to accurately reconstruct the atomic positions in dense samples.

## 6.5 Conclusion and Outlook

In conclusion, we have observed the influence of the confining potential on pairing correlations. When the coherence length of the pair is smaller than the system size, i.e. in the regime of weak interactions and intermediate particle number, we observe a real space pair density that is peaked not at the trap center – where the density is highest – but near the surface of the system. Such a surface enhancement of pair correlations has also been predicted for finite nuclei [132–134]. As the coherence length becomes smaller than the system size, i.e. as the interactions or the particle number are increased, the real space pair density is peaked in the center of the trap. In momentum space, the pair density is peaked at finite momenta, as is expected for Cooper pairs. At very large interaction strengths (when the coherence length becomes smaller than the mean interparticle spacing) the momentum space pair density peaks in the center of the trap, showcasing the formation of tightly bound molecules.

By accessing both real and momentum space correlations, we can distinguish between the regime of weak interactions – where pairing is best described by time-reversed single-particle states – and stronger interactions, where the discrete level structure can be disregarded and

the potential only sets the local density. While comparisons to many-body theory provide a qualitative understanding of the observed behavior, they fail to fully capture our experimental results due to the small number of constituents. However, exact diagonalization methods reveal excellent agreement with our experimental observations.

For atom numbers larger than three atoms per spin state, our system enters a regime that lies beyond the reach of both many-body theories and exact solutions. The high degree of experimental control, combined with the accurate correspondence to exact solutions at lower atom numbers, showcases the possibility of using our system as a quantum emulator for other finite quantum systems that are not well described by both few and many body theories. These include nuclei, small superconducting grains, nanotubes, and quantum dots.

In nuclear physics, a vast number of approaches to the pairing problem exist. These include different particle number projection techniques [139], iterative approaches and artificial neural networks [140]. While our system by no means represents an accurate model of the nucleus, it can potentially be used as a simplified toy model with known shell structure. Ideally, one can benchmark theories employing e.g. different particle number projection techniques with our experimental observations to see whether they accurately capture the properties of our system before expanding them to a more complicated regime where also the nuclear mean-field has to be taken into account. To achieve this, both the experimental effort and the clear interpretation of the results would be highly facilitated by a measurement scheme allowing us to measure in an angular momentum basis.

# 7 | Summary and Outlook

So long, and thanks for all the fish.

---

DOUGLAS ADAMS

*The Hitchhiker's Guide to the Galaxy, 1979*

In this thesis, we discuss quantum emulation of two different types of collective behavior with a system of few fermionic  ${}^6\text{Li}$  atoms. Motivated by high energy nuclear collisions, we explored the emergence of interaction-driven elliptic flow. Inspired by nuclear physics, we investigated the influence of broken translational symmetry on the formation of pairs. Our system provides a high degree of control in combination with single particle resolved observables that remain elusive in both high-energy and nuclear physics, allowing us to explore the essential mechanism giving rise to these collective phenomena.

To explore collectivity in our system, we implemented a new experimental tool – the matterwave magnifier. Magnifying the initial wave function by a factor of 56 allows us to access real space observables – originally obfuscated by the resolution of the detection technique – with single-atom and spin resolution. We benchmark the performance of the matterwave magnifier by imaging systems with known wave functions.

Motivated by observations of collective behavior in proton-proton collisions, we investigate the emergence of elliptic flow in a mesoscopic Fermi gas. Our measurements in real and momentum space reveal interaction-driven elliptic flow with as few as three particles per spin-state. By comparing the interacting expansion of 5+5 atoms with both a hydrodynamic and a collisional point-particle model, we can see that the observed inversion of the aspect ratio is best captured by a hydrodynamic theory – despite the fact that the separation of scales required for a collisional hydrodynamic behavior is not present in our system. These observations warrant an exploration of the connection between the observed collective flow and the emergence of superfluidity.

Inspired by the formation of pairs in systems with broken translational symmetry, such as nuclei or 'dirty' superconductors, we explore the influence of a spatially varying potential on the formation of pairs. The formation of pairs in systems with broken translational symmetry is not captured by standard BCS theory. It requires an extended framework – introduced by Anderson [107] – where pairs form between time-reversed states. Altering the interaction strength or particle number we observe how the system transitions from a regime where pairing is dominated by the discrete shell structure of the confining potential to a regime where the potential only sets the local density, bridging the gap between the Cooper picture and the more generalized Anderson framework. We can distinguish different pairing regimes by the pair density in real and momentum space. In the regime of weak interactions, we observe that the formation of pairs is limited to the outer regions of the system. This behavior is not captured by mean-field theories, but has been predicted for finite nuclei. This showcases how quantum

---

emulation in the mesoscopic regime can shed light on finite quantum systems that are not well described by many-body theories and inaccessible to exact methods.

Based on the measurements described in this thesis, we discuss three exemplary follow-up questions and how they could be tackled experimentally:

### **Is pairing a necessary criterion for elliptic flow in our system?**

As discussed in Sec. 5.5.1, a tempting explanation for the observed elliptic flow is that our system behaves as a superfluid. Even though the interacting expansion does not allow the distinction between a collisional and a superfluid hydrodynamic description, it is fascinating to explore whether the formation of pairs – a necessary criterion for superfluidity in fermionic systems – is also a necessary criterion for elliptic flow in our system. To test this, we could study the expansion of a spin-imbalanced system, i.e. a system with an unequal number of spin-up and spin-down atoms. Preparing the system in a regime where we expect interaction-driven elliptic flow for the spin state with smaller atom number (the minority) would allow us to explore the role of pairing by studying the behavior of the majority. If pair creation is not a necessary condition for elliptic flow, the majority should invert its aspect ratio after a long interacting expansion time. However, if pair creation is a necessary condition, we expect that the inversion of the aspect ratio exhibited by the paired atoms is masked by ballistic expansion of the unpaired atoms (leading to an isotropic distribution). Ideally, the final density then shows a bimodal distribution consisting of an elliptic density profile of the paired atoms in the center and an isotropic density profile of the unpaired atoms.

### **What is the influence of broken time reversal symmetry on the formation of pairs?**

An interesting future endeavor is to study the break-down of pairing in a system where time reversal symmetry is broken. Following the discussion in Sec. 6.2.1, time reversal symmetry can be broken by a rotation of the confining potential. This rotation lifts the degeneracy of the time reversed states in the non-rotating system - thus, at a given interaction strength, pairing is suppressed above a critical rotation frequency. Experimentally, this can be explored by studying pair correlations of atoms in a rotating harmonic oscillator potential - a system that has already been realized in our group [123, 141, 142]. In such a system one could then also characterize a Yrast spectrum for a rotating, mesoscopic Fermi gas, closely following suggestions in [121]. Here, we could also investigate the back-bending of the Yrast line due to pair breaking.

### **Are the observed pairs phase coherent?**

Long-range phase coherence is a defining characteristic of Bose-Einstein condensates and a necessary condition for superfluidity. To explore whether phase coherence is established as soon as pairs form is therefore a highly intriguing question, both in the few- and many-body limit [143, 144]. Naively one would expect that when the coherence length of the Cooper pair is larger than the system, phase fluctuations are negligible, and phase coherence is established as soon as pairs form. To test this hypothesis experimentally, we could utilize phase microscopy techniques [145–147] to explore phase coherence. These phase microscopy techniques map phase fluctuations on density fluctuations. Analogously to optical phase contrast imaging [148, 149], such a mapping can be achieved by imprinting a known phase shift on the zero momentum

component of the wave function. When measuring the real space density, the zero momentum component interferes with the non-zero momentum components, mapping phase fluctuations onto density fluctuations. To achieve this phase-shift, Brueggjenjuergen et al. [146] cleverly use the naturally occurring aberrations of the matterwave magnifier, an approach that could potentially also be easily implemented in our experimental setup.



# Bibliography<sup>1</sup>

- [1] T. Harford, *How a mind-boggling device changed economic history*, Accessed: 2025-03-24, (2024) <https://www.ft.com/content/6f28a534-7eae-4762-9ab9-abef0ff00525>.
- [2] C. Bissell, “Historical perspectives - The Moniac A Hydromechanical Analog Computer of the 1950s”, *IEEE Control Systems* **27**, 69 (2007).
- [3] R. P. Feynman, “Simulating physics with computers”, *International Journal of Theoretical Physics* **21**, 467 (1982).
- [4] D. Hangleiter, J. Carolan, and K. P. Y. Thébault, *Analogue Quantum Simulation: A New Instrument for Scientific Understanding* (Springer International Publishing, 2022).
- [5] J. Hubbard, “Electron correlations in narrow energy bands”, *Proceedings of the Royal Society of London. Series A. Mathematical and Physical Sciences* **276**, 238 (1963).
- [6] D. Jaksch, C. Bruder, J. I. Cirac, C. W. Gardiner, and P. Zoller, “Cold Bosonic Atoms in Optical Lattices”, *Physical Review Letters* **81**, 3108 (1998).
- [7] M. Greiner, O. Mandel, T. Esslinger, T. W. Hänsch, and I. Bloch, “Quantum phase transition from a superfluid to a Mott insulator in a gas of ultracold atoms”, *Nature* **415**, 39 (2002).
- [8] C. Viermann et al., “Quantum field simulator for dynamics in curved spacetime”, *Nature* **611**, 260 (2022).
- [9] D. N. Biggerstaff, R. Heilmann, A. A. Zecevik, M. Gräfe, M. A. Broome, A. Fedrizzi, S. Nolte, A. Szameit, A. G. White, and I. Kassal, “Enhancing coherent transport in a photonic network using controllable decoherence”, *Nature Communications* **7**, 10 . 1038/ncomms11282 (2016).
- [10] A. Aspuru-Guzik and P. Walther, “Photonic quantum simulators”, *Nature Physics* **8**, 285 (2012).
- [11] M. H. Anderson, J. R. Ensher, M. R. Matthews, C. E. Wieman, and E. A. Cornell, “Observation of Bose-Einstein Condensation in a Dilute Atomic Vapor”, *Science* **269**, 198 (1995).
- [12] K. Aikawa, A. Frisch, M. Mark, S. Baier, A. Rietzler, R. Grimm, and F. Ferlaino, “Bose-Einstein Condensation of Erbium”, *Physical Review Letters* **108**, 210401 (2012).
- [13] M. Lu, N. Q. Burdick, S. H. Youn, and B. L. Lev, “Strongly Dipolar Bose-Einstein Condensate of Dysprosium”, *Physical Review Letters* **107**, 190401 (2011).
- [14] N. Bigagli, W. Yuan, S. Zhang, B. Bulatovic, T. Karman, I. Stevenson, and S. Will, “Observation of Bose-Einstein condensation of dipolar molecules”, *Nature* **631**, 289 (2024).
- [15] A. Schindewolf, R. Bause, X.-Y. Chen, M. Duda, T. Karman, I. Bloch, and X.-Y. Luo, “Evaporation of microwave-shielded polar molecules to quantum degeneracy”, *Nature* **607**, 677 (2022).

---

<sup>1</sup>If you're ready to activate hard mode, read only this chapter. The rest of the thesis is left as an exercise to the reader.

- [16] A. Mazurenko, C. S. Chiu, G. Ji, M. F. Parsons, M. Kanász-Nagy, R. Schmidt, F. Grusdt, E. Demler, D. Greif, and M. Greiner, “A cold-atom Fermi–Hubbard antiferromagnet”, *Nature* **545**, 462 (2017).
- [17] J. Koepsell et al., “Microscopic evolution of doped Mott insulators from polaronic metal to Fermi liquid”, *Science* **374**, 82 (2021).
- [18] V. Helson, T. Zwettler, F. Mivehvar, E. Colella, K. Roux, H. Konishi, H. Ritsch, and J.-P. Brantut, “Density-wave ordering in a unitary Fermi gas with photon-mediated interactions”, *Nature* **618**, 716 (2023).
- [19] M. E. Gehm, “Properties of  $^6\text{Li}$ ”, in (2003).
- [20] J. Walraven, “Quantum Gases”, in Lecture notes, university of amsterdam (2019).
- [21] J. Dalibard, “Collisional dynamics of ultra-cold atomic gases”, *Proceedings of the International School of Physics* **140**, 321 (1999).
- [22] W. Ketterle and M. W. Zwierlein, “Making, probing and understanding ultracold Fermi gases”, *Riv. Nuovo Cimento* (3) **31**, 247 (2008).
- [23] G. Zuern, T. Lompe, A. N. Wenz, S. Jochim, P. S. Julienne, and J. M. Hutson, “Precise Characterization of  $\text{Li}_6$  Feshbach Resonances Using Trap-Sideband-Resolved RF Spectroscopy of Weakly Bound Molecules”, *Phys. Rev. Lett.* **110**, 135301 (2013), ppublish.
- [24] J. J. Sakurai, *Modern Quantum Mechanics*, edited by J. Napolitano, 3rd ed., Description based on publisher supplied metadata and other sources. (Cambridge University Press, Cambridge, 1985), 1572 pp.
- [25] T. Gould and T. Bučko, “ $C_6$  Coefficients and Dipole Polarizabilities for All Atoms and Many Ions in Rows 1–6 of the Periodic Table”, *Journal of Chemical Theory and Computation* **12**, 3603 (2016).
- [26] J. Levinsen and M. M. Parish, “Strongly interacting two-dimensional Fermi gases”, **3**, 1 (2014), arXiv:1408.2737 [cond-mat.quant-gas].
- [27] S. K. Adhikari, “Quantum scattering in two dimensions”, *Am. J. Phys.* **54**, 362 (1986).
- [28] D. S. Petrov and G. V. Shlyapnikov, “Interatomic collisions in a tightly confined Bose gas”, *Physical Review A* **64**, 012706 (2001).
- [29] C. Chin, R. Grimm, P. Julienne, and E. Tiesinga, “Feshbach resonances in ultracold gases”, *Reviews of Modern Physics* **82**, 1225 (2010).
- [30] A. J. Moerdijk, B. J. Verhaar, and A. Axelsson, “Resonances in ultracold collisions of  $\text{Li}_6$ ,  $\text{Li}_7$ , and  $\text{Na}_3$ ”, *Physical Review A* **51**, 4852 (1995).
- [31] R. Grimm, M. Weidemüller, and Y. B. Ovchinnikov, “Optical Dipole Traps for Neutral Atoms”, in *Advances in atomic, molecular, and optical physics* (Elsevier, 2000), pp. 95–170.
- [32] L. Bayha, “Emergence of Many-Body Physics in Two-Dimensional Few-Fermion Systems”, PhD thesis (Heidelberg University, 2020).
- [33] M. Holten, “From Pauli Blocking to Cooper Pairs: Emergence in a Mesoscopic 2D Fermi Gas”, PhD thesis (Heidelberg University, 2022).
- [34] M. G. Ries, “A Two-Dimensional Fermi Gas in the BEC-BCS Crossover”, PhD thesis (Heidelberg University, 2015).
- [35] A. Bergschneider, “Strong correlations in few-fermion systems”, PhD thesis (Heidelberg University, 2017).
- [36] J. H. W. Becher, “Towards Spin and Site-Resolved, Single-Atom Imaging of  $^6\text{Li}$  Atoms in a Multiwell Potential”, MA thesis (Heidelberg University, 2016).

- [37] V. M. Klinkhamer, “Few Fermion Systems under a matterwave microscope”, PhD thesis (Heidelberg University, 2018).
- [38] W. D. Phillips and H. Metcalf, “Laser Deceleration of an Atomic Beam”, *Phys. Rev. Lett.* **48**, 596 (1982).
- [39] J. V. Prodan, W. D. Phillips, and H. Metcalf, “Laser Production of a Very Slow Monoenergetic Atomic Beam”, *Phys. Rev. Lett.* **49**, 1149 (1982).
- [40] T. E. Barrett, S. W. Dapore-Schwartz, M. D. Ray, and G. P. Lafyatis, “Slowing atoms with  $\sigma$ -polarized light”, *Phys. Rev. Lett.* **67**, 3483 (1991).
- [41] V. Bagnato, A. Aspect, and S. Zilio, “Study of laser deceleration of an atomic beam by monitoring the fluorescence along the deceleration path”, *Opt. Commun.* **72**, 76 (1989).
- [42] J. Dalibard and C. Cohen-Tannoudji, “Laser cooling and trapping of neutral atoms”, in (1992).
- [43] S. Chu, L. Hollberg, J. E. Bjorkholm, A. Cable, and A. Ashkin, “Three-dimensional viscous confinement and cooling of atoms by resonance radiation pressure”, *Phys. Rev. Lett.* **55**, 48 (1985).
- [44] C. Cohen-Tannoudji and D. Guéry-Odelin, *Advances in Atomic Physics: An Overview* (WORLD SCIENTIFIC, Sept. 2011).
- [45] P. Simon, “Apparatus for the preparation of ultracold Fermi gases”, MA thesis (Heidelberg University, 2010).
- [46] F. Serwane, “Deterministic Preparation of a Tunable Few-Fermion System”, PhD thesis (Heidelberg University, 2011).
- [47] F. Serwane, G. Zurn, T. Lompe, T. B. Ottenstein, A. N. Wenz, and S. Jochim, “Deterministic Preparation of a Tunable Few-Fermion System”, *Science* **332**, 336 (2011).
- [42] D. Adams, *The hitchhiker’s guide to the galaxy*, 1. American ed (Harmony Books, New York, 1980), 215 pp.
- [48] A. Bergschneider, V. M. Klinkhamer, J. H. Becher, R. Klemt, G. Zuern, P. M. Preiss, and S. Jochim, “Spin-resolved single-atom imaging of Li6 in free space”, *Phys. Rev. A* **97**, 063613 (2018).
- [49] R. Buecker, A. Perrin, S. Manz, T. Betz, C. Koller, T. Plisson, J. Rottmann, T. Schumm, and J. Schmiedmayer, “Single-particle-sensitive imaging of freely propagating ultracold atoms”, *New J. Phys.* **11**, 103039 (2009).
- [50] L. Su, A. Douglas, M. Szurek, A. H. Hebert, A. Krahn, R. Groth, G. A. Phelps, O. Markovic, and M. Greiner, *Fast single atom imaging in optical lattice arrays*, 2024, [arXiv:2404.09978 \[cond-mat.quant-gas\]](https://arxiv.org/abs/2404.09978).
- [51] L. Asteria, H. P. Zahn, M. N. Kosch, K. Sengstock, and C. Weitenberg, “Quantum gas magnifier for sub-lattice-resolved imaging of 3D quantum systems”, *Nature* **599**, 571 (2021).
- [52] L. Su, A. Douglas, M. Szurek, A. H. Hébert, A. Krahn, R. Groth, G. A. Phelps, O. Marković, and M. Greiner, “Fast single atom imaging for optical lattice arrays”, *Nature Communications* **16**, 10.1038/s41467-025-56305-y (2025).
- [53] T. Markus, “The phase-space approach to optical system theory”, *Opt. Photonics Lett.*, 1330001 (2013).
- [54] A. W. Paeth, “A fast algorithm for general raster rotation”, *Graphics Gems*, 179 (1990).

- [55] P. Murthy, D. Kedar, T. Lompe, M. Neidig, M. Ries, A. Wenz, G. Zürn, and S. Jochim, “Matter-wave fourier optics with a strongly interacting two-dimensional fermi gas”, *Phys. Rev. A* **90**, 043611 (2014).
- [56] E. R. I. Abraham, W. I. McAlexander, J. M. Gerton, R. G. Hulet, R. Côté, and A. Dalgarno, “Singlet  $s$ -wave scattering lengths of  ${}^6\text{Li}$  and  ${}^7\text{Li}$ ”, *Phys. Rev. A* **53**, R3713 (1996).
- [57] N. Abbas, “Raman Transitions with a Phase Locked Laser System”, MA thesis (Heidelberg University, 2021).
- [58] I. Shvarchuck, C. Buggle, D. Petrov, K. Dieckmann, M. Zielonkowski, M. Kemmann, T. Tiecke, W. Von Klitzing, G. Shlyapnikov, and J. Walraven, “Bose-einstein condensation into nonequilibrium states studied by condensate focusing”, *Phys. Rev. Lett.* **89**, 270404 (2002).
- [59] S. Tung, G. Lamporesi, D. Lobser, L. Xia, and E. A. Cornell, “Observation of the presuperfluid regime in a two-dimensional Bose gas”, *Phys. Rev. Lett.* **105**, 230408 (2010).
- [60] Z. Idziaszek and T. Calarco, “Analytical solutions for the dynamics of two trapped interacting ultracold atoms”, *Phys. Rev. A* **74**, 022712 (2006).
- [61] M. Vogelsberger, S. Genel, V. Springel, P. Torrey, D. Sijacki, D. Xu, G. Snyder, S. Bird, D. Nelson, and L. Hernquist, “Properties of galaxies reproduced by a hydrodynamic simulation”, *Nature* **509**, 177 (2014).
- [62] B. Mottelson, “Elementary modes of excitation in the nucleus.”, [10.1103/REVMODPHYS.48.375](https://arxiv.org/abs/10.1103/REVMODPHYS.48.375) (1976).
- [63] J. S. Guasto, R. Rusconi, and R. Stocker, “Fluid Mechanics of Planktonic Microorganisms”, *Annual Review of Fluid Mechanics* **44**, 373 (2012).
- [64] L. Landau and E. Lifshitz, *Fluid mechanics* (Pergamon Press, 1987).
- [65] P. Braun-Munzinger and J. Stachel, “The quest for the quark-gluon plasma”, *Nature* **448**, 302 (2007).
- [66] S. Z. Belen’kji and L. D. Landau, “Hydrodynamic theory of multiple production of particles”, *Il Nuovo Cimento* **3**, 15 (1956).
- [67] J.-Y. Ollitrault, “Anisotropy as a signature of transverse collective flow”, *Phys. Rev. D* **46**, 229 (1992).
- [68] V. Khachatryan et al. (CMS), “Observation of Long-Range Near-Side Angular Correlations in Proton-Proton Collisions at the LHC”, *JHEP* **09**, 091 (2010), [arXiv:1009.4122](https://arxiv.org/abs/1009.4122) [[hep-ex](https://arxiv.org/abs/hep-ex)].
- [69] B. Schenke, “The smallest fluid on Earth”, *Rept. Prog. Phys.* **84**, 082301 (2021), [arXiv:2102.11189](https://arxiv.org/abs/2102.11189) [[nuc1-th](https://arxiv.org/abs/nuc1-th)].
- [70] J. L. Nagle and W. A. Zajc, “Small System Collectivity in Relativistic Hadronic and Nuclear Collisions”, *Ann. Rev. Nucl. Part. Sci.* **68**, 211 (2018), [arXiv:1801.03477](https://arxiv.org/abs/1801.03477) [[nuc1-ex](https://arxiv.org/abs/nuc1-ex)].
- [71] K. Adcox et al., “Formation of dense partonic matter in relativistic nucleus–nucleus collisions at RHIC: Experimental evaluation by the PHENIX Collaboration”, *Nucl. Phys. A* **757**, 184 (2005).
- [72] J. Adams et al., “Experimental and theoretical challenges in the search for the quark–gluon plasma: The STAR Collaboration’s critical assessment of the evidence from RHIC collisions”, *Nucl. Phys. A* **757**, 102 (2005).

- [73] I. Arsene et al., “Quark–gluon plasma and color glass condensate at RHIC? The perspective from the BRAHMS experiment”, *Nucl. Phys. A* **757**, 1 (2005).
- [74] B. Back et al., “The PHOBOS perspective on discoveries at RHIC”, *Nucl. Phys. A* **757**, 28 (2005).
- [75] Y. Aoki, Z. Fodor, S. Katz, and K. Szabó, “The QCD transition temperature: Results with physical masses in the continuum limit”, *Phys. Lett. B* **643**, 46 (2006).
- [76] C. Shen, U. Heinz, P. Huovinen, and H. Song, “Radial and elliptic flow in Pb+Pb collisions at energies available at the CERN Large Hadron Collider from viscous hydrodynamics”, *Phys. Rev. C* **84**, 044903 (2011).
- [77] A. Adare et al., “Measurement of Long-Range Angular Correlation and Quadrupole Anisotropy of Pions and (Anti)Protons in Central d+Au Collisions at sNN=200GeV”, *Phys. Rev. Lett.* **114**, 192301 (2015).
- [78] A. Adare et al., “Measurements of Elliptic and Triangular Flow in High-Multiplicity He3+Au Collisions at sNN=200 GeV”, *Phys. Rev. Lett.* **115**, 142301 (2015).
- [79] C. Aidala et al., “Measurement of long-range angular correlations and azimuthal anisotropies in high-multiplicity p+Au collisions at sNN=200 GeV”, *Phys. Rev. C* **95**, 034910 (2017).
- [80] J. L. Nagle, A. Adare, S. Beckman, T. Koblesky, J. O. Koop, D. McGlinchey, P. Romatschke, J. Carlson, J. E. Lynn, and M. McCumber, “Exploiting Intrinsic Triangular Geometry in Relativistic He3+Au Collisions to Disentangle Medium Properties”, *Phys. Rev. Lett.* **113**, 112301 (2014).
- [81] G. Aad et al., “Observation of Long-Range Elliptic Azimuthal Anisotropies in  $\sqrt{s}=13$  and 2.76 TeV pp Collisions with the ATLAS Detector”, *Phys. Rev. Lett.* **116**, 172301 (2016).
- [82] V. Khachatryan et al., “Evidence for collectivity in pp collisions at the LHC”, *Phys. Lett. B* **765**, 193 (2017).
- [83] K. M. O’Hara, S. L. Hemmer, M. E. Gehm, S. R. Granade, and J. E. Thomas, “Observation of a Strongly Interacting Degenerate Fermi Gas of Atoms”, *Science* **298**, 2179 (2002).
- [84] K. B. Davis, M. R. Andrews, N. J. van Druten, D. S. Durfee, D. M. Kurn, and W. Ketterle, “Bose-Einstein Condensation in a Gas of Sodium Atoms”, *Phys. Rev. Lett.* **75**, 3969 (1995).
- [85] A. Trenkwalder, C. Kohstall, M. Zaccanti, D. Naik, A. I. Sidorov, F. Schreck, and R. Grimm, “Hydrodynamic Expansion of a Strongly Interacting Fermi-Fermi Mixture”, *Phys. Rev. Lett.* **106**, 115304 (2011).
- [86] R. J. Fletcher, J. Man, R. Lopes, P. Christodoulou, J. Schmitt, M. Sohmen, N. Navon, R. P. Smith, and Z. Hadzibabic, “Elliptic flow in a strongly interacting normal Bose gas”, *Phys. Rev. A* **98**, 011601, 011601 (2018), arXiv:1803.06338 [cond-mat.quant-gas].
- [87] L. Pitaevskii and S. Stringari, *Bose-Einstein Condensation and Superfluidity*, International Series of Monographs on Physics Ser. v.164 (Oxford University Press, Incorporated, Oxford, 2016), 1567 pp.
- [88] A. Harpole, M. Zingale, I. Hawke, and T. Chegini, “Pyro: a framework for hydrodynamics explorations and prototyping”, *Journal of Open Source Software* **4**, 1265 (2019).
- [89] V. Makhalov, K. Martiyanov, and A. Turlapov, “Ground-State Pressure of Quasi-2D Fermi and Bose Gases”, *Phys. Rev. Lett.* **112**, 045301, 045301 (2014), arXiv:1305.4411 [cond-mat.quant-gas].

- [90] D. Hilbert, “Mathematical problems”, *Bulletin of the American Mathematical Society* **8**, 437 (1902).
- [91] Y. Deng, Z. Hani, and X. Ma, “Long time derivation of the boltzmann equation from hard sphere dynamics”, [10.48550/ARXIV.2408.07818](https://arxiv.org/abs/2408.07818) (2024), arXiv:2408.07818 [math.AP].
- [92] Y. Deng, Z. Hani, and X. Ma, “Hilbert’s sixth problem: derivation of fluid equations via boltzmann’s kinetic theory”, [10.48550/ARXIV.2503.01800](https://arxiv.org/abs/2503.01800) (2025), arXiv:2503.01800 [math.AP].
- [93] C. Menotti, P. Pedri, and S. Stringari, “Expansion of an Interacting Fermi Gas”, *Phys. Rev. Lett.* **89**, 250402 (2002).
- [94] A. A. Vlasov, “The vibrational properties of an electron gas”, *Uspekhi Fizicheskikh Nauk* (1967).
- [95] D. Guéry-Odelin, “Mean-field effects in a trapped gas”, *Phys. Rev. A* **66**, 033613 (2002).
- [96] A. J. Leggett, *Quantum liquids, Bose condensation and cooper pairing in condensed-matter systems*, First published in paperback, Oxford Graduate texts (Oxford University Press, Oxford, 2022), 388 pp.
- [97] O. Penrose and L. Onsager, “Bose-Einstein Condensation and Liquid Helium”, *Phys. Rev.* **104**, 576 (1956).
- [98] C. N. Yang, “Concept of off-diagonal long-range order and the quantum phases of liquid He and of superconductors”, *Rev. Mod. Phys.* **34**, 694 (1962).
- [99] E. Madelung, “Eine anschauliche Deutung der Gleichung von Schroedinger”, *Die Naturwissenschaften* **14**, 1004 (1926).
- [100] E. Madelung, “Quantentheorie in hydrodynamischer Form”, *Zeitschrift fuer Physik* **40**, 322 (1927).
- [101] M. W. Zwierlein, J. R. Abo-Shaeer, A. Schirotzek, C. H. Schunck, and W. Ketterle, “Vortices and superfluidity in a strongly interacting Fermi gas”, *Nature* **435**, 1047 (2005).
- [102] L. Sobirey, N. Luick, M. Bohlen, H. Biss, H. Moritz, and T. Lompe, “Observation of superfluidity in a strongly correlated two-dimensional Fermi gas”, *Science* **372**, 844 (2021), ppublish.
- [103] S. Grebenev, J. P. Toennies, and A. F. Vilesov, “Superfluidity Within a Small Helium-4 Cluster: The Microscopic Andronikashvili Experiment”, *Science* **279**, 2083 (1998).
- [104] P. Sindzingre, D. M. Ceperley, and M. L. Klein, “Superfluidity in clusters of p-H<sub>2</sub> molecules”, *Phys. Rev. Lett.* **67**, 1871 (1991).
- [105] L. N. Cooper, “Bound Electron Pairs in a Degenerate Fermi Gas”, *Phys. Rev.* **104**, 1189 (1956).
- [106] J. Bardeen, L. N. Cooper, and J. R. Schrieffer, “Theory of superconductivity”, *Phys. Rev.* **108**, 1175 (1957).
- [107] P. Anderson, “Theory of dirty superconductors”, *J. Phys. Chem. Solids* **11**, 26 (1959).
- [108] S. a. Belyaev, *Effect of pairing correlations on nuclear properties*, Matematisk-fysiske meddelelser ; bind 31, nr. 11. 840792891 (Det Kongelige Danske Videnskabernes Selskab Naturvidenskabelig og Matematisk Afdeling., København, 1959).
- [109] D. M. Brink and R. A. Broglia, *Nuclear Superfluidity: Pairing in Finite Systems* (Cambridge University Press, July 2005).
- [110] P. Coleman, *Introduction to Many-Body Physics* (Cambridge University Press, Nov. 2015).

- [111] A. Altland and B. D. Simons, *Condensed Matter Field Theory* (Cambridge University Press, Mar. 2010).
- [112] N. N. Bogoljubov, V. V. Tolmachov, and D. V. Širkov, “A New Method in the Theory of Superconductivity”, *Fortschr. Phys.* **6**, 605 (1958).
- [113] P. Ring and P. H. Schuck, *The nuclear many-body problem*, Texts and Monographs in Physics (Springer, Berlin, Germany, May 2000).
- [114] P. Lee, in *Theory of solids—mit course no. 8.512*, MIT OpenCourseWare (Cambridge MA, 2009).
- [115] B. H. Bransden and C. J. Joachain, *Quantum mechanics*, 2. ed., [repr.] (Pearson/Prentice Hall, Harlow, 2007), 803 pp.
- [116] O. Haxel, J. H. D. Jensen, and H. E. Suess, “On the ‘Magic Numbers’ in Nuclear Structure”, *Phys. Rev.* **75**, 1766 (1949).
- [117] M. G. Mayer, “On Closed Shells in Nuclei”, *Phys. Rev.* **74**, 235 (1948).
- [118] A. Bohr, B. R. Mottelson, and D. Pines, “Possible Analogy between the Excitation Spectra of Nuclei and Those of the Superconducting Metallic State”, *Phys. Rev.* **110**, 936 (1958).
- [119] H. Heiselberg, “Pairing of fermions in atomic traps and nuclei”, *Phys. Rev. A* **68**, 053616 (2003).
- [120] B. R. Mottelson and J. G. Valatin, “Effect of Nuclear Rotation on the Pairing Correlation”, *Phys. Rev. Lett.* **5**, 511 (1960).
- [121] B. Mottelson, “Yrast Spectra of Weakly Interacting Bose-Einstein Condensates”, *Phys. Rev. Lett.* **83**, 2695 (1999).
- [122] R. Wyss and M. A. Riley, “Fifty Years of Backbending”, *Nuclear Physics News* **32**, 16 (2022).
- [123] P. Lunt, “Rotating few-fermion systems”, PhD thesis (Heidelberg University, 2024).
- [124] G. M. Bruun, “Long-lived Higgs mode in a two-dimensional confined Fermi system”, *Phys. Rev. A* **90**, 023621 (2014).
- [125] H. Heiselberg and B. Mottelson, “Shell Structure and Pairing for Interacting Fermions in a Trap”, *Phys. Rev. Lett.* **88**, 190401 (2002).
- [126] J. Bjerlin, S. Reimann, and G. Bruun, “Few-Body Precursor of the Higgs Mode in a Fermi Gas”, *Phys. Rev. Lett.* **116**, 155302 (2016).
- [127] L. Bayha, M. Holten, R. Klemt, K. Subramanian, J. Bjerlin, S. M. Reimann, G. M. Bruun, P. M. Preiss, and S. Jochim, “Observing the emergence of a quantum phase transition shell by shell”, *Nature* **587**, 583 (2020).
- [128] M. Randeria, J.-M. Duan, and L.-Y. Shieh, “Superconductivity in a two-dimensional Fermi gas: evolution from Cooper pairing to Bose condensation”, *Phys. Rev. B* **41**, 327 (1990).
- [129] H. Heiselberg, “Fermi systems with long scattering lengths”, *Phys. Rev. A* **63**, 043606 (2001).
- [130] M. Randeria, J.-M. Duan, and L.-Y. Shieh, “Bound states, Cooper pairing, and Bose condensation in two dimensions”, *Phys. Rev. Lett.* **62**, 981 (1989).
- [131] B. Slavov and V. I. Dimitrov, “Influence of particle-number projection on potential energy surfaces of fissioning nuclei”, *Zeitschrift fuer Physik A Hadrons and Nuclei* **353**, 289 (1995).

- [132] N. Giovanardi, F. Barranco, R. A. Broglia, and E. Vigezzi, “Surface effects in nuclear Cooper pair formation”, *Phys. Rev. C* **65**, 041304 (2002).
- [133] N. Sandulescu, P. Schuck, and X. Viñas, “Nuclear pairing: surface or bulk?”, *Phys. Rev. C* **71**, 054303 (2005).
- [134] N. Pillet, N. Sandulescu, and P. Schuck, “Generic strong coupling behavior of Cooper pairs on the surface of superfluid nuclei”, *Physical Review C* **76**, 024310 (2007).
- [135] F. Werner and Y. Castin, “General relations for quantum gases in two and three dimensions: two-component fermions”, *Phys. Rev. A* **86**, 013626 (2012).
- [136] M. Rontani, J. R. Armstrong, Y. Yu, S. Åberg, and S. M. Reimann, “Cold Fermionic Atoms in Two-Dimensional Traps: Pairing versus Hund’s Rule”, *Phys. Rev. Lett.* **102**, 060401 (2009), ppublish.
- [137] M. Rontani, G. Eriksson, S. Åberg, and S. M. Reimann, “On the renormalization of contact interactions for the configuration-interaction method in two-dimensions”, *J. Phys. B: At. Mol. Opt. Phys.* **50**, 065301 (2017).
- [138] A. Speiser, L.-R. Mueller, P. Hoess, U. Matti, C. J. Obara, W. R. Legant, A. Kreshuk, J. H. Macke, J. Ries, and S. C. Turaga, “Deep learning enables fast and dense single-molecule localization with high accuracy”, *Nat. Methods* **18**, 1082 (2021).
- [139] W. Satuła and R. Wyss, “A number projected model with generalized pairing interaction”, *Nucl. Phys. A* **676**, 120 (2000).
- [140] M. Rigo, B. Hall, M. Hjorth-Jensen, A. Lovato, and F. Pederiva, “Solving the nuclear pairing model with neural network quantum states”, *Phys. Rev. E* **107**, 025310 (2023).
- [141] P. Lunt, P. Hill, J. Reiter, P. M. Preiss, M. Gałka, and S. Jochim, “Realization of a Laughlin State of Two Rapidly Rotating Fermions”, *Phys. Rev. Lett.* **133**, 253401 (2024).
- [142] P. Lunt, P. Hill, J. Reiter, P. M. Preiss, M. Gałka, and S. Jochim, “Engineering single-atom angular momentum eigenstates in an optical tweezer”, *Phys. Rev. A* **110**, 063315 (2024).
- [143] P. A. Murthy, M. Neidig, R. Klemt, L. Bayha, I. Boettcher, T. Enss, M. Holten, G. Zuern, P. M. Preiss, and S. Jochim, “High-temperature pairing in a strongly interacting two-dimensional Fermi gas”, *Science* **359**, 452 (2017).
- [144] X. Li et al., “Observation and quantification of the pseudogap in unitary fermi gases”, *Nature* **626**, 288 (2024).
- [145] P. A. Murthy, N. Defenu, L. Bayha, M. Holten, P. M. Preiss, T. Enss, and S. Jochim, “Quantum scale anomaly and spatial coherence in a 2D Fermi superfluid”, *Science* **365**, 268 (2019).
- [146] J. C. Brüggengjürgen, M. S. Fischer, and C. Weitenberg, “A phase microscope for quantum gases”, [10.48550/ARXIV.2410.10611](https://arxiv.org/abs/2410.10611) (2024), [arXiv:2410.10611 \[cond-mat.quant-gas\]](https://arxiv.org/abs/2410.10611).
- [147] T. Kitagawa, A. Aspect, M. Greiner, and E. Demler, “Phase-Sensitive Measurements of Order Parameters for Ultracold Atoms through Two-Particle Interferometry”, *Physical Review Letters* **106**, 115302 (2011).
- [148] W. Ketterle, D. S. Durfee, and D. M. Stamper-Kurn, “Making, probing and understanding Bose-Einstein condensates”, [10.48550/ARXIV.COND-MAT/9904034](https://arxiv.org/abs/cond-mat/9904034) (1999), [arXiv:cond-mat/9904034 \[cond-mat\]](https://arxiv.org/abs/cond-mat/9904034).

- [149] F. Zernike, “Phase contrast, a new method for the microscopic observation of transparent objects”, *Physica* **9**, 686 (1942).

## List of publications

- [SB1] M. Holten, L. Bayha, K. Subramanian, S. Brandstetter, C. Heintze, P. Lunt, P. M. Preiss, and S. Jochim, “Observation of Cooper pairs in a mesoscopic two-dimensional Fermi gas”, *Nature* **606**, 287 (2022).
- [SB2] S. Brandstetter, C. Heintze, K. Subramanian, P. Hill, P. M. Preiss, M. Gałka, and S. Jochim, “Magnifying the Wave Function of Interacting Fermionic Atoms”, [10.48550/ARXIV.2409.18954](https://arxiv.org/abs/2409.18954) (2024), [arXiv:2409.18954](https://arxiv.org/abs/2409.18954) [[cond-mat.quant-gas](https://arxiv.org/abs/2409.18954)].
- [SB3] S. Brandstetter et al., “Emergent interaction-driven elliptic flow of few fermionic atoms”, *Nat. Phys.*, [10.1038/s41567-024-02705-8](https://doi.org/10.1038/s41567-024-02705-8) (2025).



# List of Acronyms

<b>1D</b> one-dimensional	<b>MOT</b> magneto-optical trap
<b>2D</b> two-dimensional	<b>MT</b> magnifier trap
<b>2D-OT</b> 2D optical tweezer	<b>MW</b> microwave
<b>3D</b> three-dimensional	<b>NA</b> numerical aperture
<b>BEC</b> Bose-Einstein condensate	<b>OT</b> optical tweezer
<b>BCS</b> Bardeen, Cooper, and Schrieffer	<b>PSF</b> point spread function
<b>CICs</b> clock induced charges	<b>QGP</b> quark-gluon plasma
<b>CODT</b> crossed-beam optical dipole trap	<b>RF</b> radio frequency
<b>FOV</b> field-of-view	<b>RMS</b> root-mean-square
<b>EM-CCD</b> electron multiplying CCD camera	<b>SLM</b> spatial light modulator
<b>EOS</b> equation of state	<b>SWT</b> standing wave optical dipole trap
<b>HFB</b> Hartree-Fock-Bogoliubov	<b>TOF</b> time of flight
<b>LDA</b> local density approximation	<b>VdW</b> van der Waals
<b>MONIAC</b> Monetary National Income Analogue Computer	



# Acknowledgments

There are some things you can't share without ending up liking each other, and knocking out a twelve-foot mountain troll is one of them.

---

J.K. ROWLING

*Harry Potter and the Philosophers stone, 1997*

The last step in a PhD – writing this thesis – is undertaken alone. However, this last step is built on the contribution of many people, without whom none of this would have been possible. I would like to use this last (and probably most read) part of my thesis to thank all those who shaped my PhD journey. It has been a wonderful experience and five formative years that I would not want to miss.

First of all, I want to thank *Selim* for his support and mentorship during the last years. Your creativity and enthusiasm are extremely inspiring and have kept me going during this time. Working with you has shaped me, not only as a physicist, but as a person. In German, a PhD advisor is commonly referred to as a 'Doktorvater' and in my opinion, you really live up to this title. I am extremely happy that I decided to pursue a PhD in your group.

The working atmosphere in the Jochim group is amazing. A lot of great science has been made possible by the combination of creativity, enthusiasm and hard work, but also by a truly collaborative spirit (which includes, but is luckily not limited to, stealing equipment from each other). I never imagined that pulling fibers between labs could be so much fun. The hard times (that seem inevitable in the PhD journey) are always balanced by joint activities - ranging from spontaneous after work beers, random lunch break discussions (I still think that we should build a cold atom experiment in a submarine) and ice cream hauls to the Feuerzangenbowle or Cocktail evenings, bike trips to nearby lakes, Christmas cookie baking and of course the legendary Christmas video. Thanks to all the PhD students who have contributed to this wonderful atmosphere over the years:

*Luca*, one of the first experiences in my PhD was building your PhD hat. Luckily, you stayed for some more time as a Postdoc after that! Your intuitive pictures have really helped me to understand the physics background of our experiment. You have also introduced me to the playful taunting that is somewhat characteristic to the new experiment - I hope that this thesis fulfills your criteria for 'Jugend forscht'.

*Marvin*, thanks for sharing your vast knowledge about the experiment with me – even after you already left Heidelberg. Without your support in this time, none of this thesis would have been possible. You have also been the best road trip buddy - even though I am still convinced that meeting a black bear is preferable to meeting a rattle snake.

*Carl*, it is amazing how well our (somewhat) different temperaments balance each other out - I could not have wished for a better lab buddy. I am amazed that we (almost) never spiraled

at the same time and that we could thus always encourage each other when the experiment seemed to be an endless repair job. You are the only person with whom I ever want to realign the magnifier (not only because I don't ever want to do that again). Replacing you with a rubber duck while you were in Paris was never truly successful, and I was extremely happy when you rejoined the group. My weekend visit to Paris was an absolute blast – though it's a bit unfortunate that I didn't have the Garmin back then; it would have been thrilled with the tens of kilometers we walked through the city.

*Philipp*, for the elliptic flow project you became a temporary member of the new experiment, which I am extremely grateful for. It was invaluable to have you in the lab next door during the time that Carl was in Paris, and you always took time to help with things in the new experiment, even though you were also the sole PhD student in the old experiment at that time. Given the amount of physics we discussed during our bouldering sessions, we should have tried to get reimbursed for the ticket costs. I will also never forget the talk we gave in the university church and the night train adventure to Sweden (including the 3am wake-up call at the Danish border).

*Max*, my fellow Garmin victim – the steady stream of PhD memes has been a true source of joy over the past few months, much like the (sadly rare) swimming sessions. (Especially when they include jumping of the 5 m platform in Tiergartenbad.) I truly admire how sporty you are, while pursuing a PhD. Your attempts of talking me into doing a triathlon have so far been futile, but considering the landscape in Boston, I might finally get a road bike – and maybe we should both get friendlier fitness watches.

*Tobi*, somehow we abandoned our tradition of occasional after work burgers - we should really restart it, the discussions we had were always wonderful. I also had great fun Salsa dancing with you in that Cuban bar in Hannover - you must be a truly remarkable dancer to compensate for my total incompetence in that area.

*Paul*, if we ever come up with a groundbreaking idea, we should claim that it occurred to us while talking a walk on the beach in Sweden. It was great to have you as a conference buddy, both in Sweden and in Bingen - where we managed to reduce the average age in the café by at least 30 years.

*Johannes*, it was great to have another Austrian to rant with when our politics was (as it so often is) turbulent. I truly admire you for being organized enough to take a Bialetti to the DPG every single year. I think I would not have made it to a single morning session without your coffee supply.

*Daniel*, programming the Arduino code for Philipp's PhD hat with you was great fun – I hope you have as much fun programming the Arduino for my hat ;).

I also want to thank the two PostDocs that were part of the group during my time:

*Philipp*, our overlap was short, but luckily, you were still a part of both the magnifier and the elliptic flow project. Both projects benefited tremendously from your insights and I always gained new ideas from every single discussion with you!

*Maciek*, thank you for your invaluable constructive criticism and thoughtful insights. Your detailed feedback significantly improved the quality of our papers!. I greatly appreciate your

time, effort, and dedication in shaping this research into its final form.

The Jochim labs gang would of course not be complete without the master students that joined our group during the years: *Johanna, Diana, Jonas, Vivienne, Micha, Jonas, Ellen* and *Karen*.

We experimental physicists often poke at the universe like curious kids with a stick - just to see what happens. Many thanks to our theoretical collaborators for helping us justify our curiosity. I especially want to thank *Stephanie Reimann, Georg Bruun* and *Fabian Brauneis* - your ideas and feedback have challenged and refined my understanding of the physics underlying the pairing project. Special thanks go to Steffi for organizing the two great workshops at the Swedish coast - they were both truly inspiring! I also want to thank *Tilman Enss* for always having time to chat about new ideas or curiosities and providing us with helpful advice.

At my first conference, I was lucky to meet *Nick* and *Timo* - our love of lithium united us at the very first day, and I was extremely happy to meet both of you and also *Victor* at so many more conferences! From sledding and skiing in Obergurgl, swimming in Lake Ontario to drinking the occasional beer it was always great fun to spend time with you!

On the topic of conferences, I want to thank our administrative staff, *Ferman Alkasari, Alexandra Holten* and *Claudia Krämer*. Thank you for helping me figure out all the administrative forms!

I also want to thank the member's of my thesis committee: *Markus Oberthaler* for taking over the role of second referee and *Richard Schmidt* and *José R. Crespo López-Urrutia* for agreeing to be part of the committee - I look forward to discussing my work with you!

A big thank-you also goes to *Alice Ohlson* who recommended the high energy physics reviews on which Section 5.1 is based and *Markus Greiner*, who inspired me to write Section 4.1.1. Thank-you, *Fabian Finger* for sharing your L<sup>A</sup>T<sub>E</sub>X-template with me! I am also extremely grateful to everyone who agreed to proofread parts of this thesis: *Steffi, Max, Tobi, Carl, Maciek, Marvin* and *Philipp* - your feedback greatly improved this thesis!

A big shout out also goes to my friends back in Innsbruck: *Katha, Olli, Elli, Ingrid, Ralph, Marie, Tobi, Max, Claudia, Gabriele, Kathi, Flo* and (last but not least) *Sebi*. Thank you for providing me with excuses to come to Innsbruck and for always offering me places to sleep. Going hiking, biking or skiing with you has helped me keep my sanity during the last years. Its miraculous that you somehow always manage to make time when I randomly show up, even if it is only for a one-hour lay over between trains.

In diesem letzten (und wichtigsten) Teil dieser Arbeit möchte ich meiner Familie danken. Danke an meine Schwester *Susi* und ihren Mann *Stefan*, für eure Unterstützung und dafür, dass ihr es in euren Urlaubsplanungen so oft schafft einen Zwischenstopp in Heidelberg einzufügen. Danke an meine Patenkinder *Miriam* und *Martin*, für eure Neugier und Begeisterung. Entschuldige, dass ich am Wochenende nicht mehr oft nach Hause komme, ich freue mich immer Zeit mit euch zu verbringen und bin sehr stolz auf euch! Der größte Dank geht an meine Eltern - Danke *Mama* und *Papa* das ihr mich stets unterstützt, mich meinen eigenen Weg gehen lässt und mir aber gleichzeitig immer ein Auffangnetz bietet. Ich hab euch lieb!